The Astrophysical Journal, 687:1075–1106, 2008 November 10

ULTRAVIOLET SURVEY OF CO AND H_2 IN DIFFUSE MOLECULAR CLOUDS: THE REFLECTION OF TWO PHOTOCHEMISTRY REGIMES IN ABUNDANCE RELATIONSHIPS

Y. Sheffer,[1] M. Rogers,[1] S. R. Federman,[1,2] N. P. Abel,[3] R. Gredel,[4] D. L. Lambert,[5] and G. Shaw[6]

Received 2008 February 1; accepted 2008 June 28

ABSTRACT

We carried out a comprehensive far-UV survey of ^{12}CO and H_2 column densities along diffuse molecular Galactic sight lines. This sample includes new measurements of CO from *HST* spectra along 62 sight lines and new measurements of H_2 from *FUSE* data along 58 sight lines. In addition, high-resolution optical data were obtained at the McDonald and European Southern Observatories, yielding new abundances for CH, CH^+, and CN along 42 sight lines to aid in interpreting the CO results. These new sight lines were selected according to detectable amounts of CO in their spectra and provide information on both lower density ($\leq$100 cm^{-3}) and higher density diffuse clouds. A plot of log N(CO) versus log $N(H_2)$ shows that two power-law relationships are needed for a good fit of the entire sample, with a break located at log N(CO, cm^{-2}) = 14.1 and log $N(H_2)$ = 20.4, corresponding to a change in production route for CO in higher density gas. Similar logarithmic plots among all five diatomic molecules reveal additional examples of dual slopes in the cases of CO versus CH (break at log N = 14.1, 13.0), CH^+ versus H_2 (13.1, 20.3), and CH^+ versus CO (13.2, 14.1). We employ both analytical and numerical chemical schemes in order to derive details of the molecular environments. In the denser gas, where C_2 and CN molecules also reside, reactions involving C^+ and OH are the dominant factor leading to CO formation via equilibrium chemistry. In the low-density gas, where equilibrium chemistry studies have failed to reproduce the abundance of CH^+, our numerical analysis shows that nonequilibrium chemistry must be employed for correctly predicting the abundances of both CH^+ and CO.

Subject headings: astrochemistry — ISM: abundances — ISM: molecules — ultraviolet: ISM

1. INTRODUCTION

The most abundant molecule in the cosmos, H_2, has no permanent dipole moment and is thus lacking permitted pure rotation and vibration-rotation transitions. On the other hand, rotational transitions of CO, such as $J = 1–0$ at 115 GHz, have been routinely and extensively observed in molecular clouds, which are also too cold for detection of excited levels of H_2 (Papadopoulos et al. 2002 and references therein). Radio telescopes are thus used to map CO emission in the interstellar medium (ISM) in order to delineate global distributions of molecular clouds in our Galaxy and in other galaxies.

It is an empirical and theoretical foundation of radio mapping that the velocity-integrated emission intensity of CO (W_{CO}, in units of K km s^{-1}) from a molecular cloud is proportional to the total virialized mass of the cloud and hence to its hydrogen content (Larson 1981; Young & Scoville 1991). Radio astronomers thus utilize W_{CO} as a proxy for H_2, by employing the "X-factor" $X_{CO} = N(H_2)/W_{CO}(1–0)$, where N is the observed column density and X_{CO} is assumed hereafter to be in units of 10^{20} cm^{-2} (K km s^{-1})$^{-1}$.

An average value is ascribed to giant molecular clouds (GMCs) in the Milky Way, $X_{CO} \approx 4$ (Young & Scoville 1982; Dickman et al. 1986). Polk et al. (1988) found significant millimeter-wave emission from CO that was not associated with GMCs. This lowers the value of X_{CO}, having a mean value in the solar neighborhood of 1.8 ± 0.3 (Dame et al. 2001). A dependence of X_{CO} on the metallicity (primarily C/H) of the gas has been found in, e.g., studies of γ-ray emission across the Galaxy. This intensity is the product of interactions between cosmic rays and "stationary" gas; thus, the γ-ray intensity is proportional to the amount of gas along the line of sight. Strong et al. (2004) found that X_{CO} varies between 0.4 and 10.0 from the inner Galaxy to its outer regions, indicating lower gas metallicity in the outer Galaxy.

The GMCs, as well as the smaller dark clouds, are opaque enough that the CO in their cores is not dissociated by the interstellar far-UV radiation field. Consequently, CO is unobservable in the UV, necessitating its detection via millimeter-wave emission. On the other hand, diffuse molecular clouds (as well as envelopes of dark clouds) have visual extinctions lower than 5 mag, enabling a direct determination of column densities via line absorption in the UV. Both CO and H_2 are photodissociated by far-UV radiation, resulting in a variable X_{CO} that depends on the efficiency of self-shielding (as well as mutual shielding) of the two species (van Dishoeck & Black 1988) and thus on their column densities. One of our goals here is to study the behavior of X_{CO} under diffuse ISM conditions.

The Federman et al. (1980) study of diffuse interstellar clouds showed that there is an approximate quadratic relationship between CO and H_2, such that $N(CO) \propto [N(H_2)]^B$, with $B \approx 2$. Furthermore, Federman et al. (1980) remarked that for a group of lower N sight lines, a shallower slope with $B \approx 1.5$ was more appropriate, thus signaling the possibility of B varying with N. Indeed, for sight lines with log N(CO) $\leq$ 16, or values higher than those that were available to Federman et al. (1980), an even steeper relationship with $B \approx 3$ was found in the study of Pan et al. (2005). Both Burgh et al. (2007) and Sonnentrucker et al. (2007) confirmed the steepening of the slope near log N(CO) $\approx$ 15, attributing it to self-shielding of CO. Thus, a variable power law in CO versus

[1] Department of Physics and Astronomy, University of Toledo, Toledo, OH 43606; ysheffe@utnet.utoledo.edu, steven.federman@utoledo.edu.
[2] Guest Observer, McDonald Observatory, University of Texas, Austin, TX 78712.
[3] Department of Physics, University of Cincinnati, Cincinnati, OH 45221; npabel2@gmail.com.
[4] Max Planck Institute for Astronomy, Koenigstuhl 17, D69117 Heidelberg, Germany; gredel@mpia.de.
[5] W. J. McDonald Observatory, University of Texas, Austin, TX 78712; dll@astro.as.utexas.edu.
[6] Department of Astronomy and Astrophysics, Tata Institute of Fundamental Research, Mumbai 400005, India; gargishaw@gmail.com.

H_2 shows that the abundance of CO relative to H_2, and hence X_{CO}, is increasing with $N(H_2)$ along diffuse molecular sight lines. In this paper we explore the CO versus H_2 relationship in more detail, namely, the trend of CO (as well as of CH, CH^+, and CN) versus H_2 in diffuse molecular clouds and the dependence of these correlations on $N(H_2)$ and on physical parameters, such as the total gas (hydrogen) density, n_H.

Our study differs from the recent work of Burgh et al. (2007) and Sonnentrucker et al. (2007) in a number of ways. First, unlike Burgh et al. (2007) and like Sonnentrucker et al. (2007), our methodology is based on profile fitting of the data, with detailed decomposition into cloud component structures (Sheffer et al. 2007). We do not consider apparent optical depth or curve-of-growth treatments, which are always less preferred to spectrum synthesis by profile fitting (Sonnentrucker et al. 2007), nor do we build a grid of models to look for a solution with a single effective *b*-value (Burgh et al. 2007). Second, we follow up on these measurements of *N*-values with two methods of chemical analysis, analytical and numerical, in order to derive n_H at the sites where CO is detected. Third, we are able to discern two regimes of CO formation in terms of n_H. CO is associated with the similarly heavy diatomic molecules C_2 and CN inside denser and colder clumps of gas (Federman et al. 1994; Pan et al. 2005; Sonnentrucker et al. 2007), whereas in low-density clouds CO is related to the formation and chemistry of CH^+ (Zsargó & Federman 2003). Remarkably, this transition in the photochemistry of CO will be shown (§ 3) to affect also the trends of other correlations among the diatomic molecules analyzed here.

In § 2 we detail our sources for data and our methods of reduction and analysis. Next, in § 3 observational results are presented in terms of derived component structures and correlations between molecular column densities. In §§ 4, 5, and 6 we explore some of the physical conditions of the CO-harboring gas in terms of empirical relationships, analytical chemical analysis, and detailed numerical modeling with Cloudy, respectively. A discussion is given in § 7, followed by the conclusions in § 8.

2. DATA AND MODELING

Our primary effort was to detect and measure *N*(CO) for new sight lines from archival *Hubble Space Telescope* (*HST*) data. For most of these sight lines the value of $N(H_2)$ was already known from previous surveys with the *Copernicus* satellite (Savage et al. 1977) or *Far Ultraviolet Spectroscopic Explorer* (*FUSE*; Rachford et al. 2002; Andre et al. 2003; Cartledge et al. 2004; Pan et al. 2005). However, for consistency, we determined $N(H_2)$ also for sight lines with previously published results. Only two new sight lines (HD 36841 and HD 43818) lack any $N(H_2)$ data. For these, predicted values of $N(H_2)$ will be provided in § 4.4 after exploring the H_2 relationships with CO and CH. We obtained new high-resolution optical spectra of CH^+, CH, and CN by observing 42 sight lines at either McDonald Observatory or the European Southern Observatory (ESO). Results for ^{13}CO, which is also present in the *HST* spectra, were published in Sheffer et al. (2007).

Table 1 provides a list of all sight lines in terms of stars observed, their spectral types, visual magnitudes, Galactic coordinates, local standard of rest (LSR) corrections, $E(B-V)$ reddening values, and heliocentric distances. Table 2 lists the UV data sets from *HST* and *FUSE* for our stellar targets and Space Telescope Imaging Spectrograph (STIS) optical setups in terms of gratings and apertures.

2.1. *HST Data*

Initially, our sample included 66 sight lines without previous measurements of *N*(CO). The UV data for 63 of these consist of archival STIS observations, from which we extracted spectra of *A–X* bands of CO between 1229 and 1544 Å. The remaining three sight lines have archival GHRS data. Results on $N(^{12}CO)$ were subsequently published for 23 sight lines: 12 in Burgh et al. (2007), three in Sonnentrucker et al. (2007) (with one sight line in common with Burgh et al. 2007), and 12 in Sheffer et al. (2007) (with two in common with Burgh et al. [2007] and one in common with both Burgh et al. [2007] and Sonnentrucker et al. [2007]). Thus, this paper presents new $N(^{12}CO)$ results for 43 sight lines. To the entire CO sample of 66 sight lines we added previously published *N*(CO) values for 48 directions, yielding a sample of 114 sight lines with UV data. Figure 1 presents the view of CO absorption along two *HST* STIS sight lines that differ by a factor of 700 in *N*(CO).

2.2. *FUSE Data*

Our initial sample of 58 sight lines was obtained from archival *FUSE* observations of H_2 absorption at $\lambda < 1100$ Å. Of these, 33 sight lines did not have published $N(H_2)$ results. In the meantime, $N(H_2)$ results were published for five sight lines in Burgh et al. (2007) and five more in Sheffer et al. (2007) (with a single sight line in common with Burgh et al. 2007). This paper, therefore, presents first $N(H_2)$ results for 24 sight lines. As described in Federman et al. (2005), our $N(H_2)$ values are obtained from spectrum synthesis of the (2–0), (3–0), and (4–0) bands of the Lyman *B–X* transitions of H_2. The total column density $N(H_2)$ listed is based on the absorption from all rotational levels with $J'' = 0$–5. Roughly 95% of the total is found in the two $J'' = 0$ and 1 ground states of para- and ortho-H_2, respectively. Figure 2 presents a sample of two *FUSE* sight lines with H_2 absorption profiles that differ by a factor of 13 in $N(H_2)$.

The spectral coverage of *FUSE* also contains absorption features from CO (Sheffer et al. 2003; Crenny & Federman 2004). Thus, for three sight lines (HD 208905, HD 209481, and HD 209975) with no *HST* spectroscopy we determined *N*(CO) from the *B–X* (0–0), *C–X* (0–0), and *E–X* (0–0) bands of CO, as well as confirmed the CO content along the line of sight toward HD 200775 that was previously based on *IUE* data (Knauth et al. 2001). The former three stars were included in the high-resolution optical study of CH, CH^+, and CN by Pan et al. (2004, 2005).

2.3. *McDonald Data*

High-resolution optical observations of CH^+ and CH were obtained with the 2dcoude cross-dispersed echelle spectrometer (Tull et al. 1995) for the purpose of deriving cloud structure templates for CO and H_2, without which one cannot reliably derive the line optical depth for sight lines with very high column densities. In addition, the echelle spectra included absorption from Ca II and CN; the first provides a high signal-to-noise ratio (S/N) confirmation of the cloud structure, while *N*(CN) is used to model the total gas density in the absorbing cloud, based on the CH and C_2 chemical reaction network described in § 5.1. Additional absorption from CH^+ provides a check on the component structure for directions with low molecular concentrations.

Sight lines toward 20 stars were observed at $R \sim 170{,}000$ with the 2.7 m Harlan J. Smith Telescope at McDonald Observatory, Texas, during observing runs in 2004 January, October, and December and 2005 May and October. Each echelle exposure included nine orders, which simultaneously recorded two atomic transitions, Ca I at 4226 Å and the K line of Ca II at 3933 Å, as well as absorption lines from three molecules, CH at 4300 Å, CH^+ at 4232 Å, and CN at 3784 Å. Two-dimensional reduction tasks in IRAF were used to correct these for bias, scattered light, pixel-to-pixel variations, and finally to calibrate the wavelength

TABLE 1

STELLAR DATA FOR SIGHT LINES WITH NEW DETECTIONS OF CO

Star	Name	Spectral Type	V (mag)	l (deg)	b (deg)	v_{LSR}[a] (km s^{-1})	$E(B-V)$ (mag)	D_{helio}[b] (pc)	References[c]
BD +48 3437	...	B1 Iab	8.73	93.56	−2.06	14.4	0.35	6500	1, 2
BD +53 2820	...	B0 IV:n	9.96	101.24	−1.69	12.8	0.29	4100	3, 3
CPD −69 1743	...	B2 Vn	9.46	303.71	−7.35	−8.0	0.30	4700	4, 4
CPD −59 2603	V572 Car	O7 V	8.75	287.59	−0.69	−11.6	0.46	2600	4, 4
HD 12323	...	O9	8.92	132.91	−5.87	3.5	0.23	3600	3, 3
HD 13268	...	O8 Vnn	8.18	133.96	−4.99	3.3	0.36	2400	3, 3
HD 13745	V354 Per	O9.7 II	7.90	134.58	−4.96	3.1	0.46	1600	1, 2
HD 14434	...	O6.5	8.59	135.08	−3.82	3.1	0.48	4100	3, 3
HD 15137	...	O9.5 V	7.86	137.46	−7.58	1.8	0.35	2700	1, 2
HD 23180	o Per	B1 III	3.86	160.36	−17.74	−6.7	0.30	430	3, 3
HD 23478	...	B3 IV	6.69	160.76	−17.42	−6.7	0.28	240	1, 5
HD 24190	...	B2 V	7.45	160.39	−15.18	−6.4	0.30	550	1, 2
HD 24398	ζ Per	B1 Iab	2.88	162.29	−16.69	−7.1	0.34	300	6, 5
HD 30122	HR 1512	B5 III	6.34	176.62	−14.03	−10.9	0.40	220	7, 2
HD 34078	AE Aur	O9.5 Ve	6.00	172.08	−2.26	−8.4	0.53	450:	1, 5
HD 36841	...	O8	8.58	204.26	−17.22	−17.1	0.35	1200	1, 2
HD 37367	HR 1924	B2 IV–V	5.99	179.04	−1.03	−10.1	0.42	240	3, 3
HD 37903	...	B1.5 V	7.84	206.85	−16.54	−17.6	0.32	790	6, 2
HD 43818	11/LU Gem	B0 II	6.92	188.49	+3.87	−11.9	0.52	1600	3, 3
HD 58510	...	B1 Iab	6.80	235.52	−2.47	−18.8	0.32	4500	1, 2
HD 63005	...	O7	9.13	242.47	−0.93	−18.5	0.32	5200	1, 2
HD 91983	...	O9.5/B0 Ib:	8.58	285.88	+0.05	−11.9	0.29	7000	3, 3
HD 93205	V560 Car	O3 V	7.76	287.57	−0.71	−11.6	0.38	3200	3, 3
HD 93222	...	O8	8.11	287.74	−1.02	−11.6	0.36	1700	3, 3
HD 93237	DR Cha	B4 IVe	5.97	297.18	−18.39	−10.9	0.09	310	8, 5
HD 93840	...	B1.5 Iab	7.79	282.14	+11.10	−11.1	0.16	5700	1, 2
HD 94454	...	B8 III	6.70	295.69	−14.73	−11.0	0.18	330	8, 5
HD 96675	...	B6 IV/V	7.6	296.62	−14.57	−10.7	0.30	160	3, 5
HD 99872	HR 4425	B3 V	6.11	296.69	−10.62	−10.4	0.36	230	3, 5
HD 102065	...	B2 V	6.61	300.03	−18.00	−10.1	0.17	170	9, 2
HD 106943	...	B7 IV	7.51	298.96	+1.14	−8.3	0.15	500	1, 2
HD 108002	...	B2 Ia/ab	6.95	300.16	−2.48	−8.4	0.32	3400	1, 2
HD 108610	...	B3 IV/V	6.92	300.28	+0.88	−7.9	0.15	380	1, 5
HD 108639	...	B1 III	7.81	300.22	+1.95	−7.8	0.37	110	1, 2
HD 110434	...	B8/9 III	7.55	302.07	−3.60	−8.0	0.05	370:	8, 5
HD 112999	V946 Cen	B6 IIIn	7.38	304.17	+2.18	−6.6	0.23	340	1, 5
HD 114886	...	O9 V	6.89	305.52	−0.83	−6.6	0.40	1000	10, 2
HD 115071	V961 Cen	O9.5 V	7.97	305.76	+0.15	−6.4	0.53	1200	1, 2
HD 115455	...	O7.5 III	7.97	306.06	+0.22	−6.3	0.49	2000	8, 2
HD 116852	...	O9 III	8.49	304.88	−16.13	−8.6	0.21	4800	3, 3
HD 122879	HR 5281	B0 Ia	6.43	312.26	+1.79	−4.2	0.36	2300	3, 3
HD 124314	...	O7	6.64	312.67	−0.42	−4.4	0.53	1100	4, 4
HD 137595	...	B3 Vn	7.50	336.72	+18.86	5.7	0.25	400	1, 2
HD 140037	...	B5 III	7.48	340.15	+18.04	6.6	0.09	270:	8, 5
HD 144965	...	B3 Vne	7.12	339.04	+08.42	5.2	0.35	290	8, 2
HD 147683	V760 Sco	B4 V	7.05	344.86	+10.09	7.2	0.39	280	1, 2
HD 147888	ρ Oph D	B3/B 4V	6.78	353.65	+17.71	10.5	0.51	140	3, 5
HD 152590	...	O7.5 V	8.48	344.84	+1.83	6.2	0.48	1800	1, 2
HD 152723	...	O7/O8	7.31	344.81	+1.61	6.1	0.42	1600	3, 3
HD 157857	...	O7e	7.81	12.97	+13.31	14.9	0.43	1900	3, 3
HD 163758	...	O6.5	7.32	355.36	−6.10	8.1	0.33	2600	6, 2
HD 185418	...	B0.5 V	7.52	53.60	−2.17	18.1	0.50	910	3, 3
HD 190918	V1676 Cyg	WN	6.81	72.65	+2.07	18.0	0.45	2300	1, 2
HD 192035	RX Cyg	B0 IIIn	8.22	83.33	+7.76	17.3	0.37	2800	1, 2
HD 192639	...	O8 e	7.11	74.90	+1.48	17.7	0.62	1600	6, 2
HD 195965	...	B0 V	6.98	85.71	+5.00	16.7	0.25	790	1, 2
HD 198781	HR 7993	B0.5 V	6.46	99.94	+12.61	14.7	0.35	730	3, 3
HD 200775	V380 Cep	B2 Ve	7.42	104.06	+14.19	13.9	0.57	430:	11, 5
HD 203532	HR 8176	B3 IV	6.36	309.46	−31.74	−8.6	0.28	250	3, 5
HD 208905	...	B1 Vp	7.01	103.53	+5.17	13.1	0.37	790	1, 2
HD 209481	14/LZ Cep	O9 V	5.55	102.01	+2.18	13.1	0.37	690	1, 2

TABLE 1—*Continued*

Star	Name	Spectral Type	V (mag)	l (deg)	b (deg)	v_{LSR}[a] (km s^{-1})	$E(B-V)$ (mag)	D_{helio}[b] (pc)	References[c]
HD 209975	19 Cep	O9 Ib	5.11	104.87	+5.39	12.8	0.34	1300	3, 3
HD 210121	...	B9	7.69	56.88	−44.46	7.9	0.31	210	3, 5
HD 210809	...	O9 Ib	7.56	99.85	−3.13	13.0	0.31	4000	3, 3
HD 220057	NSV 14513	B2 IV	6.95	112.13	+0.21	10.4	0.23	560	3, 3
HD 303308	...	O3 V	8.21	287.59	−0.61	−11.6	0.45	3600	3, 3
HD 308813	...	O9.5 V	9.32	294.79	−1.61	−10.0	0.31	2400	1, 2

NOTE.—Information from the SIMBAD database is included.

[a] Correction from heliocentric velocity to the LSR frame.

[b] Distance derived from either a spectroscopic parallax using M_V from Table 3 of Shull & Van Steenberg (1985), unless taken from the $E(B-V)$ reference, or from a $\geq 4\ \sigma$ *Hipparcos* parallax from Perryman et al. (1997) as listed by SIMBAD, unless a $\geq 3\ \sigma$ parallax was used and flagged with a colon.

[c] First reference is for $E(B-V)$, the second is for D_{helio}.

REFERENCES.—(1) Neckel & Klare 1980; (2) Shull & Van Steenberg 1985; (3) Valencic et al. 2004; (4) Diplas & Savage 1994; (5) Perryman et al. 1997; (6) Wegner 2003; (7) Carnochan 1986; (8) Andersson et al. 2002; (9) Rachford et al. 2002; (10) Savage et al. 1985; (11) Le Coupanec et al. 1999.

TABLE 2
UV DATA SETS FOR NEW CO SIGHT LINES

	HST STIS			*FUSE*		*HST* STIS			*FUSE*
STAR	Data Set	Grating	Slit	DATA SET	STAR	Data Set	Grating	Slit	DATA SET
BD +48 3437	o6359s	E140M	0.2X0.2	P10184	HD 110434	o6lj0b	E140H	0.1X0.03	A12019
BD +53 2820	o6359q	E140M	0.2X0.2	P12232	HD 112999	o6lj0c	E140H	0.1X0.03	A12020
CPD −69 1743	o63566	E140M	0.2X0.2	P10137	HD 114886	o6lj0d	E140H	0.1X0.03	A12018
CPD −59 2603	o40p01	E140H	0.2X0.09	P12215	HD 115071	o6lj0e	E140H	0.2X0.09	G93215
	o4qx03	E140H	0.2X0.09	...	HD 115455	o6lj0f	E140H	0.1X0.03	A12007
HD 12323	o63505	E140M	0.2X0.2	P10202	HD 116852	o63571	E140H	0.2X0.2	P10138
HD 13268	o63506	E140M	0.2X0.2	P10203	HD 122879	o6lz57	E140H	0.2X0.2	B07105
HD 13745	o6lz05	E140M	0.2X0.2	P10204	HD 124314	o54307	E140H	0.1X0.03	P10262
HD 14434	o63508	E140M	0.2X0.2	P10205		o6lz58	E140H	0.2X0.2	...
HD 15137	o6lz06	E140H	0.2X0.2	P10206	HD 137595	o6lj03	E140H	0.2X0.09	A12012
HD 23180	o64801–4	E140H	0.2X0.05	...	HD 140037	o6lj04	E140H	0.1X0.03	A12015
HD 23478	o6lj01	E140H	0.1X0.03	A12002	HD 144965	o6lj05	E140H	0.1X0.03	A12016
HD 24190	o6lj02	E140H	0.1X0.03	A12001	HD 147683	o6lj06	E140H	0.2X0.09	A12009
HD 24398	o64810–11	E140H	0.2X0.05	...	HD 147888	o59s05	E140H	0.2X0.09	P11615
HD 30122	o5c065	E140H	0.2X0.2	Q20103	HD 152590	o6lz67	E140M	0.2X0.2	B07106
HD 36841	o63516	E140M	0.2X0.2	...	HD 152723	o63586	E140H	0.2X0.2	P10271
HD 37367	o5c013	E140H	0.2X0.2	B07102	HD 157857	o5c04d	E140H	0.2X0.2	P10275
HD 37903	o59s04	E140H	0.2X0.09	P11606	HD 163758	o63595	E140H	0.2X0.2	P10159
HD 43818	o5c07i	E140H	0.2X0.2	...	HD 185418	o5c01q	E140H	0.2X0.2	...
HD 58510	o63530	E140H	0.2X0.2	P10219	HD 190918	o6359j	E140M	0.2X0.2	P10285
HD 63005	o63531	E140M	0.2X0.2	P10221	HD 192035	o6359k	E140M	0.2X0.2	P10286
HD 91983	o5c08n	E140H	0.2X0.2	B07104	HD 192639	o5c08t	H140H	0.2X0.2	...
HD 93205	o4qx01	E140H	0.2X0.09	P10236	HD 195965	o6bg01	E140H	0.1X0.03	P10288
HD 93222	o4qx02	E140H	0.2X0.09	P10237	HD 198781	o5c049	E140H	0.2X0.2	P23102
HD 93237	o6lj0g	E140H	0.1X0.03	A12010	HD 200775	...	...	...	A05101
HD 93840	o63549	E140H	0.2X0.2	P10127	HD 203532	o5co1s	E140H	0.2X0.2	B07108
HD 94454	o6lj0h	E140H	0.1X0.03	A12005	HD 208905	...	...	...	D01401
HD 96675[a]	z19w01[a]	G160M[a]	0.25[a]	Q10102	HD 209481	...	...	...	D01402
HD 99872	o6lj0i	E140H	0.1X0.03	A12006	HD 209975	...	...	...	D01403
HD 102065	o4o001	E140H	0.2X0.09	Q10101	HD 210121	...	...	...	P24901
HD 106943	o6lj07	E140H	0.1X0.03	A12011	HD 210809	o6359t	E140M	0.2X0.2	P12231
HD 108002	o6lj08	E140H	0.1X0.03	A12017	HD 220057	o5c01x	E140H	0.2X0.2	Z90178
HD 108610	o6lj09	E140H	0.1X0.03	A12014	HD 303308	o4qx04	E140H	0.2X0.09	P12216
HD 108639	o6lj0a	E140H	0.2X0.09	A12013	HD 308813	o63559	E140M	0.2X0.2	P12219

[a] The *HST* data set for HD 96675 is from the GHRS, not the STIS.

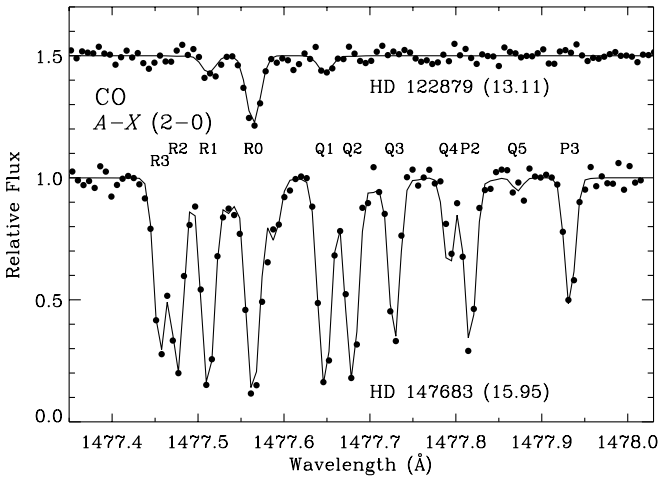

FIG. 1.—Sample CO spectra (*filled circles*) from *HST* STIS and Ismod.f fits (*solid lines*) for HD 147683 ($\log N = 15.95$) and HD 122879 (13.11). The second spectrum has been shifted upward by 0.5 continuum units.

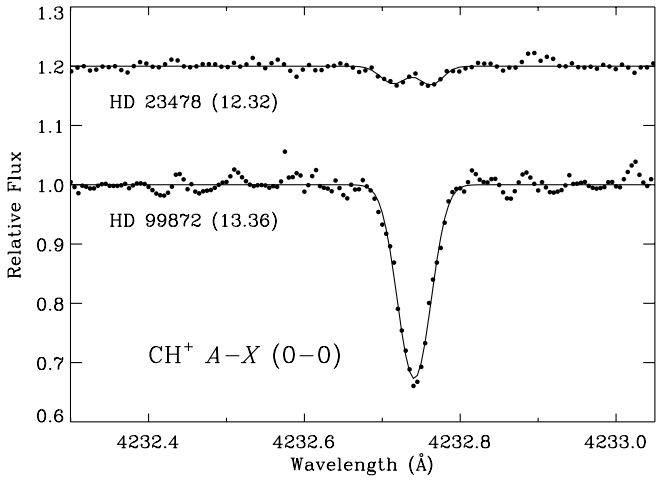

FIG. 3.—Sample optical CH^+ spectra (*filled circles*) and Ismod.f fits (*solid lines*) for HD 99872 (from ESO, $\log N = 13.36$) and HD 23478 (McDonald, 12.32). The second spectrum has been shifted upward by 0.2 continuum units. Note the presence of two cloud components along the sight line toward HD 23478 (also seen in CN in Fig. 5).

scale based on accompanying exposures of a Th-Ar lamp. The latter step yielded residuals smaller than 0.001 Å, or <0.07 km s^{-1}.

2.4. *ESO Data*

For the 17 stars in our sample that are located too far south to be observable from McDonald, data were obtained at ESO[7] in Chile. Five more sight lines were added to the ESO observing program to complement CH results given in Andersson et al. (2002) with new CH^+ and CN acquisitions. For the 22 sight lines we obtained exposures on CH for 16 sight lines, on CH^+ for 19 sight lines, and on CN for five sight lines. The observations were carried out at the 3.6 m telescope at La Silla in 2005 June and 2006 June using the Coudé Echelle Spectrograph (CES; Enard 1982). The CES is fed with an optical fiber with an aperture of 2″ on the sky and provides R of 220,000. The data were bias subtracted, flat-fielded, and rebinned to a linear wavelength scale using the MIDAS long package. Figures 3, 4, and 5 provide comparisons of sight lines with weak and strong absorption from CH^+, CH, and CN, respectively. HD 23478 and HD 210121 were observed at McDonald, whereas the acquisition of data for HD 99872 and HD 116852 occurred at ESO.

[7] Based on observations collected at the European Southern Observatory, La Silla, Chile, programs 075.C-0025(A) and 077.C-0116(A).

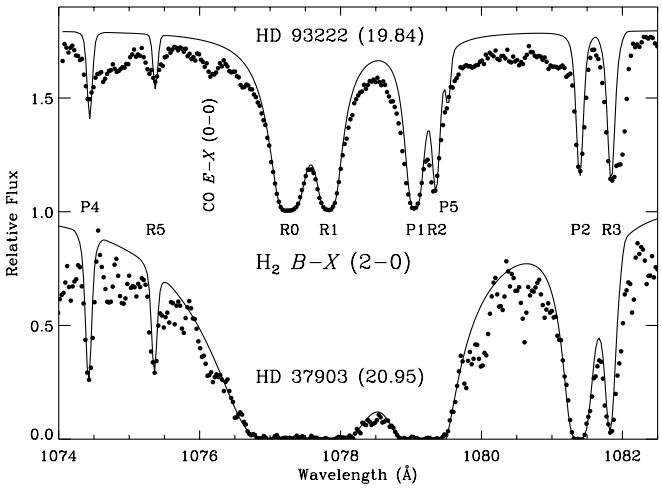

FIG. 2.—Sample H_2 spectra (*filled circles*) from *FUSE* and Ismod.f fits (*solid lines*) for HD 37903 ($\log N = 20.95$) and HD 93222 (19.84). The second spectrum has been shifted upward by 0.8 continuum units. Each spectrum synthesis with Ismod.f includes also the (3–0) and the (4–0) bands. Also seen is one of the CO Rydberg bands at 1076 Å.

2.5. *Ismod.f Spectrum Synthesis*

We used the Y. S. code, Ismod.f, to model Voigt absorption profiles via spectrum synthesis and automatic rms minimizations of (data minus fit) residuals. Besides presenting the data, Figures 1–5 all include spectrum synthesis fits that were performed with Ismod.f. The basic absorption equations were adapted in 1990 from Black & van Dishoeck (1988). Besides fitting radial velocity, excitation temperature (T_{ex}), and total N for any absorption feature, Ismod.f provided solutions for cloud structures along each sight line, i.e., the number of cloud components, their relative shifts and fractions, and their Doppler widths (b-values). This information is critical for proper evaluation of large optical depth effects and has to be derived ab initio whenever not known from previous investigations. Table 3 presents all cloud components that we were able to identify via molecular absorption,

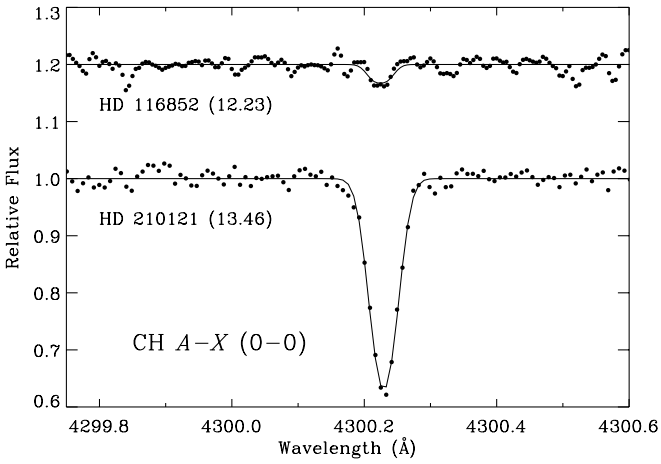

FIG. 4.—Sample optical CH spectra (*filled circles*) and Ismod.f fits (*solid lines*) for HD 210121 (from McDonald, $\log N = 13.46$) and HD 116852 (ESO, 12.23). The second spectrum has been shifted upward by 0.2 continuum units.

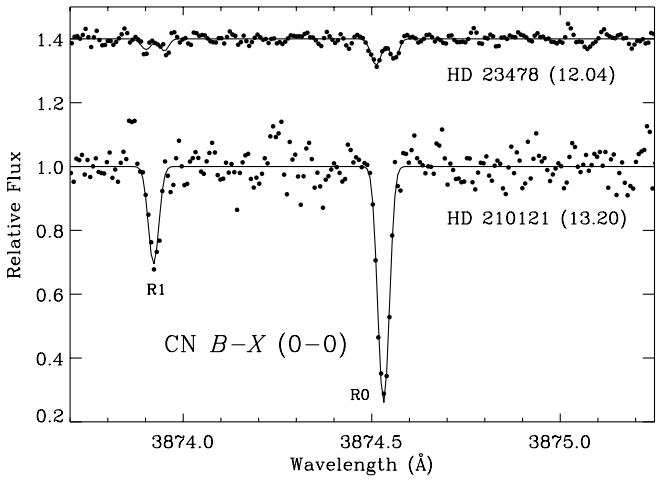

FIG. 5.—Sample optical CN spectra (*filled circles*) from McDonald and Ismod.f fits (*solid lines*) for HD 210121 ($\log N = 13.20$) and HD 23478 (12.04). The second spectrum has been shifted upward by 0.4 continuum units. Both the R0 and R1 transitions of CN are shown, and both absorption lines have two cloud components toward HD 23478, as is the case with CH^+ in Fig. 3.

while Figures 3 and 5 present spectra of CH^+ and CN toward HD 23478, with each species clearly showing two cloud components. Our criteria for detection were a 2 σ limit for molecular column density, as well as simultaneous detection in Ca II (Pan et al. 2005). All radial velocities have been transformed from the heliocentric scale to the LSR reference frame. For CO transition strengths we used the *f*-values of Chan et al. (1993), which in a global sense have been verified to a level of a few percent by Eidelsberg et al. (1999), while wavelengths were obtained from Morton & Noreau (1994). Both *f*-values and wavelengths for H_2 were obtained from Abgrall et al. (1993a, 1993b) via files available on the Dr. McCandliss Web site.[8] As for the species with optical transitions, the corresponding input values for Ca I, Ca II, CH, CH^+, and CN were taken from Table 3.4 in Pan (2002).

A subset sample of $N(^{12}CO)$ and $N(^{13}CO)$ for 25 sight lines was published by Sheffer et al. (2007), who showed that a minimal number of absorption bands are needed for a robust modeling of N(CO). Specifically, a few bands that are optically thin and a few that are optically thick should be simultaneously synthesized to yield a good measure of N and of those parameters that affect line saturation in the bands, such as b and T_{ex}. Based on that sample of CO results, we find that our uncertainties in N range from a few to ~20%. Thus, to be on the conservative side, we assume that the 1 σ errors are ±20%, plotting this value in all of our relevant figures.

All H_2 lines from the $J'' \leq 5$ levels were modeled simultaneously with Ismod.f. The major difference in modeling methodology between CO and H_2 is that for the latter we do not attempt to fit any parameters that are associated with the cloud component structure along the line of sight. This is a direct result of the relatively low spectral resolution of *FUSE* ($R \sim 20{,}000$), as well as the restricted available range (compared to CO) in *f*-values for the Lyman and Werner bands of H_2. Since it had been discovered (Federman 1982) and is verified in § 3.3 that N(CH) and $N(H_2)$ have a linear relationship, our method is to apply any cloud structure already known from high-resolution CH data to the modeling of H_2, while keeping such structure parameters fixed during the fit. As in our previous work (Pan et al. 2005; Federman et al. 2005), we prefer known cloud structures to effective *b*-values as the proper solution to H_2 line saturation. This is in contrast to CO, where parameters such as relative strength and width of components are allowed to vary during the fit. Further details can be found in our earlier paper (Sheffer et al. 2007). In a similar fashion to CO, we show global ±20% 1 σ error bars in all our figures that present values for $N(H_2)$. This uncertainty is consistent with published results.

Whenever repeated multiple exposures are available, we combined them in wavelength space for an improved S/N. In addition, when a feature (band) appears in two adjacent orders, we combined them after correcting for any small wavelength inconsistencies by subtracting the wavelength shifts as measured from the absorption-line positions. All our reductions were in IRAF and STSDAS. A single Gaussian was used to describe the instrumental profile of STIS, but R was allowed to be a free parameter in the CO fits. This revealed that R is a decreasing function of slit size for both the E140H and the E140M gratings of STIS (see Fig. 4 of Sheffer et al. 2007). The range of fitted resolving powers per aperture agrees well with the range of values given by Bowers (1997), showing that Ismod.f has a good handle on R. Table 4 provides logarithmic values for total line of sight N of all five diatomic molecules that were modeled with Ismod.f spectrum synthesis in this study, as well as supplementary N-values from the literature. Throughout the paper, all $\log N$ values are expressed in units of cm^{-2}.

3. OBSERVED RELATIONSHIPS

3.1. *Component Structures*

Our aim of deriving accurate column densities was the main reason for obtaining high-resolution spectra, both for CO from *HST* UV exposures and for CH, CH^+, and CN from new optical data. These spectra reach velocity resolutions between 1.5 and 2.0 km s^{-1}, enough to resolve many sight lines into multiple cloud components. The unveiling of such structures is important both for correctly treating the optical depth along the sight lines (by deriving *b*-values for the line widths) and for distinguishing characteristics of individual parcels of gas that would otherwise be lost in integrated line-of-sight values (Pan et al. 2005).

Our earlier analysis of individual cloud components toward Cep OB2 in Pan et al. (2005) showed that fits of CO cloud structures consistently resulted in structures that were similar to CN structures, even though the input for the synthesis of CO was based on CH cloud structures that have more components than those found for CN. However, the sight lines sampled toward Cep OB2 were molecule-rich, with a median value of $N(CO) = 2.5 \times 10^{15}$ cm^{-2}, and with CN detections along 73% of the sight lines. The new CO sample presented here is molecule-poor, with a median value of $N(CO) = 1.0 \times 10^{14}$ cm^{-2}, i.e., a factor of 25 lower in CO abundance relative to the Cep OB2 sample. Most of the poorest sight lines here [$\log N(CO) \lesssim 14$] are without detected N(CN) but with CO cloud structures that are very similar to those of both CH and CH^+, whereas for sight lines with CN detections, CN is found in only about half of the components detected in CO.

The lower molecular abundance along the new sight lines is also reflected in the generally low number of cloud components for all observed molecular species, even though these are mostly sight lines with large path lengths that have a higher chance of intersecting molecular clouds. Whereas 53% of the sample stars are farther than 1 kpc, and 23% are farther than 3 kpc, the derived cloud structures have low means of components per sight line: 1.9 ± 1.0, 1.8 ± 0.9, and 1.7 ± 0.8 for CH^+, CH, and CO, respectively. This shows that CO is in excellent agreement with

[8] See http://www.pha.jhu.edu/~stephan/h2ools2.html.

TABLE 3

NEWLY DETECTED CLOUD COMPONENTS OF MOLECULAR SPECIES

		CO		CN		CH		CH^+	
STAR	v_{LSR} (km s^{-1})	N (10^{14} cm^{-2})	b (km s^{-1})	N (10^{12} cm^{-2})	b (km s^{-1})	N (10^{12} cm^{-2})	b (km s^{-1})	N (10^{12} cm^{-2})	b (km s^{-1})
BD +48 3437	−16.4	...	...	...	...	...	...	4.35	1.8
	−11.4	...	...	...	...	...	...	0.98	1.0
	−1.0	0.23	1.5	...	...	...	...	2.15	1.7
	5.2	...	...	0.41	0.5	6.86	3.2	7.25	1.6
BD +53 2820	−5.4	...	...	...	...	...	...	2.15	1.0
	0.9	0.50	0.5	...	...	1.59	0.5	...	...
	6.9	0.27	0.4	...	...	2.49	1.1	4.26	2.2
CPD −69 1743	0.8	0.11	1.4	...	...	...	...	15.42	1.4
CPD −59 2603	−5.7	0.08	1.5	...	...	3.80	1.3	...	...
	−2.8	1.13	0.7	...	...	7.91	0.5	16.36	2.9
HD 12323	−13.5	2.53	0.7	0.63	0.5	1.97	1.0	...	...
	−9.7	...	...	0.73	0.5	2.37	1.0	...	...
	−5.9	0.89	0.8	...	...	1.98	2.3	5.52	2.5
	0.3	...	...	...	...	...	...	2.42	1.5
HD 13268	−36.2	...	...	...	...	0.94	1.0	...	...
	−19.5	...	...	...	...	...	...	3.1	3.0
	−16.4	0.16	1.3	...	...	1.13	1.0	...	...
	−10.4	...	...	0.43	0.5	2.06	1.9	3.5	2.3
	−7.4	1.26	1.0	0.94	1.3	5.29	2.3	...	...
	−5.1	...	...	...	...	...	...	4.8	1.6
	−1.0	0.14	1.0	...	...	2.15	2.5	3.5	1.5
HD 13745	−43.9	0.33	0.7	0.52	1.1	5.85	2.3	8.59	2.0
	−18.1	0.36	0.5	...	...	3.97	1.9	10.98	2.8
	−10.3	0.11	1.3	...	...	...	...	7.22	3.0
	−4.3	0.07	0.3	...	...	...	...	...	...
	0.0	...	...	...	...	...	...	5.89	3.0
HD 14434	−6.1	0.43	0.6	...	...	...	...	8.52	3.0
	−1.0	1.83	0.7	0.39	0.8	9.24	2.3	14.94	2.5
HD 15137	−13.4	0.11	0.7	...	...	2.17	2.5	4.13	2.9
	−7.4	...	...	...	...	1.49	1.0	7.70	3.0
	−4.0	0.03	0.6	...	...	...	...	...	...
	−0.2	0.19	1.3	...	...	2.50	2.1	2.26	1.7
HD 23180	4.6	0.81	0.8	...	...	7.01	2.1	1.58	2.0
	7.3	5.97	1.0	1.33	1.7	11.96	1.5	5.72	2.0
HD 23478	4.1	6.28	1.0	0.67	1.1	13.53	1.8	1.42	1.2
	7.7	1.77	0.9	0.43	0.5	4.72	0.9	1.40	1.0
HD 24190	6.5	0.84	0.5	0.50	1.8	...	...	...	...
	9.7	0.06	1.0	...	...	...	...	...	...
HD 24398	6.8	17.95	0.8	3.20	1.0	21.41	1.6	3.13	2.3
HD 30122	4.2	...	...	...	...	...	...	2.98	2.9
	6.9	7.04	0.8	0.87	1.3	15.66	2.0	...	...
HD 36841	−4.6	0.46	0.5	...	...	...	...	...	...
	5.7	0.35	0.4	...	...	...	...	...	...
	10.6	...	...	0.78	0.5	9.98	1.5	5.74	2.2
HD 37367	3.8	...	...	...	...	2.21	2.0	...	...
	6.2	0.70	1.5	...	...	9.80	2.0	32.41	2.2
HD 43818	−7.0	...	...	...	...	3.22	2.5	...	...
	−3.9	0.74	1.5	...	...	3.23	1.6	3.61	1.8
	1.2	...	...	...	...	2.77	1.6	7.36	3.0
	5.2	...	...	...	...	2.03	1.9	4.14	3.0
HD 58510	23.6	...	...	...	...	...	...	1.77	1.5
	26.7	...	...	...	...	2.52	2.0	10.74	2.1
	29.6	0.18	1.5	...	...	2.53	1.6	...	...
HD 63005	9.9	...	...	...	...	...	...	2.67	1.8
	14.3	0.63	0.9	0.99	1.1	4.51	2.2	5.67	2.5
	21.0	0.39	1.5	...	...	4.46	2.0	5.69	1.7
HD 91983	−14.0	0.62	0.5	...	...	...	...	3.27	1.2
HD 93205	−6.5	0.06	1.0	...	...	1.33	1.0	...	...
	−2.8	0.08	0.3	...	...	1.31	0.5	...	...
HD 93222	−6.3	0.18	1.5	...	...	2.28	2.1	...	...
HD 93237[a]	3.5	0.25	0.7	...	...	1.2	0.7	...	...
HD 93840	−7.0	0.18	0.8	...	...	1.79	0.5	3.28	2.7

TABLE 3—*Continued*

Star	v_{LSR} (km s^{-1})	CO N (10^{14} cm^{-2})	CO b (km s^{-1})	CN N (10^{12} cm^{-2})	CN b (km s^{-1})	CH N (10^{12} cm^{-2})	CH b (km s^{-1})	CH^+ N (10^{12} cm^{-2})	CH^+ b (km s^{-1})
HD 94454[a]	3.6	2.02	1.3	...	...	9.4	1.6	...	...
HD 96675	4.1	20.18	0.9	4.96	0.5	22.76	1.1	4.90	2.0
HD 99872[a]	3.2	4.54	0.7	...	...	12.6	1.7	23.10	1.9
HD 102065	1.0	...	...	...	...	1.14	0.5	4.97	1.9
	3.8	0.49	1.4	...	...	6.03	1.6	5.78	1.2
HD 106943	−0.8	0.06	0.8	...	...	...	...	...	...
HD 108002[a]	−10.1	0.06	0.4	...	...	...	...	...	...
	1.6	0.35	0.8	...	...	3.2	1.5	...	...
HD 108639	−1.2	0.15	1.0	...	...	...	...	...	...
HD 110434	−5.1	0.04	0.6	...	...	...	...	...	...
	−1.7	0.04	0.3	...	...	...	...	...	...
HD 114886[b]	−27.5	0.09	0.6	...	...	4.	...	6.	...
	−4.3	0.19	1.5	...	...	...	...	13.	...
	−1.9	0.13	1.5	...	...	5.	...	...	...
HD 115071[a]	−3.3	3.40	1.3	...	...	8.2	2.7	...	...
HD 115455[a]	−3.3	1.18	1.0	...	...	17.	3.6	9.06	1.4
	−0.1	...	...	...	...	...	...	3.30	1.0
HD 116852	0.6	0.20	0.5	...	...	1.73	0.5	1.93	1.0
HD 122879	−26.1	...	...	...	...	...	...	3.94	2.2
	−2.5	0.13	1.5	...	...	2.45	1.8	7.24	2.3
HD 124314	−23.6	0.24	1.5	...	...	1.75	0.9	8.59	2.4
	−2.1	1.33	0.8	...	...	7.07	1.7	6.23	2.6
HD 137595[a]	5.4	0.77	1.0	...	...	12.2	3.5	9.63	2.5
HD 140037	1.1	0.41	1.4	...	...	...	...	...	...
HD 144965[a]	4.5	19.35	0.6	...	...	14.4	1.6	7.58	1.9
HD 147683[a]	5.0	0.54	0.3	...	...	2.0	<0.3	11.08	2.5
	6.1	88.55	0.6	...	...	15.2	1.9	5.59	2.8
	11.8	0.18	1.0	...	...	5.0	2.5	2.53	1.6
HD 148937	−13.5	1.07	0.4	...	...	...	...	...	...
	−10.4	2.51	0.7	...	...	...	...	...	...
	3.2	0.23	0.8	...	...	...	...	...	...
HD 152590	−0.5	0.44	0.5	...	...	7.59	1.9	8.45	2.3
	5.3	0.15	1.5	...	...	3.91	3.0	10.69	2.1
HD 152723	2.1	0.10	1.5	...	...	4.06	5.2	2.65	1.5
	7.7	0.05	0.5	...	...	4.20	0.8	3.63	1.9
	10.2	0.43	1.5	...	...	3.70	1.4	4.78	2.2
HD 157857	−5.6	...	...	...	...	...	...	3.37	2.3
	0.0	1.22	0.6	...	...	5.02	1.0	7.88	2.8
	4.2	...	...	...	...	2.83	2.6	8.27	3.0
HD 163758	−3.8	0.24	0.9	...	...	2.25	1.1	...	...
	2.1	...	...	...	...	...	...	1.42	1.0
HD 177989	6.7	0.04	1.0	...	...	...	...	...	...
	10.1	0.45	0.8	...	...	...	...	...	...
	12.1	3.96	0.5	...	...	...	...	...	...
HD 185418[c]	6.8	4.53	0.7	...	...	8.6	1.1	3.9	1.3
	11.0	0.80	0.3	...	...	3.2	0.5	8.6	2.1
HD 190918	2.1	...	...	...	...	1.74	1.5	3.77	1.4
	5.8	0.05	0.3	...	...	...	...	5.51	2.0
	18.3	0.09	1.5	...	...	1.16	0.6	4.74	2.5
HD 192035	1.4	...	...	...	...	2.84	1.0	3.61	2.0
	5.6	10.76	1.0	4.05	0.8	10.12	1.0	4.11	2.0
	9.4	0.81	1.5	...	...	3.53	1.0	...	...
HD 192639[d]	7.3	0.60	1.0	...	...	6.8	1.2	...	...
HD 195965	6.4	0.50	0.5	...	...	...	...	...	...
	10.2	0.70	1.0	...	...	...	...	...	...
HD 198781	−0.1	0.66	0.3	...	...	...	...	...	...
	5.4	15.87	0.4	2.13	0.5	13.17	1.5	3.34	1.7
HD 203532	5.3	45.62	0.6	...	...	9.76	3.1	2.98	2.0
	7.5	...	...	...	...	14.91	1.0	...	...
HD 210121	−6.2	...	...	13.34	0.9	28.61	1.6	5.05	2.8
	−1.7	...	...	...	...	...	...	6.55	1.7
HD 210809	−1.2	0.23	1.5	...	...	1.61	2.0	...	...
	2.8	...	...	...	...	3.86	1.5	7.51	1.7

TABLE 3—*Continued*

Star	v_{LSR} (km s^{-1})	CO N (10^{14} cm^{-2})	CO b (km s^{-1})	CN N (10^{12} cm^{-2})	CN b (km s^{-1})	CH N (10^{12} cm^{-2})	CH b (km s^{-1})	CH^+ N (10^{12} cm^{-2})	CH^+ b (km s^{-1})
HD 220057	−1.8	4.34	1.1	0.96	0.6	8.22	1.3	5.27	3.0
	1.9	...	...	...	...	4.87	2.5	...	...
HD 303308	−7.7	0.10	1.5	...	...	...	...	...	...
	−4.5	0.35	1.4	...	...	5.40	2.9	...	...
	−1.4	0.07	0.3	...	...	...	...	...	...
HD 308813	−2.8	0.69	0.7	...	...	5.09	0.9	...	...

NOTE.—N(CN) is for the R0 line only.
[a] CH results are from Andersson et al. (2002).
[b] CH and CH^+ results are from Gredel (1997).
[c] CH and CH^+ results are from Sonnentrucker et al. (2003).
[d] CH results are from Sonnentrucker et al. (2007).

TABLE 4
NEW TOTAL MOLECULAR COLUMN DENSITIES

Star	log N(cm^{-2}) H_2	References	CO	References	CH^+	References	CH	References	CN	References
BD +48 3437	20.42		13.36		13.18		12.79		11.76	
BD +53 2820	20.15		13.89		12.81		12.61		<11.97	
CPD −69 1743	19.99		13.08		13.18		...		...	
CPD −59 2603	20.15		14.08		13.20		13.08		...	
HD 12323	20.32		14.53		12.90		12.63		12.28	
HD 13268	20.51		14.20		13.18		13.04		12.30	
HD 13745	20.67		13.94		13.52		12.99		11.86	
HD 14434	20.43		14.36		13.38		12.96		11.74	
HD 15137	20.32		13.52		13.15		12.79		<11.62	
HD 23180	20.61	1	14.83	3	12.84		13.28		12.22	
HD 23478	20.57		14.91		12.32		13.34		12.26	
HD 24190	20.38		13.95		13.18		12.98		11.88	
HD 24398	20.67		15.26		12.45		13.32		12.59	
HD 30122	20.70		14.85		12.48		13.20		12.20	
HD 34078	20.88		14.76		13.84		13.90		12.52	
HD 36841	[a]		14.08		12.76		13.00		12.19	
HD 37367	20.61		13.85		13.51		13.08		<11.53	
HD 37903	20.95		13.69		13.11	5	12.96	5	11.90	5
HD 43818	[a]		13.87		13.18		13.04		<11.79	
HD 58510	20.23		13.26		13.08		12.70		<11.71	
HD 63005	20.23		14.00		13.15		12.95		12.15	
HD 91983	20.23		13.79		12.52		...		...	
HD 93205	19.83		13.15		<12.20		12.42		...	
HD 93222	19.84		13.26		...		12.36		...	
HD 93237	19.80		13.40		...		12.08	9	...	
HD 93840	19.28		13.26		12.52		12.26		...	
HD 94454	20.76		14.30		...		12.97	9	...	
HD 96675	20.86		15.28		12.69		13.36		12.80	
HD 99872	20.52		14.65		13.36		13.11	9	<11.79	
HD 102065	20.56		13.69		13.04		12.86		<12.19	
HD 106943	19.81		12.76		...		<12.49	9	...	
HD 108002	20.34		13.66		...		12.51	9	...	
HD 108610	19.86		...		...		<12.56	9	...	
HD 108639	20.04		13.18		...		<12.38	9	...	
HD 110434	19.90		12.94		...		<12.23	9	...	
HD 112999	20.11		<13.23		...		...		...	
HD 114886	20.34		13.61		13.28	6	12.95	6	...	
HD 115071	20.69		14.53		...		12.91	9	...	
HD 115455	20.58		14.08		13.23		13.23	9	<12.20	
HD 116852	19.83		13.30		12.54		12.23		...	
HD 122879	20.36		13.11		13.08		12.38		...	

TABLE 4—*Continued*

Star	log N(cm^{-2})									
	H_2	References	CO	References	CH^+	References	CH	References	CN	References
HD 124314	20.52		14.20		13.18		12.94		...	
HD 137595	20.62		13.89		13.26		13.08	9	<11.90	
HD 140037	19.34		13.61		...		<11.85	9	...	
HD 144965	20.79		15.28		12.88		13.15	9	...	
HD 147683	20.74		15.95		13.28		13.34	9	...	
HD 147888	20.58		15.28		12.88	7	13.34	7	12.32	7
HD 152590	20.51		13.77		13.28		13.08		...	
HD 152723	20.30		13.76		13.04		13.08		...	
HD 157857	20.69		14.08		13.30		12.89		<12.06	
HD 163758	19.85		13.38		12.15		12.34		...	
HD 190918	19.95		13.18		13.15		12.46		<11.53	
HD 192035	20.68		15.15		12.89		13.20		12.71	
HD 192639	20.75	2	13.78		13.61	2	13.45	2	<11.85	10
HD 195965	20.34		14.08		...		...		...	
HD 198781	20.56		15.23		12.52		13.11		12.52	
HD 200775	21.15		17.29		12.97	8	13.51	8	13.08	8
HD 203532	20.70		15.66		12.48		13.40		...	
HD 208905	20.43		14.62		12.78	7	12.73	7	...	
HD 209481	20.54		14.60		12.72	7	12.83	7	...	
HD 209975	20.15		14.04		13.38	7	12.93	7	...	
HD 210121	20.86		15.83	4	13.08		13.46		13.24	
HD 210809	20.00		13.36		12.88		12.74		<11.81	
HD 220057	20.34		14.63		12.87		13.11		12.13	
HD 303308	20.15		13.72		...		12.73		...	
HD 308813	20.30		13.84		...		12.71		...	

Note.—N(CN) includes both R0 and R1. $N1/N0$ is assumed to be 0.41 when R1 is not detected.

[a] HD 36841 and HD 43818 are both predicted here to have log $N(H_2) = 20.4 \pm 0.1$; see § 4.4.

References.—(1) Savage et al. 1977; (2) Rachford et al. 2002; (3) Sheffer et al. 2007; (4) Sonnentrucker et al. 2007; (5) Knauth et al. 2001; (6) Gredel 1997; (7) Pan et al. 2004; (8) Federman et al. 1997a; (9) Andersson et al. 2002; (10) Thorburn et al. 2003.

both CH and CH^+, underscoring the prevalence of low-density gas along these sight lines. The mean of CN components per sight line is smaller, 1.2 ± 0.4. CN is detected along sight lines with the higher values of N(CO) and $N(H_2)$, and then, on average, inside a single component. Among the 15 new CO sight lines with CN detections, 13 (87%) have $N(CO) \geq 14.0$, which is the median value for this sample. There are only three CO components that have CN with no detected CH^+, and seven that are associated with CH^+ but not with CN. We see in § 4.3 that this dichotomy between N(CN) and $N(CH^+)$ can be employed as a good qualitative indicator of n_H.

In the rest of this section we explore the correlations among logarithms of observed column densities by deriving power-law parameters from regression analyses of the form $\log N(M_Y) = \log A + B \log N(M_X)$ (Federman et al. 1990), where M_X and M_Y are two molecular species. Unless otherwise indicated, our BCES least-squares fits (Akritas & Bershady 1996) are done on detections only, excluding the small number of upper limits.

3.2. CO *versus* H_2

Figure 6*a* shows 105 sight lines with CO and H_2 detections taken from our sample and from the samples of Crenny & Federman (2004), Pan et al. (2005), and Sheffer et al. (2007), as well as including results toward bright stars from Federman et al. (2003). A single-slope global correlation returns a slope of $B = 1.89 \pm 0.15$, having a correlation coefficient $r = 0.834$ and confidence level (CL) >99.99% (see Table 5). The first indication of a global correlation between N(CO) and $N(H_2)$ was provided by Federman et al. (1980), who found a B of $\approx$2 for $19 < \log N(H_2) < 21$. Our fit of the new sample also confirms the result of Liszt & Lucas (1998), who plotted N-values of CO and H_2 from an updated version of the Federman et al. (1994) compilation to derive $B = 2.0 \pm 0.3$.

From the start, the need for a variable slope description of CO versus H_2 was present. Federman et al. (1980) found that lower N sight lines have a shallower B of $\approx$1.5, implying a slope break between $20.0 < \log N(H_2) < 20.6$ and between $13.6 < \log N(CO) < 14.8$. Rachford et al. (2002) were the first to analyze higher $N(H_2)$ sight lines from *FUSE*, together with the data from Federman et al. (1994). They showed qualitatively that the slope of H_2 versus CO becomes shallower above $\log N(H_2) \sim 20.5$. According to our inspection of their Figure 3, the slope of the CO versus H_2 relationship appears to get as high as $\approx$3.5. Another exploration of this relationship by Pan et al. (2005) was based on a sample of *FUSE* sight lines toward the Cep OB2 and Cep OB3 associations. Despite gas density differences, these two associations presented similar CO/H_2 slopes that also indicated a steeper relationship for $\log N(H_2) \gtrsim 20$, i.e., $B = 3.2 \pm 0.3$ and 2.9 ± 0.6 toward Cep OB2 and Cep OB3, respectively.

Burgh et al. (2007) examined 19 sight lines and plotted these together with the results of Crenny & Federman (2004) and Pan et al. (2005), confirming that CO versus H_2 was described by a relationship with $B \approx 2$. Likewise, Sonnentrucker et al. (2007) agreed that the overall appearance of CO versus H_2 is as steep as found by Federman et al. (1980), but that it also appears to have a steeper increase of CO with H_2 for $N(CO) \gtrsim 10^{15}$ cm^{-2}, in agreement with the findings of Rachford et al. (2002), Pan et al. (2005), and Burgh et al. (2007).

Overall, the indications are that the log N(CO) versus log $N(H_2)$ relationship is not strictly linear (single sloped), but that the slope

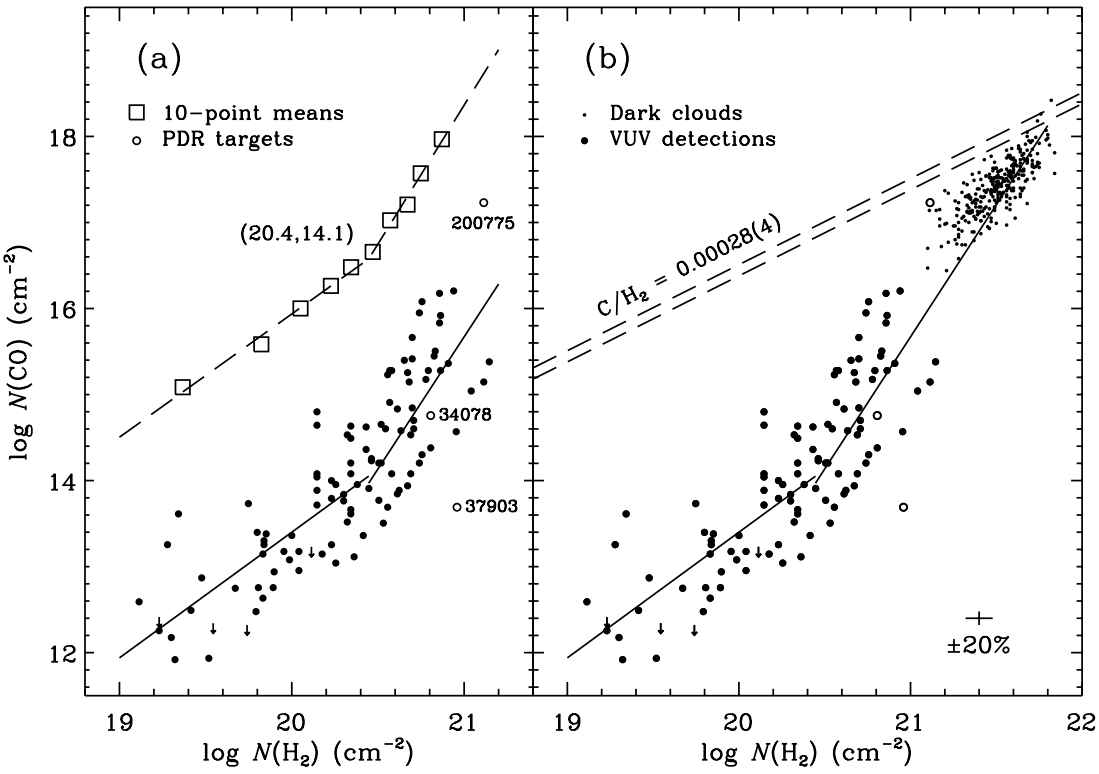

FIG. 6.—CO vs. H_2 for our sample of diffuse clouds. Open circles here and in subsequent figures represent sight lines probing prominent PDRs. In panel (*a*) the sample is fitted with two power laws, as revealed by the 10-point means, with a break at $\log N = (20.4, 14.1)$. Panel (*b*) expands the view to include CO derived for dark clouds (*smaller filled circles*). The steeper slope from (*a*) is seen to pass near the center of the dark-cloud distribution. Practically all CO abundances are found below the highest possible limit set by C/H_2 (1 σ range depicted by the dashed double line).

itself (i.e., the exponent B) is also a function of $N(H_2)$. Indeed, when we restrict the fit to the lower end of the distribution, the returned slope is shallower, while the higher end reveals a steeper slope. In Figure 6*a* we also show the 10-point means of the CO-H_2 sample, revealing a clear signature of two slopes, or a dual power-law correlation between CO and H_2. Using the two slopes to solve for their intersection point, we find that the break between slopes occurs at $\log N(H_2) = 20.4 \pm 0.2$ and $\log N(CO) = 14.1 \pm 0.1$. Finally, employing the break location, we fit the two resulting subsamples to find two highly significant (>4 σ)

TABLE 5
POWER-LAW FITS OF COLUMN DENSITY CORRELATIONS

y	x	n	r	CL (%)	A	B
$\log N(CO)$	$\log N(H_2)$	105	0.834	>99.99	−24.4 ± 3.1	1.89 ± 0.15
	$\log N(H_2) < 20.4$	50	0.734	>99.99	−15.8 ± 4.5	1.46 ± 0.23
	$\log N(H_2) \geq 20.4$	55	0.638	>99.99	−48.8 ± 15.0	3.07 ± 0.73
$\log N(CH)$	$\log N(H_2)$	90	0.906	>99.99	−6.80 ± 1.50	0.97 ± 0.07
	$\log N(H_2) < 20.4$	36	0.799	>99.99	−5.87 ± 3.78	0.92 ± 0.19
	$\log N(H_2) \geq 20.4$	54	0.740	>99.99	−9.34 ± 3.90	1.09 ± 0.19
$\log N(CO)$	$\log N(CH)$	92	0.824	>99.99	−12.3 ± 2.7	2.05 ± 0.21
	$\log N(CH) < 13.0$	42	0.624	>99.99	−5.30 ± 3.8	1.50 ± 0.30
	$\log N(CH) \geq 13.0$	50	0.693	>99.99	−22.3 ± 11.3	2.80 ± 0.85
$\log N(CH^+)$	$\log N(H_2)$	86	0.471	>99.99	4.41 ± 2.06	0.42 ± 0.10
	$\log N(H_2) < 20.3$	26	0.637	99.95	−2.76 ± 4.30	0.78 ± 0.22
	$\log N(H_2) \geq 20.3$	60	0.089	50	10.1 ± 4.3	0.15 ± 0.21
	$\log N(CO)$	88	0.120	73	12.4 ± 0.7	0.04 ± 0.05
	$\log N(CO) < 14.1$	41	0.648	>99.99	6.83 ± 1.29	0.46 ± 0.10
	$\log N(CO) \geq 14.1$	47	0.268	93.1	15.2 ± 1.0	−0.14 ± 0.07
$\log N(CN)$	$\log N(H_2)$	40	0.669	>99.99	−18.5 ± 7.5	1.49 ± 0.36
	$\log N(H_2) < 20.68$	20	0.318	83	−9.0 ± 20.8	1.02 ± 1.02
	$\log N(H_2) \geq 20.68$	20	0.294	79	−11.5 ± 24.9	1.16 ± 1.19
$\log N(CO)$	$\log N(CN)$	42	0.836	>99.99	−2.81 ± 2.77	1.44 ± 0.23
	$\log N(CN) < 12.31$	20	0.453	95.5	2.69 ± 5.02	0.97 ± 0.42
	$\log N(CN) \geq 12.31$	22	0.578	99.5	3.38 ± 5.70	0.96 ± 0.45

NOTE.—BCES($y \mid x$) results from the Akritas & Bershady (1996) code.

correlations (Table 5). Thus, below the break in slope, $\log N(\mathrm{CO}) \propto (1.46 \pm 0.23) \log N(\mathrm{H_2})$, while above it, $\log N(\mathrm{CO}) \propto (3.07 \pm 0.73) \log N(\mathrm{H_2})$. These two slopes are in excellent agreement with previous estimates, confirming all indications that a steeper slope was needed for sight lines with higher values of N.

The global behavior of N(CO) versus $N(\mathrm{H_2})$ may be understood better when the UV data are complemented with N-values for 293 dark clouds detected by millimeter-wave CO emission and taken from the compilation of Federman et al. (1990). We note that $N(\mathrm{H_2})$ values for dark clouds were not directly observed but were inferred (Federman et al. 1990) from the corresponding visual extinction (A_V), which is due solely to $\mathrm{H_2}$ in these clouds. This procedure cannot be applied to diffuse clouds (where $A_V <$ 5 mag) because the (hydrogen) molecular fraction, $f(\mathrm{H_2}) \equiv 2N(\mathrm{H_2})/[N(\mathrm{H\ I}) + 2N(\mathrm{H_2})]$, is <1. As seen in Figure 6*b*, beyond the highest end of the diffuse molecular cloud distribution one encounters the dark clouds, which have higher values of molecular N and of total gas density.

The previous version of this connection between cloud classes was based on only 20 diffuse cloud data points (Federman et al. 1990). At the time of the Federman et al. (1990) study, only five CO values were known above $\log N = 15$, with none available above $\log N = 16$. At this time, however, we have 22 data points with $\log N(\mathrm{CO}) > 15.0$, of which 5 are above $\log N(\mathrm{CO}) = 16$, and 1 (HD 200775) is higher than $\log N = 17$. Thus, during the intervening 18 yr the gap between diffuse sight lines and dark clouds has been filling up with observations. (Simultaneously, recent radio observations are becoming more sensitive in their ability to measure smaller CO column densities that approach the diffuse cloud regime [e.g., Goldsmith et al. 2008].) Not only are the two distributions seen to be stretching toward each other, but the steeper slope of the CO versus $\mathrm{H_2}$ distribution, when extended to higher N, is seen to pass near the center of the dark cloud distribution. However, the rise of N(CO) versus $N(\mathrm{H_2})$ cannot increase without limit because the supply of atomic carbon for CO formation will be exhausted. Thus, the highest possible $\mathrm{CO/H_2}$ ratio is set by $\mathrm{C/H_2} = 2(\mathrm{C/H})$ or $(2.8 \pm 0.4) \times 10^{-4}$, based on the gas-phase C/H abundance from Cardelli et al. (1996) and shown in Figure 6*b* as a double dashed line enclosing the $\pm 1\ \sigma$ range. Only a single datum out of 398 is seen to be slightly above the $\mathrm{C/H_2}$ limit.

One may need to go beyond fits with linear logarithmic slopes in order to allow for a better description of the CO-$\mathrm{H_2}$ relationship. Our test of a fourth-order polynomial fit returned a continuously variable slope that ranged from $B = 0.8$ to 3.4 for the lowest to highest N(CO) values in the sample of diffuse clouds, at which point the slope declined while "connecting" with the dark cloud distribution. Such higher order fits can only approximate the more realistic slopes predicted by detailed CO photochemistry models. Both Rachford et al. (2002) and Sonnentrucker et al. (2007) noted the agreement between the observed trend of CO versus $\mathrm{H_2}$ and results from the CO photochemical modeling of van Dishoeck & Black (1988) for the CO-rich sight lines with $\log N(\mathrm{CO}) \gtrsim 15$. In Figure 7 we show that the theoretical models of "translucent clouds" from van Dishoeck & Black (1988) provide a functional variation that closely mimics the observed distribution of both diffuse and dark clouds, as well as along the transition region (i.e., their relative locations on the plot). These curves have steeper slopes than those obtained in our fourth-order polynomial fit, reaching as high as $B = 4.3$, 5.4, or 7.3 for the $I_{\mathrm{UV}} = 0.5$, 1.0, or 10 models, respectively, where I_{UV} denotes the enhancement factor over the mean interstellar UV radiation field. All three curves end up at the highest column densities with B between 1.5 and 1.9, i.e., bracketing the dark-cloud slope of

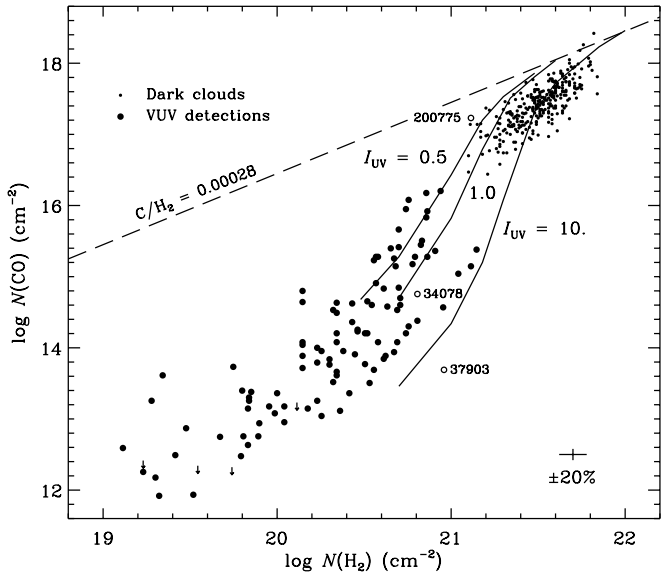

FIG. 7.—CO vs. $\mathrm{H_2}$ distribution for diffuse and dark clouds compared with the H ($I_{\mathrm{UV}} = 0.5$), T (1.0), and I (10) theoretical models for translucent clouds from van Dishoeck & Black (1988). Note the overall agreement between the shape of model curves and the transition region from diffuse to dark cloud regimes, as well as with the observed slopes of each type of clouds.

$B = 1.62 \pm 0.07$. Our modeling with Cloudy of the CO versus $\mathrm{H_2}$ relationship that results from $\mathrm{CH^+}$ chemistry is described in § 6.

3.3. CH *versus* $\mathrm{H_2}$ (*and* CO *vs.* CH)

Based on 19 data points, Federman (1982) demonstrated that N(CH) is proportional to $N(\mathrm{H_2})$, finding a slope of 1.0 ± 0.1, while Danks et al. (1984) confirmed this result by finding a slope of 0.85 ± 0.15 based on a slightly larger sample with lower S/N data. (A combination of the two samples resulted in a slope of 0.90 ± 0.10.) As for CO, Rachford et al. (2002) presented this relationship qualitatively, confirming its nearly linear appearance and its agreement with the models of van Dishoeck & Black (1989) for the highest values of N(CH) and $N(\mathrm{H_2})$. A slope of 0.95 ± 0.10 was found by Pan et al. (2005) toward 11 stars in Cep OB2, but the only four data points that were available from the Cep OB3 sample did not provide a clear case for a CH versus $\mathrm{H_2}$ correlation. Our log-log plot of CH relative to $\mathrm{H_2}$ (Fig. 8) shows a well-correlated 90-point sample with a single slope of $B = 0.97 \pm 0.07$. Thus, CH is definitely linearly related to $\mathrm{H_2}$, but as is the case with CO, the width of the correlation is appreciably larger than individual measurement uncertainties. These correlations have CL above 99.9%, and thus our methodology used in § 2.5, of importing CH cloud structures into spectrum syntheses of $\mathrm{H_2}$, is vindicated.

Consequently, the ratio $\mathrm{CH/H_2}$ is a quantity that shows no correlation with $\mathrm{H_2}$. Our sample average is $\mathrm{CH/H_2} = 3.5^{+2.1}_{-1.4} \times 10^{-8}$, or $\log(\mathrm{CH/H_2}) = -7.46 \pm 0.21$. This value can be seen to agree well with the data plotted in Figure 2 of Federman (1982). Thus, $N(\mathrm{H_2})$ can be predicted from optical observations of N(CH), possibly with the exception of certain prominent photon-dominated, or photodissociation, regions (PDRs). The PDR targets HD 34078 and HD 37903 are found on the outskirts of the distribution, deviating from the average by about +3 and $-2.5\ \sigma$, respectively.

It would be interesting to include CH and $\mathrm{H_2}$ values for dark clouds to see how they relate to the plotted distribution of diffuse sight lines. Mattila (1986) found that $N(\mathrm{CH})/N(\mathrm{H_2}) = 10^{-7.4}$

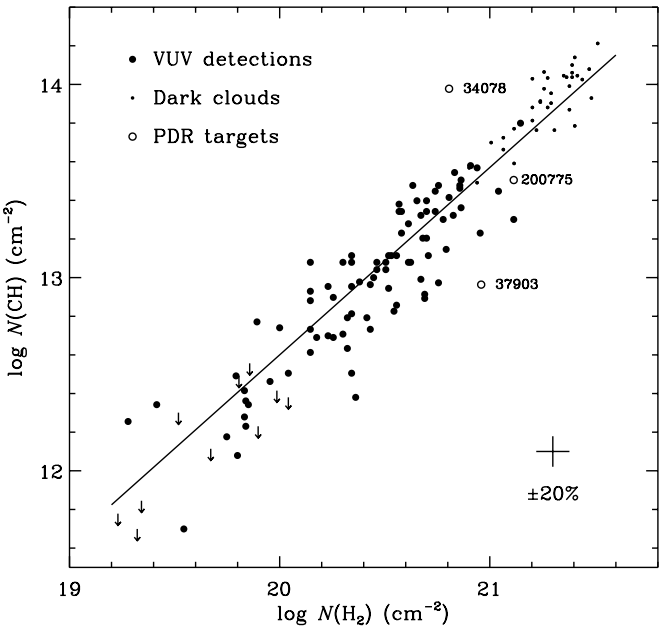

FIG. 8.—CH column density shown to have a linear correlation with $N(H_2)$, characterized by a single slope of 0.97 ± 0.07. The optical data fit is seen to match the Mattila (1986) dark cloud extension of the CH vs. H_2 relationship. The abundance ratio CH/H_2 is constant at 3.5×10^{-8}.

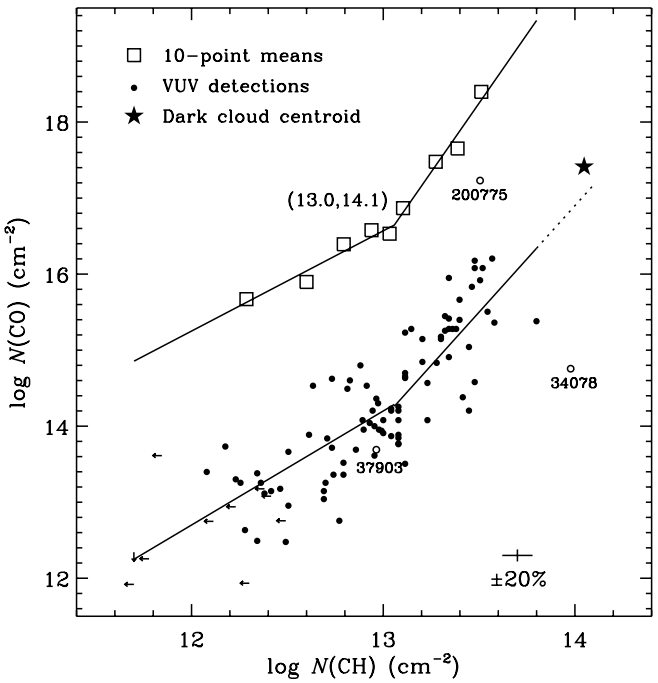

FIG. 9.—Since CH has been shown to be linearly related to H_2, it can serve as a proxy for the amount of H_2 along the line of sight. Thus, we see that CO has a dual-slope relationship with CH as it has with H_2 (cf. Fig. 6). As with H_2, the slope is steeper for larger column densities, pointing toward the location of CO dark clouds. The break in slopes is found at $\log N(CH) = 13.0$ and $\log N(CO) = 14.1$, in excellent agreement with the CO vs. H_2 break found in Fig. 6 and with $\log \langle CH/H_2 \rangle = -7.5$.

for a small sample of dark clouds, i.e., in excellent agreement with our average above for diffuse molecular clouds. Mattila (1986) compared CH versus H_2 for both types of clouds and found that they are in complete agreement, the dark cloud data being a monotonic extension of the CH-H_2 diffuse cloud relationship, with a global slope of $B = 1.02 \pm 0.04$. This is confirmed here with the inclusion of the Mattila (1986) sample of dark clouds in Figure 8, yielding $B = 1.03 \pm 0.03$. [This relationship breaks down, however, for dense molecular cloud cores with $N(H_2) \gtrsim 3 \times 10^{22}$ cm^{-2} (Mattila 1986).] In summary, the linear relationship between CH and H_2 for diffuse and dark molecular clouds is bound to be very useful for determinations of $N(H_2)$ along sight lines where no CO data are available, or to corroborate such determinations based on CO data, as we show in § 4.4.

The tight correspondence between CH and H_2 was employed by Magnani & Onello (1995) in order to derive $N(H_2)$ from millimeter-wave detections of N(CH) toward diffuse and dark molecular clouds. Thus, they were able to find variation by a factor of 20 in X_{CO} for diffuse clouds ($A_V < 4$). Another relationship between CH and $E(B - V)$ was presented by Magnani et al. (2003) showing that while $N(H_2)$ can be predicted from millimeter-wave CH and reddening measurements, CO cannot be derived from linear relationships with these parameters. Reddening values were already known to correlate with the total proton density $N(H) = N(H\ I) + 2N(H_2)$ in diffuse clouds (Bohlin et al. 1978), and with $N(H_2)$ along translucent sight lines (Rachford et al. 2002).

The linear relationship between CH and H_2 means that a plot of CO versus CH should be similar to the plot of CO versus H_2. Indeed, our single-slope fit of 92 data points shows that $B = 2.05 \pm 0.21$, i.e., N(CO) varies as the square of N(CH). Originally, Federman & Lambert (1988) fitted a sample of 19 data points to find $B = 1.97$ for CO versus CH. Employing a sample twice as large, this quadratic relationship was confirmed by Federman et al. (1994), who commented that above about $N(CH) \sim 3 \times 10^{13}$ and $N(CO) \sim 10^{15}$ cm^{-2}, N(CO) is increasing more rapidly (higher B). In our sample, which is more than double in size yet again, one can see (Fig. 9) that the slope appears to be increasing above $\log N(CH) \sim 13.3$ and $\log N(CO) \sim 15$ toward the locus of HD 200775, in very good agreement with Federman et al. (1994), who also noted the outlying position of the PDR sight line toward AE Aur (HD 34078).

Sonnentrucker et al. (2007) found a single slope of $B = 4.0 \pm 0.3$ for a CO versus CH sample that tended to have higher column densities, i.e., mostly with $\log N(CO) > 14$ and $\log N(CH) > 13$. In fact, as shown in Figure 9, the 10-point means of our sample reveal the presence of two slopes with CL > 99.99%, $B = 1.50 \pm 0.30$ and 2.80 ± 0.85, below and above a break at $\log N(CH, CO) = (13.0, 14.1)$, respectively. There is excellent agreement with the power-law break found for CO versus H_2, since, according to the CH/H_2 ratio found above, $\log N(CH) = 13.0$ corresponds to $\log N(H_2) = 20.5$. As is the case for CO versus H_2, the steeper power law can be extended to reach near the center of the dark cloud distribution, which was plotted after converting its H_2 coordinate into a CH location. These characteristics of the CO versus CH plot confirm that CH can be used as a dependable proxy for H_2 and that a distinct change in CO photochemistry occurs at $\log N(CO) = 14.1 \pm 0.1$.

3.4. CH^+ *versus* H_2 (*and* CH^+ *vs.* CO)

Federman (1982) also compiled and plotted 25 sight lines with detected CH^+ and $\log N(H_2) > 19$, finding an insignificant correlation ($r = 0.3$ and CL < 90%) with an unspecified B. Rachford et al. (2002) also found a linear relationship between the two species, but with much increased scatter above $\log N(H_2) \sim 20$. They commented that Gredel (1997) found $N(CH^+)$ and N(CH) to be correlated, which in light of the tight correlation between CH and H_2 presented in the previous section

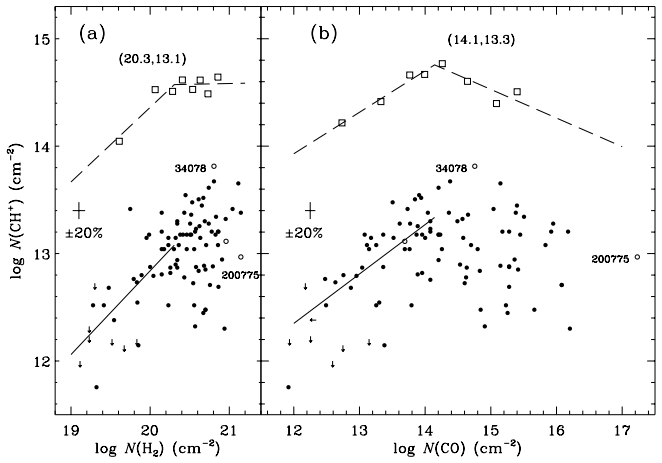

FIG. 10.—Two relationships between CH^+ and the most abundant diatomic molecules. In panel (*a*), $\log N(CH^+)$ is seen to be correlated with $\log N(H_2) \leq 20.3$. Similarly in (*b*), CH^+ is seen to be well correlated with CO below $\log N = 14.1$. These two power-law breaks are in excellent agreement with the break of CO vs. H_2 (Fig. 6), as well as in excellent mutual agreement that the CH^+ abundance stops increasing at $\langle \log N \rangle = 13.2 \pm 0.1$. The unlabeled PDR sight line belongs to HD 37903.

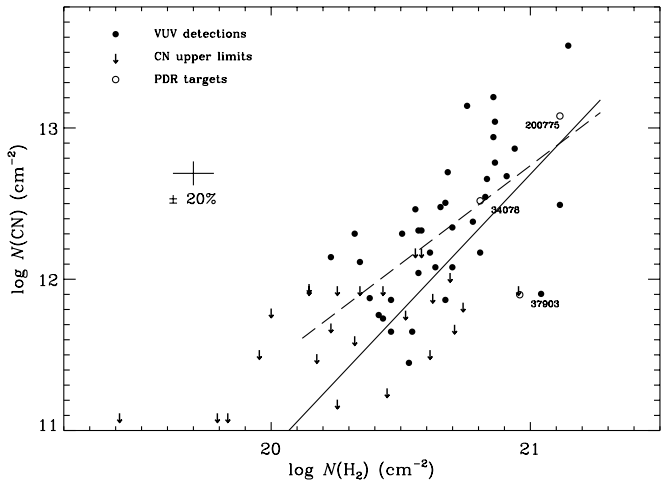

FIG. 11.—Fitting CN detections only vs. H_2 returns a slope of $B = 1.5 \pm 0.4$ (*dashed line*). A slope of $B = 1.8 \pm 0.3$ results from using the Buckley-James regression method for censored data.

is consistent with a correlation between CH^+ and H_2. Indeed, our sample of 86 points returns a single-slope $B = 0.42 \pm 0.10$ with CL > 99.99%, confirming that a global correlation exists between CH^+ and H_2.

However, in agreement with Rachford et al. (2002), the current sample also shows a marked increase in data scatter or a loss of correlation above $N(H_2) \approx 2. \times 10^{20}$ cm^{-2}. Figure 10*a* shows that employing 10-point means reveals yet another broken-slope relationship, with $B = 0.78 \pm 0.22$ for $\log N(H_2) < 20.3$ and $B = 0.15 \pm 0.21$ above that break. The steeper power law indicates (at CL = 99.95% or 3.5 σ) that CH^+ varies nearly linearly with H_2 at lower column densities. Above the break in slope, which is in excellent agreement with the H_2 break from Figure 6, both *B* and its CL indicate that CH^+ and H_2 are no longer correlated.

Lambert & Danks (1986) presented correlations between $\log N(CH^+)$ and $\log N(H_2^*)$, i.e., column densities of excited states of H_2 involving the $J = 3$ and 5 levels. Here we are unable to confirm these findings because for our sight lines we do not find any CH^+ and H_2^* correlations for all $J = 1$–4 levels. However, we note that the Lambert & Danks (1986) study included sight lines with a range of *N*-values much larger than ours, including sight lines that are H_2 poorer by at least 3 orders of magnitude than those studied here. We comment further about excited H_2 in § 6.2 when discussing the formation of CH^+.

When CH^+ is plotted against CO, the behavior is similar to that found just above for CH^+ versus H_2, namely, presenting a slope break that is flanked by two different power-law fits (Fig. 10*b*). Below $\log N(CO) = 14.1$ we find $B = 0.46 \pm 0.10$ (CL > 99.99%), while above the break $B = -0.14 \pm 0.07$ (CL = 93%). Again, showing excellent agreement with the CO break in Figure 6, CH^+ is definitely correlated with CO for lower column densities but is insignificantly (1.8 σ) anticorrelated with CO above the break. We believe that this behavior reflects the importance of CH^+ reactions when *N*(CO) is low, so that a different production route operates at higher *N*(CO). It is interesting to note further that with $\log N(CH^+) \propto B_1 \log N(H_2)$ and with $\log N(CH^+) \propto B_2 \log N(CO)$, one expects $\log N(CO)$ to be $\propto (B_1/B_2) \log N(H_2)$. Thus, $0.78/0.46 = 1.7 \pm 0.6$ is in excellent agreement with $B = 1.46 \pm 0.23$ found in § 3.2 for the low-*N* sight lines. Finally, both CH^+ breaks relative to H_2 (Fig. 10*a*) and to CO (Fig. 10*b*) are in complete mutual agreement that the abundance of CH^+ presents a power-law change at $\log N = 13.2 \pm 0.1$. A more detailed and chemically motivated treatment of CH^+ and its relationships with H_2 and CO is provided in § 6 based on numerical modeling with Cloudy and the incorporation of a nonequilibrium term in the chemical formation of CH^+.

3.5. CN *versus* H_2 (*and* CO *vs.* CN)

CN detections here encompass a smaller sample that includes less than half of the sight lines that are included in the H_2, CO, CH, and CH^+ samples. Federman et al. (1984) analyzed a smaller sample still and concluded that the CN abundance was proportional to the third power of H_2. Rachford et al. (2002) showed that a strong correlation exists here as well, with an estimated $B \sim 2.5$ according to our inspection. Such steep slopes are not confirmed here because we find $B = 1.5 \pm 0.4$ from our regression fit, with $r = 0.67$ (CL > 99.99%). However, owing to the relatively large number of upper limits on CN, we decided to employ the Buckley-James method of linear regression with censored data, available from the ASURV statistical package (Isobe et al. 1986). This fit returned a steeper slope of $B = 1.8 \pm 0.4$ (Fig. 11), which was also confirmed by the EM algorithm and by Schmitt's method, but is also appreciably shallower than $B \approx 3$. One possible explanation for the disagreement among fitted slopes may involve the smaller number of sight lines with detected CN in previous studies. Our sample includes 40 sight lines with detected CN, and as a result there is a significant "re"population of the plot with $\log N(H_2) < 20.5$. However, the sample is still too small and restricted in range to reveal information about any power-law break. Thus, arbitrarily breaking the sample at midpoint results in similar slopes, both of which have CL below 90% (Table 5).

Figure 12 shows the run of $\log N(CO)$ versus $\log N(CN)$ with $B = 1.4 \pm 0.2$, fitting the CN detections only. This 42-point sample has $r = 0.84$ and thus CL > 99.99%. Again, owing to the presence of 17 CN upper limits, we employed the Buckley-James censored-data fit and derived $B = 1.9 \pm 0.2$, a slope that seems to treat the upper limits as quasi-detections. On the other hand, using the Schmitt method returned a fit with the significantly lower $B = 0.8 \pm 0.2$, which seems to exclude all upper

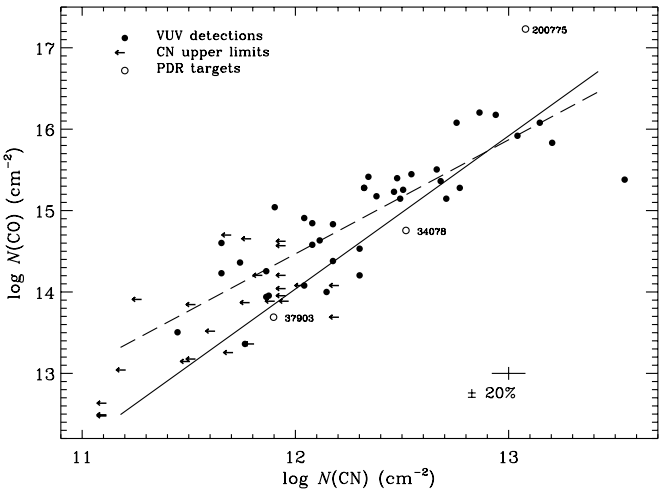

FIG. 12.—Two heavier diatomic molecules, CO and CN, shown to be well correlated. This confirms earlier clues that CO and CN are found together in the same colder and denser clumps of gas. The dashed line shows a fit of CN detections only with $B = 1.4 \pm 0.2$, and the solid line is a Buckley-James regression that includes all CN upper limits (censored data, $B = 1.9 \pm 0.2$).

limits in the independent variable (i.e., in CN). Thus, our result based on detections only is bracketed by the two slopes based on censored-data methods. A smaller sample of (uncensored) 31 points was presented by Sonnentrucker et al. (2007), yielding (in an unweighted fit) $B = 1.5 \pm 0.1$ and $r = 0.90$ (CL > 99.9%), thus agreeing more with our detections-only fit than with our Buckley-James fit. Again, splitting the sample into two equal subsamples returns two $\lesssim 2\ \sigma$ fits with identical slopes, i.e., with no evidence for a break. Since the CN sample is derived for the most part from high-N sight lines that are above the CO versus H_2 break, consistency is still preserved.

4. DERIVED PHYSICAL CONDITIONS

4.1. *UV Shielding of* CO

Earlier (§ 3.2) we described the finding of a power-law break in the correlation analysis of CO versus H_2 at $\log N = 14.1$ versus 20.4. This break in slope was also confirmed above through analysis of CO versus CH, CH^+ versus H_2, and CH^+ versus CO. This power-law break corresponds to a change in CO photochemistry. Our value is similar to $\log N(\mathrm{CO}) \gtrsim 14$ found by Frerking et al. (1982) for two CO isotopologues, $C^{18}O$ and ^{13}CO, through their correlations with A_V in molecular clouds. In addition, a value of $\log N(\mathrm{CO}) \gtrsim 14$ was supported by the self-shielding computations of Bally & Langer (1982), who showed the importance of line photodissociation in steepening the increase of N(CO) with depth into a molecular cloud.

Van Dishoeck & Black (1988) presented the most detailed modeling of CO photochemistry in the regime of translucent (1 mag $< A_V <$ 5 mag) sight lines. In § 3.2 (and Fig. 7) we also compared the observed distribution of diffuse and dark clouds with three families of van Dishoeck & Black (1988) models for translucent sight lines differing in I_{UV}. This showed the good global agreement of abundance trends for CO versus H_2. In their modeling, van Dishoeck & Black (1988) incorporated a detailed description of numerous CO absorption bands in the far-UV, owing to their importance in diminishing CO photodissociation rates through self-shielding. This detailed band structure was also needed for precise accounting of the shielding of CO bands by H_2 absorption lines, since the total UV shielding of CO is controlled by both N(CO) and $N(H_2)$. This two-parameter shielding

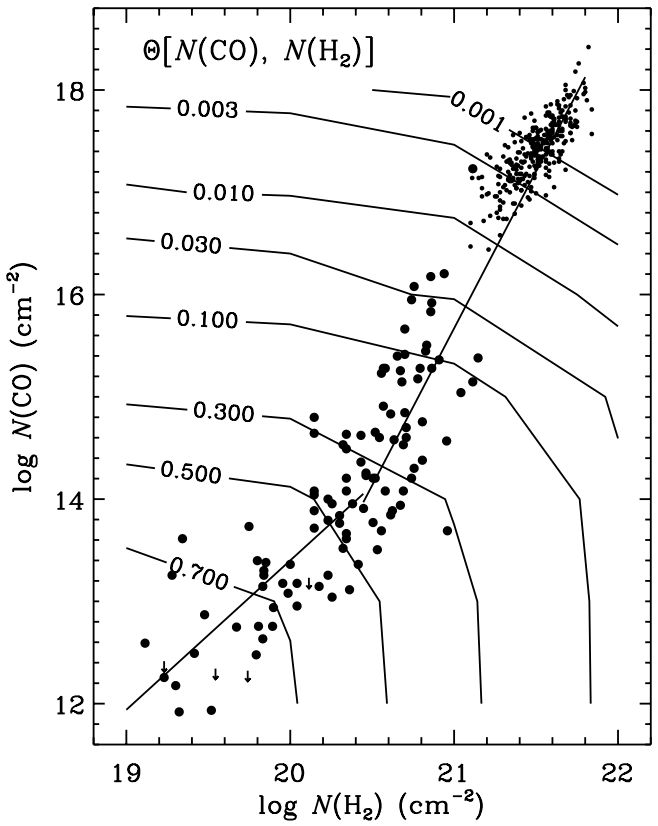

FIG. 13.—Interpolated values of the shielding function Θ of van Dishoeck & Black (1988) plotted as contours over the observed distribution of N(CO) vs. $N(H_2)$. UV shielding plays a role in the steepening slope beyond $\log N(\mathrm{CO}) \approx 15$.

function of CO, Θ, was tabulated in Table 5 of van Dishoeck & Black (1988). The values of Θ are smaller than 1 since they provide the reduction in the photodissociation rate of CO. When $\Theta \lesssim 0.1$, or $\log N(\mathrm{CO}) \gtrsim 15$, total UV shielding of CO results in rapid steepening of the CO versus H_2 relationship.

In order to determine the effect that Θ has on the observed distribution of CO versus H_2, we present again in Figure 13 the global view of the diffuse and dark cloud distribution, together with our dual power-law fits, all overlaid by contours of theoretical Θ-values based on an interpolation of Table 5 of van Dishoeck & Black (1988). It can be seen that for decreasing values of Θ the values of N(CO) are increasing, as the photodestruction of the molecule is being diminished. This provides a demonstration of the applicability of the van Dishoeck & Black (1988) shielding function to diffuse and dark sight lines. Quantitatively, the location of the slope break at $\log N(H_2, \mathrm{CO}) = (20.4, 14.1)$ is seen to be near $\Theta \approx 0.4$, i.e., where the reduction in the photodissociation of CO equals 1 mag. Here we interpret the slope break as the locus of a transition between lower density and higher density regimes, but the comparison with Θ suggests some contribution from the UV shielding of CO to the steepening of the slope near the break. Future calculations of Θ, which should include updated f-values of predissociating CO bands (Federman et al. 2001; Sheffer et al. 2003; Eidelsberg et al. 2004, 2006), may clarify the association between Θ and the observed break in the slope of CO versus H_2.

4.2. *Excitation Temperatures*

Each molecule in the ISM is influenced both by collisions with other molecules and atoms (matter) and by interactions with

photons (radiation). The former processes will tend to thermalize the internal level populations of the molecules so that their T_{ex} will reflect the kinetic energy of the colliding gas particles. Such a case is reflected in the $J = 0$ and 1 populations of H_2 owing to the lack of permitted dipole transitions that lead to cooling of the molecule. As can be seen in Table 6, H_2 along all sight lines has relatively high values of $T_{ex}(J = 0, 1)$ (hereafter T_{01}) since they reflect the prevailing kinetic temperature of the gas. The average of 56 sight lines with newly derived H_2 parameters is $T_{01}(H_2) = 76 \pm 14$ K, which is in excellent agreement with the Savage et al. (1977) result of 77 ± 17 K. As we pointed out in Sheffer et al. (2007), sight lines with lower T_{01} values for H_2 are associated with detected amounts of ^{13}CO. The subsample of 25 sight lines with ^{13}CO was shown to have an average $T_{01}(H_2)$ that is 20 K below the average T_{01} for sight lines without detected ^{13}CO. The entire sample here is not constrained by the presence of ^{13}CO, just like the original sample of Savage et al. (1977).

The Y. S. Ismod.f code also returned fitted T_{ex} values for the higher J levels of H_2, as listed in Table 6. A cursory inspection shows that for H_2, as detected in diffuse molecular gas, $T_{01} < T_{02} < T_{03} < T_{04}$. This is confirmed by their means from all sight lines: 76 ± 15, 101 ± 15, 140 ± 23, and 213 ± 31 K, respectively. As can be seen in Figure 14, logarithmic correlations exist between each T_{0J} (for $J > 1$) and T_{01}, all with CL $> 99.99\%$. The respective slopes of the regressions are mutually identical within their uncertainties: $B = 0.48 \pm 0.07$, 0.52 ± 0.09, and 0.46 ± 0.08, in order of increasing J. The positive slopes may be indicating a connection between increasing T_{0J} and decreasing gas density at cloud edges, where there is more efficient pumping by far-UV photons.

CO presents the opposite case of subthermal excitation, with T_{ex} values rarely rising above ≈ 5 K. The only interesting case of warmer CO is found along the ρ Oph D (HD 147888) sight line: $T_{01}(CO) = 13.6$ K. In this case the CO being probed is near the ρ Oph molecular cloud, and CO emission from the latter is able to raise $T_{ex}(CO)$ along the diffuse part of the cloud (Wannier et al. 1997). The average $T_{01}(CO)$ from 61 (62) sight lines without (with) ρ Oph D is 3.5 ± 0.7 (3.6 ± 1.5) K. Slightly higher values are found for $T_{02}(CO) = 4.2 \pm 0.8$ (4.4 ± 1.4) K and $T_{03}(CO) = 5.3 \pm 1.3$ (6.0 ± 2.0) K, without (with) ρ Oph D, but more likely showing that $T_{ex}(CO)$ is constant within the uncertainties. We also see no dependence of $T_{01}(CO)$ on the density indicator CN/CH^+ (§ 4.3). Furthermore, the same mean value for $T_{01}(CO)$ is found for sight lines with or without detected CN, despite a density difference of a factor of 10. These differences from $T_{ex}(H_2)$ arise because in diffuse molecular clouds densities remain below the critical density of ~ 2000 cm^{-3} for CO.

4.3. *Total Gas Density: Empirical Indicators*

The total gas (proton) density, $n_H \equiv n(H\ I) + 2n(H_2)$, controls the chemical reaction networks via the density dependence of molecule production terms and thus affects the resultant molecular abundances. We may explore such density effects by deriving n_H for sight lines in a variety of ways. The simplest and most empirical involves the ratio of two observables, $N(CH)$ and $N(CN)$. Cardelli et al. (1991) showed that the CN/CH ratio is correlated with n_H^2 since CN is formed inside denser and colder clumps of gas out of preexisting CH. Thus, plotting other quantities versus CN/CH is tantamount to showing the relationship of those quantities with n_H (Sonnentrucker et al. 2007).

As is reinforced below, the CH^+ molecule is typically formed in lower density regimes, leading to a dependence opposite to that of CN. This was shown empirically by Cardelli et al. (1990), who found that CN/CH was anticorrelated with CH^+/CH. Thus, instead of using CH, which is less dependent on density thanks to its connection to gas containing CN or CH^+ (Lambert et al. 1990; Pan et al. 2005), CN/CH^+ should be a more effective indicator of the density than the CN/CH ratio. In Figure 15 we show that both empirical density indicators are well correlated with each other ($r = 0.77$, CL $> 99.99\%$). Note, however, that CN/CH extends over less than 2 orders of magnitude, whereas CN/CH^+ spans 3 orders, suggesting that CN/CH^+ responds better to changes in n_H, a picture consistent with the presence of CH in both high- and low-n_H gas.

Figure 16*a* shows the abundance of CO relative to H_2 versus the empirical density indicator CN/CH. With $r = 0.60$ the plot shows a very good correlation (CL $> 99.99\%$) between the two quantities, having $B = 1.16 \pm 0.25$. For comparison, Figure 16*b* shows CO/H_2 versus CN/CH^+, and the correlation is found to be even tighter, having a larger r of 0.78 and $B = 0.85 \pm 0.11$. Similar plots of species other than CO also exhibit larger r-values and visibly tighter relationships, confirming the better role of CN/CH^+ in sorting diffuse sight lines according to n_H. Furthermore, the tighter correlation seen in Figure 16*b* is an indication that the CO/H_2 ratio is controlled significantly by the local gas density.

Given the better association between n_H and the observed CN/CH^+ ratio, one may imitate a three-dimensional (3D) plot by employing proportionately sized symbols to represent values of the latter quantity on the two-dimensional (2D) surface of, e.g., the $N(CO)$ versus $N(H_2)$ plot that was shown in Figure 6. From the resulting Figure 17 one can discern two general trends involving variations in gas density (as given by CN/CH^+). First, density is clearly the lowest toward the lower left corner of the plot (where many of the values are upper limits) and vice versa, showing that both $N(CO)$ and $N(H_2)$ are correlated with n_H. Second, the density clearly varies in an orthogonal direction to its first gradient; i.e., it is increasing from the lower envelope to the upper envelope of the distribution.

Federman et al. (1980) were the first to find that the dispersion in the relationship of CO versus H_2 is significantly larger than the measurement uncertainties associated with individual data points, as confirmed in Figure 6. These authors were also able to show that applying high-density and low-density chemical models to this relationship indicated that its width was affected by gas density, such that n_H is higher at the upper envelope, in agreement with our findings using CN/CH^+ as the density indicator.

The two Cepheus samples in Pan et al. (2005) appeared to occupy nonoverlapping positions on the CO versus H_2 plot. However, when compared with the current, much larger sample that includes the sight lines from Pan et al. (2005), all Cep OB2 (having higher density gas) and Cep OB3 (lower density) data points are part of the global distribution of points, although they seem to belong to the upper and lower envelopes of the distribution, respectively, thus providing more support to the overall picture.

Recently, Liszt (2007) suggested that the CO versus H_2 relationship in diffuse clouds directly reflects the formation of CO from an HCO^+ precursor. However, while the second (crosswise) variation agrees qualitatively with the models of Liszt (2007; see his Fig. 1), those models do not reproduce the first variation, i.e., the rise in density in tandem with increasing N-values. In fact, the Liszt (2007) models have *constant* density values between the lower left and upper right corners of the CO versus H_2 plot. Perhaps this difference is an indication that Liszt's assumption that CO production is controlled by recombination of HCO^+ with a constant abundance of 2×10^{-9} relative to H_2 is inadequate.

TABLE 6

NEW INTERSTELLAR EXCITATION TEMPERATURES FOR H_2 AND CO

Star	$T_{01}(H_2)$ (K)	$T_{02}(H_2)$ (K)	$T_{03}(H_2)$ (K)	$T_{04}(H_2)$ (K)	T_{01}(CO) (K)	T_{02}(CO) (K)	T_{03}(CO) (K)
BD +48 3437	83.	113.	158.	246.	2.7	...	...
BD +53 2820	93.	120.	176.	244.	3.3	...	...
CPD −69 1743	79.	102.	143.	213.	2.7	...	...
CPD −59 2603	77.	95.	142.	217.	3.0	3.3	...
HD 12323	82.	101.	142.	217.	3.1	4.3	...
HD 13268	92.	120.	167.	245.	3.4	...	...
HD 13745	66.	93.	128.	202.	4.0	...	...
HD 14434	99.	129.	166.	247.	4.4	...	...
HD 15137	104.	111.	153.	245.	3.1	4.2	...
HD 23478	55.	79.	101.	171.	3.4	3.6	4.2
HD 24190	66.	86.	119.	193.	3.1	3.5	...
HD 24398	...	...	...	...	3.4	3.8	4.3
HD 24534	54.	73.	96.	152.	...	...	...
HD 27778	51.	78.	103.	152.	5.3	5.5	5.6
HD 30122	61.	86.	121.	185.	3.8	4.0	...
HD 34078	75.	92.	128.	206.	...	...	...
HD 36841	...	...	...	...	2.7	3.0	...
HD 37367	73.	82.	112.	185.	3.2	...	...
HD 37903	64.	121.	125.	190.	2.7	...	...
HD 43818	...	...	...	...	4.1	...	...
HD 58510	90.	99.	143.	212.	2.9	...	...
HD 63005	78.	91.	129.	188.	3.6	...	...
HD 91983	61.	105.	144.	222.	2.7	...	...
HD 93205	97.	118.	167.	241.	2.8	...	...
HD 93222	69.	109.	162.	218.	3.3	...	...
HD 93237	58.	85.	111.	135.	3.1	...	...
HD 93840	54.	112.	170.	224.	3.1	...	...
HD 94454	74.	83.	106.	167.	3.8	...	...
HD 96675	...	...	...	...	3.7	5.9	...
HD 99872	66.	94.	114.	179.	3.7	3.8	...
HD 102065	...	...	...	...	3.6	...	...
HD 106943	96.	108.	142.	214.	2.7	...	...
HD 108002	77.	98.	133.	218.	3.2	...	...
HD 108610	80.	106.	138.	208.	...	...	...
HD 108639	88.	111.	153.	219.	3.0	...	...
HD 110434	87.	105.	144.	216.	2.7	...	...
HD 112999	96.	102.	140.	231.	3.0	...	...
HD 114886	92.	109.	151.	214.	3.1	...	...
HD 115071	71.	95.	133.	208.	3.7	...	...
HD 115455	81.	96.	128.	200.	2.9	...	...
HD 116852	66.	98.	147.	200.	3.2	...	...
HD 122879	90.	105.	148.	200.	2.9	...	...
HD 124314	74.	98.	138.	208.	3.8	...	...
HD 137595	72.	94.	124.	197.	3.9	4.4	...
HD 140037	...	...	...	...	2.9	...	...
HD 144965	70.	91.	125.	203.	4.3	5.3	...
HD 147683[a]	58.	85.	116.	185.	5.2	6.5	6.9[a]
HD 147888	44.	90.	110.	181.	13.6	9.3	9.0
HD 148937	69.	97.	132.	228.	3.7	4.4	5.6
HD 152590	64.	87.	125.	205.	4.1	...	...
HD 152723	76.	96.	141.	201.	4.0	...	...
HD 154368	47.	95.	...	...	3.0	4.3	...
HD 157857	86.	99.	133.	203.	4.6	...	...
HD 163758	79.	142.	204.	277.	4.0	...	...
HD 177989	49.	85.	127.	198.	3.3	3.5	...
HD 190918	102.	156.	214.	310.	2.7	4.0	...
HD 192035	68.	92.	126.	205.	3.2	3.9	...
HD 195965	91.	103.	136.	214.	3.0	...	...
HD 198781	65.	92.	128.	191.	3.4	3.7	...
HD 200775	44.	104.	104.	168.	...	...	...
HD 203532	47.	78.	102.	169.	5.3	4.8	...
HD 208905	77.	97.	132.	214.	6.0	...	...
HD 209481	78.	97.	137.	215.	2.9	...	...
HD 209975	73.	104.	149.	243.	2.9	...	...

TABLE 6—*Continued*

Star	$T_{01}(H_2)$ (K)	$T_{02}(H_2)$ (K)	$T_{03}(H_2)$ (K)	$T_{04}(H_2)$ (K)	$T_{01}(CO)$ (K)	$T_{02}(CO)$ (K)	$T_{03}(CO)$ (K)
HD 210121	51.	83.	108.	178.	...	...	...
HD 210809	87.	126.	187.	278.	3.1	...	...
HD 220057	65.	87.	122.	192.	3.0	3.8	...
HD 303308	91.	121.	177.	300.	3.1	...	...
HD 308813	73.	92.	129.	181.	3.8	...	...

[a] HD 147683 presents higher J lines with $T_{04}(CO) = 7.7$ K and $T_{05}(CO) = 8.5$ K (see Fig. 1).

4.4. *Predicted Column Densities for* H_2

After fitting a correlation plot between two observed column densities (N_o), fit parameters may be used to predict one of the column densities (N_p) in the absence of the other. The value of $N_p(H_2) = (7.4–10.0) \times 10^{20}$ cm^{-2} toward HD 208266 was given in Pan et al. (2005) based on their fits of $N_o(CO)$ and $N_o(CH)$ versus $N_o(H_2)$ for the small sample of sight lines toward Cep OB2. Here we use the dual-slope relationship between CO and H_2 in Figure 6*a*, as well as the single-slope relationship between CH and H_2 in Figure 8, to predict (the unobserved) $N(H_2)$ toward the two stars without H_2 data but with CO and CH data, HD 36841 and HD 43818/11 Gem, which are near the CO versus H_2 break in slope, as well as toward HD 208266. These predictions employ the global ±20% 1 σ uncertainties in N_o values.

The CO-based $\log N_p(H_2)$ values for HD 36841 and HD 43818 are 20.46 ± 0.06 and 20.32 ± 0.06, respectively. The same exercise for HD 208266 yields $\log N_p(H_2) = 21.12 \pm 0.03$, which is 2 σ away from the predicted range (20.87–21.00) given in Pan et al. (2005). The CH-based $\log N_p(H_2)$ values for HD 36841 and HD 43818 are 20.41 ± 0.08 and 20.45 ± 0.08, respectively, which are 0.05 lower and 0.13 higher than the CO-based $\log N_p(H_2)$. Conceivably, when the difference is larger than 20% (or >0.08 in the log), it is reflecting the additional uncertainties introduced by the intrinsic widths of the correlations. The same exercise for HD 208266 yields $\log N_p(H_2) = 20.95 \pm 0.08$, which is 0.17 lower than the CO-based prediction but in excellent agreement with the predicted midrange value given in Pan et al. (2005). Combining results from CO and CH, both HD 36841 and HD 43818 are predicted here to have $\log N_p(H_2) = 20.4 \pm 0.1$, while for HD 208266 the prediction is 21.0 ± 0.1. The corresponding 3 σ uncertainties are provided by the full width (±0.3) of the horizontal spread of $N_o(H_2)$ in both Figures 6 and 8.

5. ANALYTICAL CHEMISTRY

We examined the results presented here from two chemical perspectives. First, two sets of analytical expressions from previous work are used in this section to extract n_H associated with the material containing CO; one set involves the equilibrium chemistry leading to CN, and another set describes the (equilibrium) synthesis of CH from CH^+. In § 6 we provide a more general chemical analysis based on the use of the Cloudy code.

5.1. CN *Chemistry*

Analytical expressions for the chemistry connecting CH, C_2, and CN in diffuse interstellar clouds (Federman et al. 1994), with updated rate coefficients (Knauth et al. 2001; Pan et al. 2001), are used to extract estimates for gas density, $n_H(CN)$. To summarize, the production of CN is primarily given by the reactions C_2(N, C)CN, CH(N, H)CN, and the chain C^+(NH, H)CN^+(H_2, H)HCN^+(*e*, H)CN, which has a parallel path where HCN^+ reacts with H_2 to produce H_2CN^+ and then CN via electron recombination. *Observed* $N(CH)$ and $N(C_2)$ (when available) are adopted for the comparison between observed and predicted CN column densities. A steady state rate equation involving terms for chemical production and photodestruction of CN is employed in the determination of n_H (Federman et al. 1994).

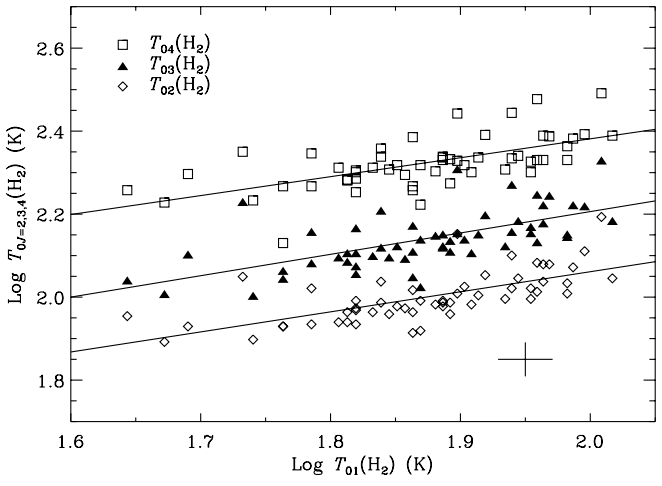

FIG. 14.—Three higher J excitation temperatures of H_2 plotted vs. T_{ex} of the $J = 1$ level, showing three indistinguishable positive correlations with $\langle B \rangle = 0.48 \pm 0.08$. The adopted global uncertainties are ±5% and ±10% in T_{01} and T_{0J} ($J > 1$), respectively.

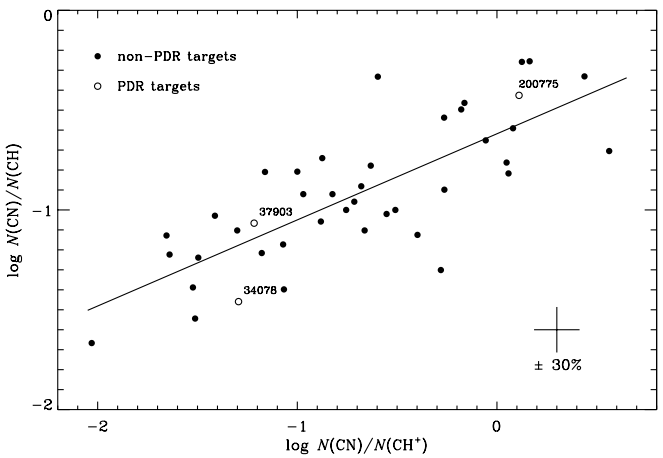

FIG. 15.—Plot showing the empirical density indicator, CN/CH, to be well correlated with CN/CH^+, so that gas density is increasing with either quantity. The relationship has a slope of 0.43 ± 0.06 and $r = 0.77$.

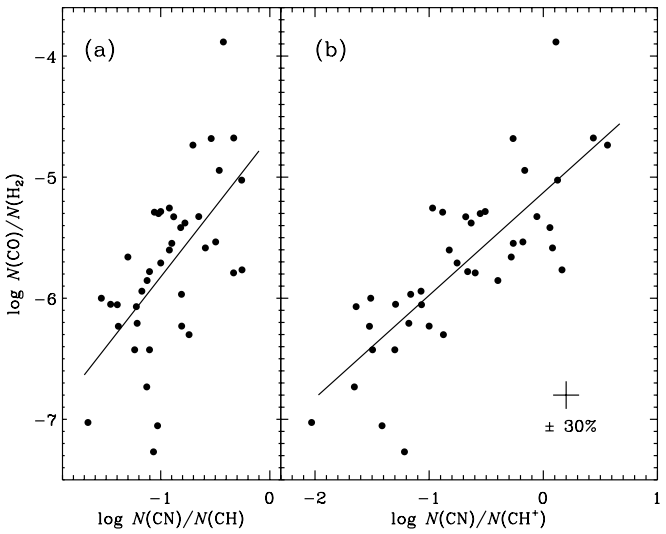

FIG. 16.—Abundance of CO relative to H_2 plotted vs. two empirical indicators of gas density: (*a*) CN/CH and (*b*) CN/CH^+. The sample of CO/H_2 data points shows a tighter correlation with CN/CH^+ ($r = 0.784$) than with CN/CH ($r = 0.604$).

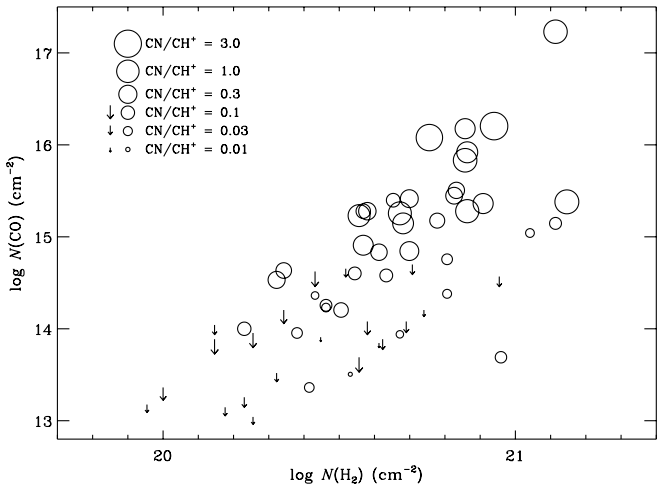

FIG. 17.—Values of $N(CN)/N(CH^+)$ are denoted by circles (or by upper limit arrows) as indicators of n_H. The general indication is that higher gas density is associated with higher $N(CO)$ along the upper envelope of the distribution, as well as with higher $N(H_2)$ (from left to right along the diagonal).

As in our recent papers (e.g., Gredel et al. 2002; Pan et al. 2005; Welty et al. 2006), results are presented for individual velocity components, whenever possible. Like Gredel et al. (2002), we determine upper limits on $n_H(CN)$ for components without detectable amounts of CN absorption. This is especially important for the results presented here because many new detections of CO are found in directions that are not very rich in molecules. We do not repeat the chemical analysis for sight lines in Ophiuchus, Cep OB2, and Cep OB3 described in Pan et al. (2005) or the analyses of the PDRs illuminated by HD 37903 and HD 200775 found in Knauth et al. (2001). Similarly, many of the directions contained in a reanalysis of spectra acquired with the *Copernicus* satellite (Crenny & Federman 2004) are discussed in Zsargó & Federman (2003). Updates are given for some of the sight lines examined by Federman et al. (1994) and Wannier et al. (1999) in order to provide a self-consistent analysis, and comparisons are presented below.

A key ingredient in this analysis is the value for the amount of extinction at UV wavelengths caused by interstellar grains, τ_{UV}, for each sight line. This was determined by examining various measures for grain properties: the ratio of total to selective extinction (Cardelli & Clayton 1991; Larson et al. 2000; Barbaro et al. 2001; Patriarchi et al. 2001, 2003; Whittet et al. 2001; Ducati et al. 2003; Valencic et al. 2004; Fitzpatrick & Massa 2005; Larson & Whittet 2005; Sofia et al. 2005), the shape of the UV extinction curve (Massa et al. 1983; Witt et al. 1984; Fitzpatrick & Massa 1990; Papaj et al. 1991; Welty & Fowler 1992; Larson et al. 1996; Patriarchi & Perinotto 1999), and a comparison of the ratio $E(15 - V)/E(B - V)$ (Krelowski & Strobel 1983; Savage et al. 1985; Papaj & Krelowski 1992). For most sight lines, typical grain properties apply, and we adopted $\tau_{UV} = 2 \times 3.1E(B - V)$, where 2 is a prefactor that depends on characteristics of the extinction curve (Federman et al. 1994) and the amount of reddening came from the work cited above or from Seab & Snow (1984), Carnochan (1986), and Aiello et al. (1988). When grain properties suggested enhanced UV extinction, we used prefactors of 3 (for the directions toward HD 12323, HD 15137, HD 36841, HD 163758, HD 185418, HD 198781, and HD 210121) or 2.5 (for HD 14434) instead of 2, depending on the severity of the difference from typical values. Several directions (HD 96675, HD 99872, HD 102065, and HD 124314) indicated below typical UV extinction; here the prefactor was set to 1.7. For HD 93840, an intermediate value seems to be appropriate, and a prefactor of 1.85 was adopted. For sight lines without information on grain properties (HD 24190, HD 30122, HD 137595, HD 190918, HD 192035, and HD 192369), the typical relation was employed. One further constraint was considered: components having separations less than 20 km s^{-1} were assumed to arise from nearby complexes where shadowing would be present and each component would experience the full amount of extinction as a result. The lone exception was the direction toward HD 13745, where the components are 26 km s^{-1} apart. The results for HD 30122 given in Table 7 show the effects that uncertainties in τ_{UV} have on $n_H(CN)$. In general, photodissociation is the dominant destruction pathway for the clouds in our study; therefore, uncertainties in τ_{UV} lead to inferred uncertainties of $\sim$30% in $n_H(CN)$.

For many of the directions, *N* data for CH, CN, and CH^+ used in the next section were obtained as part of the present study. Much of the remaining data on $N(CH)$ and $N(CN)$ come from the compilation of Federman et al. (1994), but there are a number of updates now available. For ξ Per, we included the results of Crane et al. (1995) for CH and of Lambert et al. (1995) for C_2. The results of Lambert et al. (1995) for ζ Oph were also used here. We adopted the results of Kaczmarczyk (2000) for the C_2 column toward X Per. The CH results of Andersson et al. (2002) for HD 99872, HD 115455, and HD 137595 are included, as are the CH and CH^+ results of Gredel (1997) for HD 114886. For the sight line toward HD 154368 we incorporated $N(CH)$ from D. E. Welty (2005, private communication) and $N(CN)$ from Roth et al. (1993) and Roth & Meyer (1995). For the gas toward HD 185418 and HD 192639, we used the results from Sonnentrucker et al. (2002, 2003) supplemented by those of Thorburn et al. (2003). Since Pan et al. (2005) did not consider directions without detectable amounts of CN in their analyses, we do so here for HD 208440, HD 208905, HD 209339, 19 Cep, and HD 217035A. For stars in Per OB2 (40 Per, HD 23478, and HD 24190) we used our unpublished results. We also note that for gas toward o Per, X Per, and 62 Tau, component structure is available for CN, but not C_2. Since these species appear to coexist (e.g., Federman et al. 1994), we scaled the C_2 results so that CN/C_2 was the same for each component. Finally, as indicated in

TABLE 7

CHEMICAL RESULTS FROM CN CHEMISTRY

Star	Cloud[a]	N_o(CH) (10^{12} cm^{-2})	N_o(C_2) (10^{12} cm^{-2})	N_p(C_2) (10^{12} cm^{-2})	N_o(CN) (10^{12} cm^{-2})	N_p(CN) (10^{12} cm^{-2})	T (K)	τ_{UV}	n_H(CN) (cm^{-3})
BD +48 3437	...	4.80	...	4.5	0.58	0.58	65	2.17	475
BD +53 2820	+0.9	1.59	...	≤3.9	≤0.93	≤0.93	65	2.17	≤1600
	+6.9	2.49	...	≤5.6	≤0.93	≤0.93	...	...	≤1425
HD 12323	−13.5	1.77	...	4.1	0.89	0.72	65	2.23	∼1600
	−9.7	3.36	...	6.3	1.03	1.03	...	...	1200
HD 13268	−16.4	1.20	...	≤2.1	≤0.42	≤0.42	65	2.48	≤1450
	−10.4	2.70	...	3.5	0.61	0.60	...	...	900
	−7.4	5.42	...	7.5	1.33	1.35	...	...	1000
	−1.0	1.82	...	≤2.4	≤0.42	≤0.42	...	...	≤925
HD 13745	−43.9	5.89	...	6.5	0.74	0.74	65	1.34	850
	−18.1	3.98	...	≤4.9	≤0.57	≤0.56	...	...	≤950
HD 14434	...	9.32	...	2.7	0.55	0.58	65	3.72	125
HD 15137	−13.4	2.24	...	≤2.0	≤0.42	≤0.41	65	2.98	≤425
	−7.4	1.62	...	≤1.8	≤0.42	≤0.42	...	...	≤900
	−0.2	2.56	...	≤2.1	≤0.42	≤0.42	...	...	≤550
HD 22951/40 Per	...	12.0	3.6	4.4	0.64	0.42	40	1.49	225
HD 23180/o Per	+4.6	7.01	≤4.0	≤3.3	≤0.30	≤0.32	40	1.86	≤200
	+7.3	11.96	23.0	16.0	1.65	1.91	...	...	625
HD 23478	+4.1	13.53	7.8	8.4	1.03	0.85	50	1.67	325
	+7.7	4.72	6.2	6.6	0.80	0.74	...	...	775
HD 24190[b]	...	9.5	...	7.3	0.75	0.73	40	1.74	375
HD 24398/ζ Per	...	22.0	35.0	35.0	3.9	3.9	30	2.05	700
HD 24534/X Per	+5.0	6.0	3.4	3.5	0.70	0.62	20	3.84	250
	+7.1	25.9	31.0	31.0	6.6	6.7	...	...	650
HD 24912/ξ Per[b]	...	12.0	7.9	4.6	0.26	0.49	70	1.44	∼250
HD 27778/62 Tau	+5.0	12.8	24.0	36.0	8.9	5.8	50	2.29	∼1100
	+7.2	9.4	14.0	30.0	5.1	3.6	...	...	∼575
HD 30122	...	15.72	...	10.5	1.58	1.54	65	2.48	400
	...	15.72	...	6.6	1.58	1.53	...	3.72	200
	...	15.72	...	13.5	1.58	1.62	...	2.11	400
HD 36841	...	9.92	...	7.2	1.56	1.54	65	3.16	475
HD 37367	+3.8	3.23	...	≤2.3	≤0.34	≤0.34	65	2.48	≤425
	+6.2	9.76	...	≤2.7	≤0.34	≤0.35	...	...	≤150
HD 43818/11 Gem	−7.0	3.80	...	≤2.6	≤0.61	≤0.61	65	3.41	≤425
	−3.9	2.69	...	≤2.4	≤0.61	≤0.61	...	...	≤625
	+1.2	2.79	...	≤2.4	≤0.61	≤0.61	...	...	≤600
	+5.2	2.02	...	≤2.2	≤0.61	≤0.61	...	...	≤900
HD 58510	...	5.11	...	≤4.6	≤0.51	≤0.50	65	1.92	≤375
HD 63005	+14.3	4.64	...	10.5	1.40	1.41	65	1.74	1300
	+21.0	4.37	...	≤8.1	≤1.03	≤1.03	...	...	≤1025
HD 96675	...	22.76	...	49.7	6.26	6.25	50	1.58	1425
HD 99872	...	12.6	...	≤6.1	≤0.62	≤0.63	65	1.90	≤200
HD 102065	+1.0	1.1	...	≤1.4	≤0.62	≤0.17	65	0.90	>1600
	+3.8	6.0	...	≤7.9	≤0.94	≤0.93	...	...	≤1600
HD 115455	...	17.0	...	≤8.1	≤1.6	≤1.6	65	3.16	≤275
HD 137595	...	12.2	...	≤7.7	≤0.80	≤0.82	65	1.49	≤400
HD 148184/χ Oph	...	34.0	35.0	19.0	1.3	2.7	60	2.30	∼300
HD 149757/ζ Oph[b]	...	25.0	18.0	21.0	2.6	2.2	60	1.98	325
HD 154368	−13.1	2.1	...	0.53	0.21	0.20	50	4.77	90
	+3.3	54.1	51.0	58.0	27.0	22.0	...	...	750
HD 157857	+0.0	5.02	...	≤6.0	≤1.15	≤1.16	65	2.67	≤900
	+4.2	2.83	...	≤4.9	≤1.15	≤1.10	...	...	≤1600
HD 185418[b]	...	13.0	≤10.0	≤1.5	≤0.50	≤0.48	65	4.46	≤30
HD 190918	+2.1	1.73	...	≤1.9	≤0.34	≤0.34	65	2.54	≤775
	+18.3	1.16	...	≤1.8	≤0.34	≤0.34	...	...	≤1175
HD 192035	+1.4	3.31	...	≤4.3	≤0.53	≤0.53	65	2.05	≤575
	+5.6	11.42	...	33.4	5.07	5.11	...	...	1550
	+9.4	2.62	...	≤4.1	≤0.53	≤0.53	...	...	≤725
HD 192639[b]	...	28.0	≤10.0	≤3.2	≤0.70	≤0.76	65	3.97	≤40
HD 198781	...	13.19	...	13.1	3.29	3.25	65	3.26	750
HD 208440[b]	...	11.7	...	≤8.2	≤0.90	≤0.87	65	1.80	≤325
HD 208905[b]	...	5.4	...	≤7.6	≤0.90	≤0.90	65	1.60	≤850
HD 209399[b]	...	7.9	...	≤8.1	≤0.90	≤0.91	65	1.28	≤825
HD 209975/19 Cep[b]	...	8.5	...	≤8.1	≤0.90	≤0.90	65	1.52	≤600

TABLE 7—*Continued*

Star	Cloud[a]	N_o(CH) (10^{12} cm^{-2})	N_o(C_2) (10^{12} cm^{-2})	N_p(C_2) (10^{12} cm^{-2})	N_o(CN) (10^{12} cm^{-2})	N_p(CN) (10^{12} cm^{-2})	T (K)	τ_{UV}	n_H(CN) (cm^{-3})
HD 210121	...	286.2	65.0	55.1	17.35	19.10	50	3.35	1425
HD 210809	−0.6	1.61	...	≤4.4	≤0.64	≤0.64	65	1.98	≤1325
	+3.4	3.86	...	≤5.4	≤0.64	≤0.64	...	...	≤575
HD 217035A[b]	...	16.8	...	≤9.0	≤0.90	≤0.90	65	2.47	≤125
HD 220057	−1.8	9.33	...	11.8	1.36	1.37	65	1.61	750
	+1.9	3.86	...	≤5.4	≤0.65	≤0.65	...	...	≤850

NOTE.—All calculations employ $I_{UV} = 1$, except for HD 27778/62 Tau and HD 210121, where $I_{UV} = 0.5$.

[a] If more than one cloud containing CN appears along a line of sight, they are designated by v_{LSR} values from Table 3, having identical values for T and τ_{UV}.

[b] Results are for line of sight because some input data are not available for all components.

the table, line-of-sight results are given for directions where component information is missing for C_2 as well as CN.

The results of this analysis appear in Table 7. For each cloud in a specific direction, we list the observed values N_o(CH), N_o(C_2), and N_o(CN) and the predicted values N_p(C_2) and N_p(CN) that best match the observations, the kinetic temperature (T), τ_{UV}, and n_H(CN). N-values are given in units of 10^{12} cm^{-2}. Most calculations are based on I_{UV} equaling 1 and on $T = 65$ K. The latter value is not critical because the results for n_H are not very sensitive to T. For especially molecule-rich clouds and for some clouds studied by us in the past, lower values for T are adopted. The N_p values are generally in very good agreement, and are always within a factor of 2, of the N_o values.

5.2. CH^+ *Chemistry*

For many of the directions listed in Table 7, only upper limits on CN are available. For nearly all of these, CO production via reactions involving CH^+ appears likely (see below). We therefore considered estimating the gas density from the chemical scheme linking CH and CH^+ (Welty et al. 2006; Ritchey et al. 2006) as follows: $CH^+(H_2, H)CH_2^+(H_2, H)CH_3^+$ and the dissociative recombination $CH_3^+(e, H_2)CH$. In particular, we used the analytical expression in Ritchey et al. (2006),

$$n_H = \frac{N(CH)}{N(CH^+)} \frac{2I_{UV}\Gamma(CH)}{0.67kf(H_2)},$$

where Γ(CH) is the CH photodissociation rate [$1.3 \times 10^{-9} \exp(-\tau_{UV})$ s^{-1}], k is the rate coefficient for the reaction $CH^+(H_2, H)CH_2^+$ (1.2×10^{-9} cm^3 s^{-1}), and $f(H_2)$ is the molecular fraction. In addition to the present study, $N(H_2)$ values come from Savage et al. (1977), Rachford et al. (2002), and Pan et al. (2005). The column densities of atomic hydrogen, N(H I), are from Savage et al. (1977) for the bright stars and from Rachford et al. (2002), Andre et al. (2003), Cartledge et al. (2004), and Jensen & Snow (2007) for sight lines studied with *FUSE*. Data on atomic hydrogen do not exist for the sight lines toward HD 114886 and HD 137595. For these stars, we estimated N(H I) from $E(B - V)$ using the relationship between reddening and total proton column density of Bohlin et al. (1978) and accounting for the amount of H_2. Values of N for the carbon-bearing molecules are taken from the sources given in the previous section for the most part or from those compiled by Crenny & Federman (2004) for the bright stars. The results appear in Table 8.

5.3. *Comparison of Results*

Many of the sight lines listed in Table 7 were analyzed in our previous work. For o Per, X Per, and 62 Tau, we incorporated results for individual velocity components by scaling the values for N(C_2) to those measured for N(CN). The updated chemistry does not significantly affect the conclusions of Federman et al. (1994) for the three sight lines, nor for the gas toward ζ Per, ξ Per, χ Oph, and ζ Oph. There is also reasonable correspondence between the present chemical results for 40 Per and those of Wannier et al. (1999), which are based on C_2 (and C I) excitation. Finally, our inferred density for the main component toward HD 154368 is about a factor of 2 larger than our previous estimate (Federman & Lambert 1988), which was based on an earlier, higher measure for N(CH). This refined value for n_H(CN) is consistent with the results of van Dishoeck & de Zeeuw (1984) from C_2 excitation (300–1000 cm^{-3}) and Black & van Dishoeck (1991) from CN excitation (750–2000 cm^{-3}).

Comparisons for several other sight lines with other work are also available. The most well studied of these directions is toward HD 210121. Our chemical analysis indicates that $n_H = 1425$ cm^{-3}, one of the highest values in Table 7. The large value agrees with results from analyses of molecular excitation. For C_2 and CN, Gredel et al. (1992) found densities of 500–1000 cm^{-3} and 1500–2500 cm^{-3}, respectively, while Roueff et al. (2002) obtained densities of about 2000 cm^{-3} from the distribution of C_3 levels. Our upper limits on density for the gas toward HD 185418 and HD 192639 (≤30–40 cm^{-3}) are consistent with densities inferred from C I excitation (Sonnentrucker et al. 2002, 2003).

For most directions with CN upper limits, results from CN chemistry are not very constraining (e.g., Federman et al. 1997b). Instead, comparisons with C I excitation seem to be more appropriate, as in the cases of HD 185418 and HD 192639. For such directions, CH^+ chemistry usually dominates, and so the results from Table 8 would be more meaningful. For the nearby bright stars, α Cam, ν Sco, and μ Nor, a comparison with the results from Jenkins et al. (1983) is possible. For the three directions, densities are derived from the quoted pressures assuming that T_{01} is the kinetic temperature. Consistency between results occurs for α Cam and μ Nor, where upper limits from C I excitation are 10 and 370 cm^{-3}, respectively, versus our values of about 1 for no enhancement in the strength of the UV radiation field. However, the *lower* limit toward ν Sco of 70 cm^{-3} contrasts with our density of 10 cm^{-3}. If the cloud were near the star, such that I_{UV} was greater than 1, the two measures could be brought into agreement. This points out a deficiency in the current analysis of CH^+-like CH (Lambert et al. 1990) for many of the sight lines in Table 8: most stars in the table lie at least a kiloparsec away. Thus, a significant amount of atomic hydrogen and a corresponding amount of UV extinction are not likely associated with the gas containing CH and CH^+. The most important factor is the exponential change in extinction, thereby increasing the

TABLE 8
CHEMICAL RESULTS FROM CH^+ CHEMISTRY

Star[a]	$N(CH^+)$ (10^{12} cm^{-2})	$N(CH)$ (10^{12} cm^{-2})	$f(H_2)$	τ_{UV}	$n_H(CH^+)$ (cm^{-3})
BD +53 2820	6.40	4.08	0.11	2.17	2.1
CPD −69 1743	15.0	2.20	0.13	1.30	1.0
CPD −59 2603	16.0	12.0	0.09	2.42	2.4
HD 15137	14.0	6.42	0.24	2.98	0.3
HD 30614/α Cam	20.0	6.80	0.36	1.98	0.4
HD 37367	32.0	13.0	0.30	2.48	0.4
HD 58510	12.0	5.11	0.15	1.92	1.4
HD 93840	3.30	1.80	0.03	0.52	31.4
HD 99872	23.0	12.6	0.28	1.90	1.0
HD 102065	11.0	7.10	0.68	0.90	1.3
HD 114886	19.0	9.00	0.19	2.48	0.7
HD 115455	17.0	17.0	0.23	3.16	0.6
HD 116852	3.50	1.70	0.13	1.36	3.1
HD 122879	12.0	3.10	0.20	2.17	0.5
HD 124314 (−19)	8.60	1.80	0.33	1.37	0.5
HD 124314 (+2)	6.20	7.10	0.22	1.37	4.2
HD 137595	18.0	12.0	0.60	1.49	0.8
HD 145502/ν Sco	6.30	5.90	0.10	1.17	9.4
HD 149038/μ Nor	35.0	10.0	0.36	2.36	0.2
HD 152590	19.0	10.0	0.22	2.67	0.5
HD 152723	11.0	6.40	0.13	2.60	1.1
HD 157857	20.0	7.85	0.33	2.67	0.3
HD 163758	1.40	2.20	0.08	3.07	3.4
HD 164353/67 Oph	7.40	4.50	0.26	0.74	3.5
HD 185418	12.0	13.0	0.40	4.46	0.1
HD 190918	14.0	2.89	0.07	2.54	0.8
HD 192639	41.0	28.0	0.34	3.97	0.1
HD 203532	3.00	25.0	0.34	1.92	11.5
HD 208440	8.70	11.7	0.21	1.80	3.5
HD 209339	6.60	7.90	0.17	1.28	6.5
HD 209975/19 Cep	24.0	8.50	0.17	1.52	1.5
HD 210809	7.50	5.47	0.10	1.98	3.2
HD 217035A	21.0	16.8	0.38	2.47	0.6
HD 218376/1 Cas	11.0	7.60	0.24	1.36	2.4

[a] If more than one cloud containing CN appears along a line of sight, the velocity is given in parentheses.

estimate for n_H. The typical increase is about a factor of 10 but can be significantly more. For the clouds toward HD 185418 and HD 192639, densities approaching 10 are possible, comparable to the results from C I (Sonnentrucker et al. 2002, 2003). Overall, the analytical results presented in Tables 7 and 8 are consistent with the detailed models described next. In particular, the gas rich in CN and CO tends to have larger densities.

5.4. *The Role of* C_2 *Data*

Solving for $n_H(CN)$ via the analytical chemistry scheme depends on input of $N(CH)$ and $N(CN)$, but not necessarily on the availability of $N(C_2)$. When $N(C_2)$ is not available, it is predicted by the model via $CH(C^+, H)C_2^+$, which is followed by $C_2^+(H_2, H)C_2H^+$ and $C_2H^+(H_2, H)C_2H_2^+$, both leading to the C_2 molecule by dissociative recombination. The predicted value of $N(C_2)$ is then determined from a steady state rate equation involving terms for C_2 chemical production and photodestruction. However, when $N(C_2)$ is known, it introduces a constraint on the chemical formation of C_2, which in turn is affecting the production (and predicted abundance) of CN. It would be interesting to investigate the differences, if any, between sight lines with or without observed values of $N(C_2)$.

Figure 18*a* shows a logarithmic plot of CN-derived gas densities, $n_H(CN)$, versus observed $N(CN)$ for sight lines with detected CN components, fitted with $B = 0.31 \pm 0.10$ (*solid line*). (Data were gathered from the chemical analyses of this paper, of Knauth et al. [2001], and of Pan et al. [2005].) Whereas sight lines without observed values of $N(C_2)$ (*open circles*) show a loose correlation with $r = 0.32$ between $n_H(CN)$ and $N(CN)$, a much tighter correlation with $r = 0.61$ is seen in the distribution of the filled circles, which denote sight lines with C_2 measurements. Thus, it is apparent that more robust derivations of $n_H(CN)$ require not only observed $N(CH)$ and $N(CN)$ values but also observed $N(C_2)$ data. Similarly, Figure 18*b* shows the run of $n_H(CN)$ versus the ratio CN/CH^+, which is the better empirical proxy for gas density (§ 4.3). Again it is obvious that sight lines with observed $N(C_2)$ show a tighter correlation than those without C_2 data.

Finally, as a confirmation of the close affinity between resultant gas densities and input C_2 observations, we plot in Figure 19*a* these two quantities. It shows that $n_H(CN)$ predictions correlate well with $N(C_2)$ for sight lines with C_2 detections ($r = 0.63$, CL $> 99.5\%$). This relationship, with $B = 0.48 \pm 0.15$, is in line with the expectation that CN and C_2 molecules are formed in higher density (and colder) clumps of gas because of the correlation found above between $n_H(CN)$ and $N(CN)$. Figure 19*b* indeed shows that the correspondence between the observables $N(CN)$ and $N(C_2)$ has a slope of 0.97 ± 0.28 and $r = 0.64$, or CL $\geq 99.7\%$. This result agrees at the 2 σ level with the slope of 1.6 ± 0.2 found by Federman et al. (1994) from

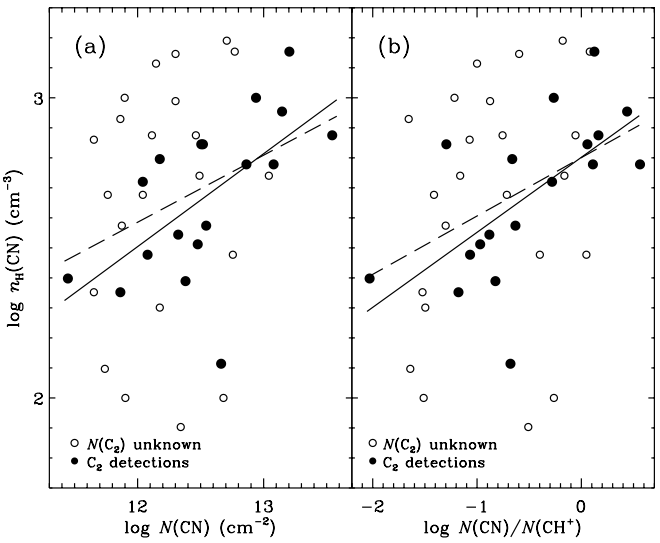

FIG. 18.—(*a*) Density from the CN chemical analysis vs. N(CN). All sight lines are fitted by $B = 0.22 \pm 0.11$ (*dashed line*), whereas those with known $N(C_2)$ (*filled circles*) have $B = 0.31 \pm 0.10$ (*solid line*). The latter has an appreciably smaller dispersion, with $r = 0.61$ instead of 0.32 (CL increases from 95% to 99%). Panel (*b*) employs the same symbols as panel (*a*). It shows n_H vs. N(CN)/N(CH$^+$), where B increases from 0.19 ± 0.08 to 0.25 ± 0.08, r from 0.36 to 0.64, and CL from 98% to 99.5% owing to restricting the sample to those sight lines with known $N(C_2)$. Thus, the restricted sample yields more robust predictions of n_H values.

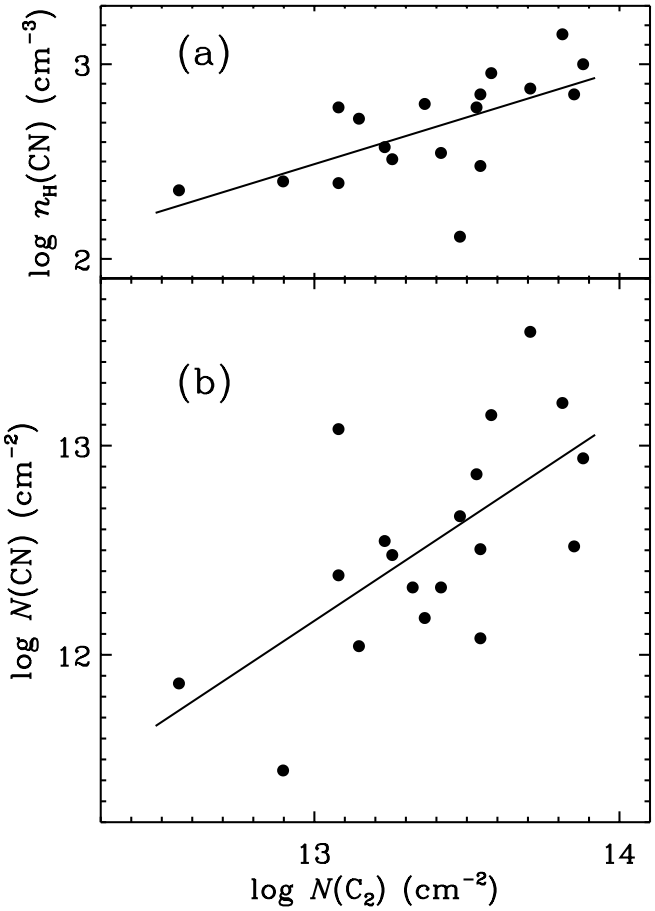

FIG. 19.—Values of n_H(CN) from the chemical analysis are seen in (*a*) to be well correlated with $N(C_2)$ values. The slope is $B = 0.48 \pm 0.15$ and $r = 0.63$. In (*b*) CN is shown to be linearly related to C_2, since the slope of their abundance relationship is 0.97 ± 0.28 ($r = 0.64$).

a larger 33-point sample that showed a tighter correlation ($r = 0.85$ and CL $> 99.99\%$). Gredel (2004) showed that a small sample of sight lines toward Cep OB4 is probing a high-n_H molecular cloud and providing tight correlations between all three molecules that are involved in equilibrium chemistry: CH, C_2, and CN. It is clear that CN chemistry is dependent on $N(C_2)$ and that robust n_H(CN) values can be derived from these two observables.

6. NUMERICAL MODELS WITH CLOUDY

6.1. *Computational Details*

We performed a series of model calculations designed to cover a range of physical parameters characteristic of diffuse and molecular clouds. Our calculations used version C07.02 of the spectral synthesis code Cloudy, last described by Ferland et al. (1998). Van Hoof et al. (2004), Abel et al. (2005), Shaw et al. (2005), and Röllig et al. (2007) discuss in detail the Cloudy treatment of various physical processes important in modeling atomic and molecular phases of the ISM. Röllig et al. (2007) compare the predictions made by various PDR codes and find excellent agreement between Cloudy and the codes used in Kaufman et al. (1999), Boger & Sternberg (2005), and the Meudon PDR code (Le Petit et al. 2006).

The geometry of our model is a plane-parallel slab illuminated from both sides by far-UV radiation. This geometry is appropriate for diffuse environments bathed on all sides by the far-UV radiation field and is identical to that used in both van Dishoeck & Black (1988) and Le Petit et al. (2006). Le Petit et al. (2006) showed that N_p values for species like CO and CH in a single- versus double-sided calculation vary by up to a factor of 2 for an A_V between 0.2 and 5 mag.

Our choice of explored ranges in physical parameters such as density, radiation field intensity, cosmic-ray ionization rate, and stopping criterion (the physical thickness of our slab model) is determined by the need to compare our results with observations and with results from previous studies, and by typical diffuse cloud conditions. Diffuse clouds generally have n_H ranging from 10 to 5000 cm^{-3} (Snow & McCall 2006); therefore, we vary n_H from 10 to 1000 cm^{-3}, in increments of 1 dex. For simplicity, all calculations are performed at constant (depth independent) density. We use the Draine (1978) radiation field in our calculations, which is also used in van Dishoeck & Black (1988) and Le Petit et al. (2006). We vary the far-UV intensity from $I_{UV} = 0.1$ to 10 times the average value of the interstellar radiation field, which equals 1.6×10^{-3} ergs cm^{-2} s^{-1} (Habing 1968), also in increments of 1 dex. We also include the effect of cosmic rays, for which we use a cosmic-ray ionization rate $\zeta = 3 \times 10^{-17}$ cm^3 s^{-1}. Higher values of ζ were found by McCall et al. (2003) and Shaw et al. (2006), studying H_3^+ toward ζ Per and HD 185418, respectively; by Liszt (2003), who inferred a higher ζ based on analysis of HD and H_3^+ along a sample of sight lines; and by Federman et al. (1996b), based on cosmic-ray-induced chemistry of OH toward o Per. Nevertheless, since our goal is to model global trends, we decided to use a value of ζ consistent with the average value of $\zeta = 2.5 \times 10^{-17}$ cm^3 s^{-1} determined by Williams et al. (1998). We stop all calculations once $N(H_2) = 2 \times 10^{21}$ cm^{-2}, a value high enough to include all the diffuse cloud observational data in our sample. This stopping criterion corresponds to A_V of 1–5 mag. We integrate molecular N for all $N(H_2)$ values up to the stopping criterion, thus including all the phases of ISM clouds as classified by Snow & McCall (2006).

The thermal balance and ionization balance are both computed self-consistently. The temperature is computed from energy

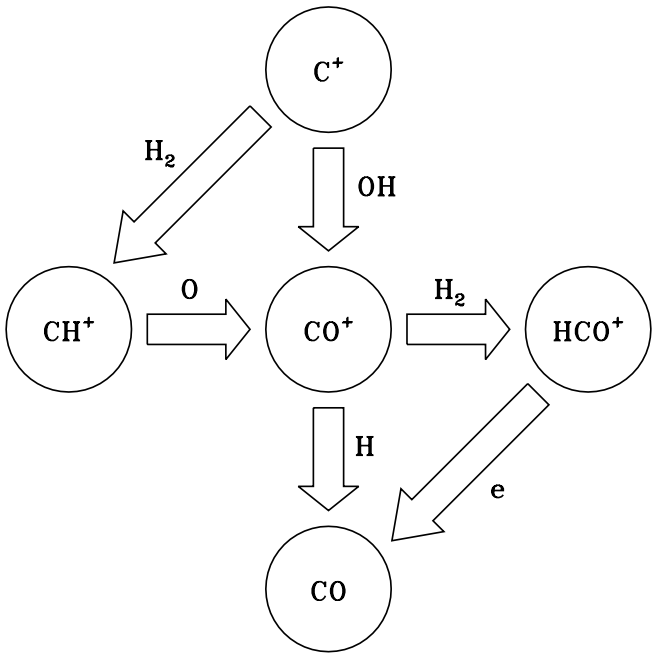

FIG. 20.—Schematic formation routes from C^+ to CO involving the most common intermediate gas-phase chemical reactants and products.

conservation consisting of a host of microphysical processes (Ferland et al. 1998; Abel et al. 2005; Röllig et al. 2007). All atomic photoprocesses are calculated by integrating the product of the incident radiation field intensity over the cross section for the photointeraction rate. We also integrate the cross section for photodissociation of H_2, using a detailed H_2 model incorporated into Cloudy (Shaw et al. 2005). For CO, we use the shielding function described in van Dishoeck & Black (1988) and Hollenbach et al. (1991). Le Petit et al. (2006) show that the predicted N(CO) is about a factor of 2 smaller when using a shielding function versus an exact treatment of CO photodissociation in diffuse clouds. This is small, however, when compared to the increases by a factor of 100 that nonequilibrium CH^+ formation can contribute to the formation of CO in diffuse environments (Zsargó & Federman 2003; this work).

Our assumed gas and dust abundances are consistent with average ISM values. For the gas phase, we include the 30 lightest elements. The abundance relative to hydrogen for each species is an average of the abundance taken from Cowie & Songaila (1986) and ζ Oph (Savage & Sembach 1996). The only exceptions are C/H and O/H. For C/H we use the value determined by Savage & Sembach (1996) without averaging, while for O/H we use the value determined by Meyer et al. (1998). Some of the more important abundances by number are $He/H = 0.098$, $C/H = 1.3 \times 10^{-4}$, $O/H = 3.2 \times 10^{-4}$, $N/H = 8 \times 10^{-5}$, $Ne/H = 1.2 \times 10^{-4}$, $Si/H = 3.2 \times 10^{-5}$, $S/H = 3.2 \times 10^{-6}$, and $Cl/H = 1 \times 10^{-7}$.

Our network includes all known important chemical channels leading to CH^+ and CO formation (Fig. 20). The chemical reaction network consists of approximately 1200 reactions involving 89 molecules made up of H, He, C, N, O, Si, S, and Cl. A complete list of molecules and reactions, along with rates, can be found on the Cloudy Web site.[9] Most of the rate coefficients come from the UMIST database (Le Teuff et al. 2000; Woodall et al. 2007), although there are a few exceptions. For the important $C^+(OH, H)CO^+$ reaction, we use a temperature-dependent rate based on the data of Dubernet et al. (1992) with an equation derived in Abel et al. (2005). H_2 is known to form primarily through catalysis on grain surfaces, and we compute the rate of H_2 formation using the temperature- and material-dependent rates given in Cazaux & Tielens (2002).

The most important aspect to our calculations is the modeling of nonequilibrium chemistry in order to simulate the formation of CH^+ and its trickle-down effects on CO. To this end, we use the method given in Federman et al. (1996a) that incorporates a coupling between the ions and neutrals. The physical model for the nonequilibrium chemistry involves Alfvén waves that, on entering the cloud, dissipate over some physical scale, as described in § 6.2. We model this effect by reducing the coupling by one-third for $N(H_2) \geq 4 \times 10^{20}$ cm^{-2}. This roughly corresponds to the transition from the diffuse atomic to diffuse molecular phase (Snow & McCall 2006) and effectively "turns off" nonequilibrium effects for $N(H_2) \geq 4 \times 10^{20}$ cm^{-2}. The coupling in terms of $T_{\rm eff}$ depends most critically on $\Delta v_{\rm turb}$, which is the turbulent velocity of the gas. Therefore, we study the effects of $\Delta v_{\rm turb}$ on model predictions by using three different values for it, 2.0, 3.3, and 4.0 km s^{-1}. These values for $\Delta v_{\rm turb}$ are physically motivated from a number of considerations. A typical CH^+ line width is $\sim$2.5 km s^{-1} (Crawford et al. 1994; Crane et al. 1995; Crawford 1995; Pan et al. 2004). The character of $\Delta v_{\rm turb}$ in the nonequilibrium chemistry is 3D; therefore, if the CH^+ line width is completely described by a one-dimensional (1D) turbulence driven by Alfvén waves, $\Delta v_{\rm turb} = \sqrt{3}$(line width) $\sim$ 4.3 km s^{-1} (Heiles & Troland 2005). These authors found that a typical 1D value is $\Delta v_{\rm turb} \sim 1.2$–$1.3$ km s^{-1} in the cold neutral medium (CNM), corresponding to 2.1–2.3 km s^{-1} for 3D turbulence. The average of the CH^+ and CNM turbulence is $\sim$3.3 km s^{-1}. For all combinations of $n_{\rm H}$ and $I_{\rm UV}$ considered, we used this average value for $\Delta v_{\rm turb}$ (3.3 km s^{-1}) and only compute models with $\Delta v_{\rm turb} = 2.0$ or 4.0 km s^{-1} for $n_{\rm H} = 100$ cm^{-3} and $I_{\rm UV} = 1$. More details about the nonequilibrium CH^+ chemistry follow.

6.2. *Forming and Modeling* CH^+

Despite being one of the earliest molecules detected in the ISM, the formation of CH^+ in the diffuse ISM remains one of the biggest challenges in astrochemistry. The fundamental issue is that equilibrium chemical models underpredict $N(CH^+)$ by 3–4 orders of magnitude. The main problem in the formation of CH^+ is the primary formation channel leading to CH^+ in the reaction

$$C^+(H_2, H)CH^+. \quad (1)$$

This reaction is highly endothermic, with a rate of $1 \times 10^{-10} \exp(-4640/T_{\rm kin})$ cm^3 s^{-1} (Federman et al. 1996a). One way around the endothermicity of equation (1) is to have C^+ react with excited H_2 (H_2^*), which reduces or eliminates the exponential temperature dependence in the rate constant. As was mentioned in § 3.4, observations by Lambert & Danks (1986) provided correlations between $N(CH^+)$ and $N(H_2^*)$ for $J = 3$ and 5, but our sample of sight lines does not show any similar correlations, a fact that could be the result of our much narrower range of examined $N(H_2^*)$ values. In any case, models of CH^+ chemistry, which include the formation process via H_2^*, still do not reproduce the observed CH^+ in diffuse clouds (Garrod et al. 2003). CH^+ can also form through the radiative association of C^+ and H. The rate for this reaction is 1.7×10^{-17} cm^3 s^{-1}, which exceeds the rate for the reaction given by equation (1) for temperatures lower than 300 K. CH^+ is easily destroyed, however, through reactions with H and H_2. Therefore, the only way to efficiently

[9] See http://www.nublado.org.

produce CH^+ to observed levels is to increase the temperature above the value used in models of equilibrium chemistry.

It is generally agreed that nonequilibrium chemistry is the key to solving the CH^+ abundance problem in diffuse clouds. However, the exact physical mechanism producing CH^+ is still unclear. Hydrodynamic or magnetohydrodynamic shock models (Elitzur & Watson 1978; Draine & Katz 1986) generate large amounts of CH^+ by heating the gas to where CH^+ efficiently forms by equation (1). However, the lack of velocity differences between CH and CH^+ (Gredel et al. 1993; Federman et al. 1996a, 1997b) argues against shocks, while excitation analysis of interstellar C_2 (Gredel 1999) suggests that CH^+ production occurs in regions where the gas temperature is 50–100 K. Recently, Lesaffre et al. (2007) modeled the effects of turbulent diffusion on diffuse cloud chemistry, determining that this mechanism can increase the CH^+ abundance by up to an order of magnitude, which is still ~2 orders of magnitude lower than observed.

It has been suggested that CH^+ formation is driven by non-Maxwellian velocity distributions of H_2 and/or C^+ (Gredel et al. 1993). One possible solution to the problem of forming large quantities of CH^+ in cold ($T_{kin} < 100$ K) regions is discussed in Federman et al. (1996a). In this work, the authors propose that Alfvén waves entering a diffuse cloud from the intercloud medium are coupled to the cold gas through the Lorentz force (for ions) and collisions with the ions (for neutral atoms/molecules). The coupling results in significant nonthermal motion of the gas along the physical extent over which the MHD waves do not dissipate, consisting of a boundary layer on the cloud-intercloud surface. As a result, an effective temperature can be defined that characterizes the reaction between two species undergoing nonthermal motions (Flower et al. 1985; Federman et al. 1996a):

$$T_{\rm eff} = T_{\rm kin} + \frac{\mu}{3k}(\Delta v_{\rm turb})^2. \quad (2)$$

In this equation, k is the Boltzmann constant, μ is the reduced mass of the system, and $\Delta v_{\rm turb}$ is assumed to equal the Alfvén speed. For turbulent velocities consistent with the observed line widths of CH^+, $T_{\rm eff}$ is large enough to significantly increase the reaction rate of equation (1), increasing $N(CH^+)$ to values consistent with observation.

While this physical process is not the only possible explanation for the observed CH^+ abundance, this method does have several important characteristics. One is that it allows for the formation of CH^+ without heating the gas to temperatures inconsistent with the observed level of molecular excitation. This mechanism also explains the lack of OH toward ξ Per as a result of ion-neutral decoupling, where the magnetic field was coupled to the ions but not the neutrals. Thus, $T_{\rm eff}$ increased the reaction rate of ion-neutral reactions such as equation (1), but not neutral-neutral reactions such as O(H_2, H)OH, an important pathway to OH production at high temperatures. Finally, Alfvén wave propagation and dissipation in a cold diffuse cloud are a relatively simple way to model nonequilibrium effects in a calculation designed to model equilibrium chemistry. All one needs to do is compute $T_{\rm eff}$ for each reaction using equation (2) and replace T with $T_{\rm eff}$ when calculating the rate coefficient.

6.3. *Effects of* CH^+ *on Other Molecules*

The regions where CH^+ forms also contain significant quantities of other molecules. This conclusion is independent of the actual physical processes controlling CH^+ formation. Federman et al. (1997b) and Zsargó & Federman (2003) estimated the contribution to the formation of CH and CO due to equilibrium processes alone (i.e., due to regions that do not form CH^+) using a simple chemical model of a diffuse cloud. These studies found that most CH and CO (over 90% in many cases) could not be explained through equilibrium processes. The conclusion is that CH and CO in low-density ($n_{\rm H} \leq 100$ cm^{-3}) sight lines form in regions where nonequilibrium processes dominate the chemistry. So the same physical process that controls CH^+ formation is also likely to contribute to the formation of these molecules.

Almost all explanations to account for CH^+ involve increasing the temperature in order to activate the formation channel given by equation (1). However, increasing the temperature also increases the rates of other reactions, leading to increased formation of certain molecules. One example, OH, has already been mentioned. Forming CH^+ via equation (1) also leads to increased formation of CH through the chain involving CH_2^+ and CH_3^+, as was given in § 5.2. Forming CH^+ also leads to the formation of CO^+ via the reaction CH^+(O, H)CO^+, which is then followed by these two CO-forming channels: CO^+(H, H^+)CO and CO^+(H_2, H)HCO^+, together with HCO^+(e, H)CO. Finally, CO and CH are coupled through the neutral-neutral reaction CH(O, H)CO. This last reaction is an efficient formation route of CO and destruction route for CH at the high effective temperatures required for CH^+ formation. At higher density ($n_{\rm H} \geq 100$ cm^{-3}), C^+(OH, H)CO^+, followed by either CO^+-to-CO channel above, becomes the primary route for CO formation. Regardless of $n_{\rm H}$, photodissociation is the primary destruction process for CO.

Calculations made by van Dishoeck & Black (1988), Warin et al. (1996), and Le Petit et al. (2006) did not consider nonequilibrium effects. The models of van Dishoeck & Black (1988) and Le Petit et al. (2006) were used by Sonnentrucker et al. (2007) to show that, if $n_{\rm H}$ is sufficiently high, the correlation between CO and H_2 observed through UV absorption from *Copernicus*, *IUE*, *FUSE*, and *HST* can be reproduced (see also Fig. 7). However, since neither model considered CH^+ formation or nonequilibrium chemistry (although the Meudon PDR group did in the past take CH^+ into account through a shock model; see Le Petit et al. 2004), the CO relationship with H_2 is likely to be much different in a model that also reproduces trends in CH^+ versus H_2 and CH^+ versus CO. Such modeling and comparisons with observed trends in H_2, CO, and CH^+ abundances are the goals of our analysis.

6.4. *Comparing Model Results to Observation*

The results of our calculations are shown in Figures 21, 22, and 23. Each one shows plots of $N(CH^+)$ versus $N(H_2)$, $N(CH^+)$ versus N(CO), and N(CO) versus $N(H_2)$. Figure 21 shows the results for $I_{\rm UV} = 1$, $\log n_{\rm H} = 1$, 2, and 3 ($\Delta v_{\rm turb} = 3.3$ km s^{-1}); Figure 22 the results for $\log n_{\rm H} = 2$, $I_{\rm UV} = 0.1$, 1, and 10 ($\Delta v_{\rm turb} = 3.3$ km s^{-1}); and Figure 23 the results for $\log n_{\rm H} = 2$, $I_{\rm UV} = 1$, and $\Delta v_{\rm turb} = 2$, 3.3, and 4 km s^{-1}.

6.4.1. CH^+ *versus* H_2

The general observed trend in this plot is that $N(CH^+)$ appears to saturate around 2×10^{13} cm^{-2}, after which increasing $N(H_2)$ does not result in increased $N(CH^+)$ (recall Fig. 10). This trend is likely due to CH^+ formation by a mechanism that is acting over only a portion of the cloud. Our model mimics this effect by reducing $T_{\rm eff}$ for $N(H_2) \geq 4 \times 10^{20}$ cm^{-2}. Once $N(H_2)$ becomes greater than this limit, the combination of smaller $T_{\rm eff}$ (due to "turning off" the nonequilibrium chemistry) and increased destruction of CH^+ through reactions with H_2 leads to a decreased CH^+ density and hence a saturated $N(CH^+)$. Figures 21 and 22 show that for any value of $N(H_2)$ the value of $N(CH^+)$ is inversely

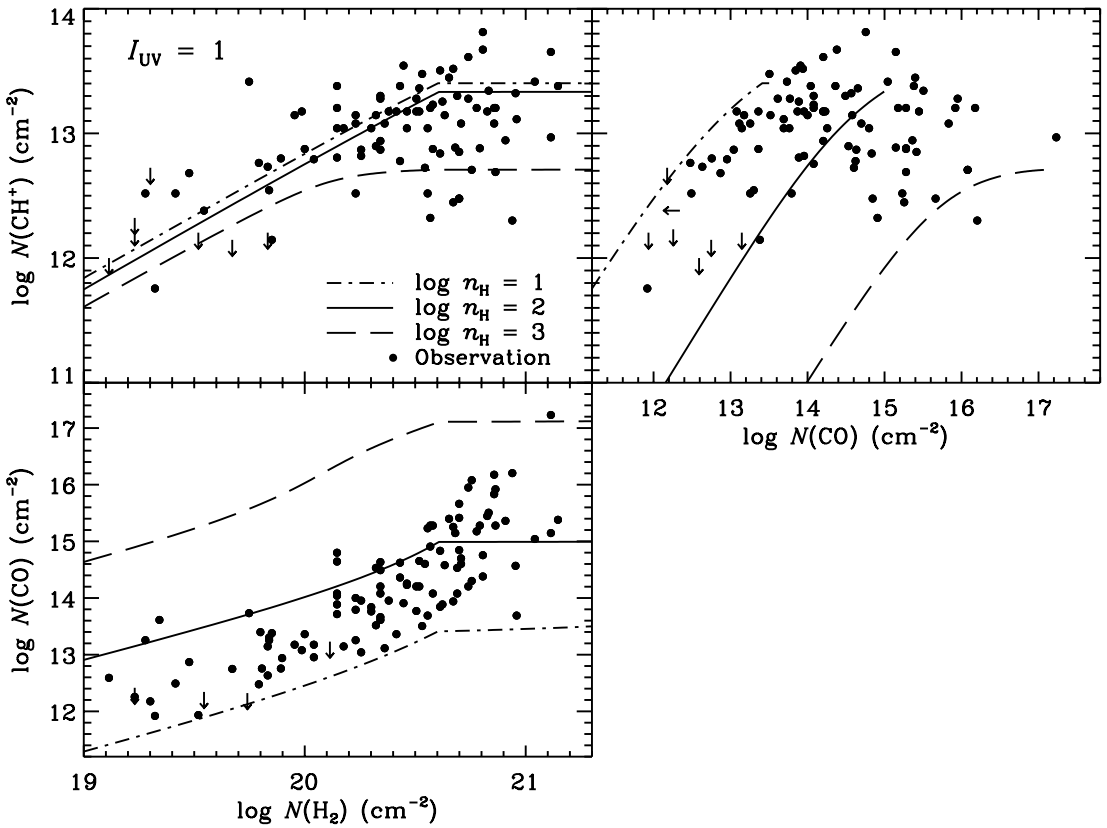

FIG. 21.—CH^+ vs. H_2, CH^+ vs. CO, and CO vs. H_2 as a function of n_H, for the average value of the far-UV interstellar radiation field ($I_{UV} = 1$) and $\Delta v_{turb} = 3.3$ km s^{-1}.

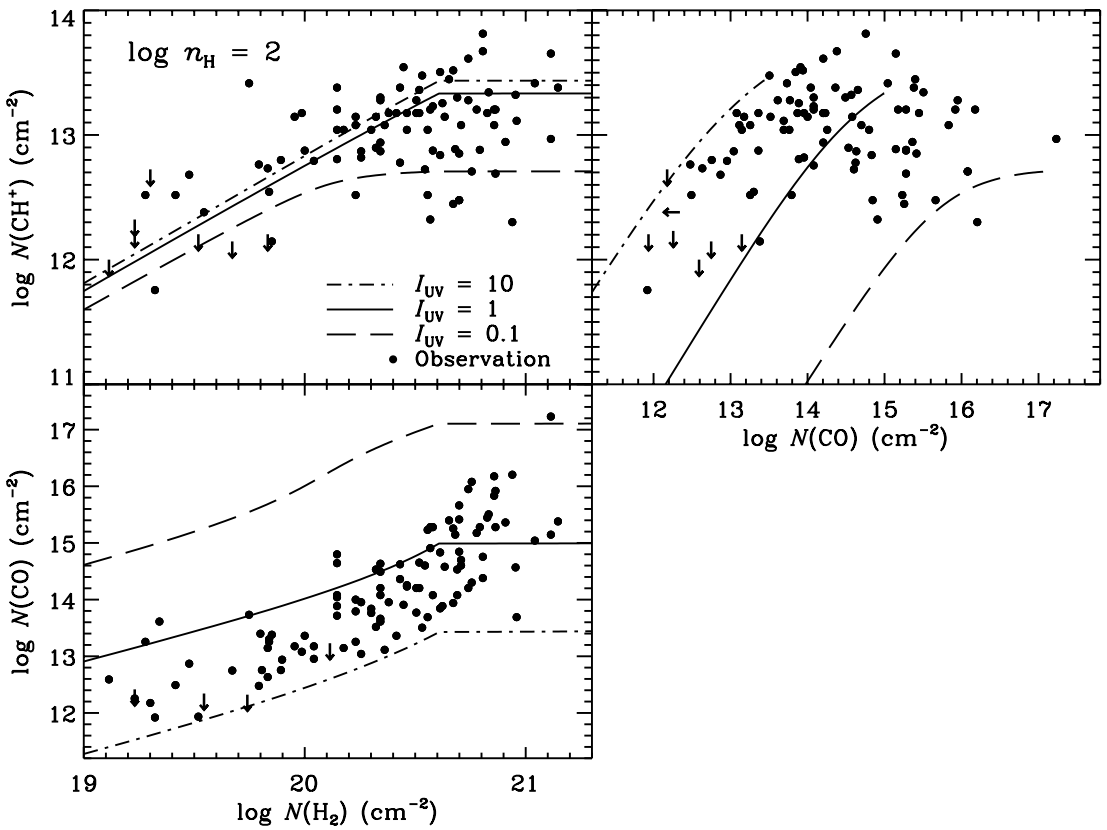

FIG. 22.—CH^+ vs. H_2, CH^+ vs. CO, and CO vs. H_2 as a function of I_{UV}, for $n_H = 100$ cm^{-3} and $\Delta v_{turb} = 3.3$ km s^{-1}.

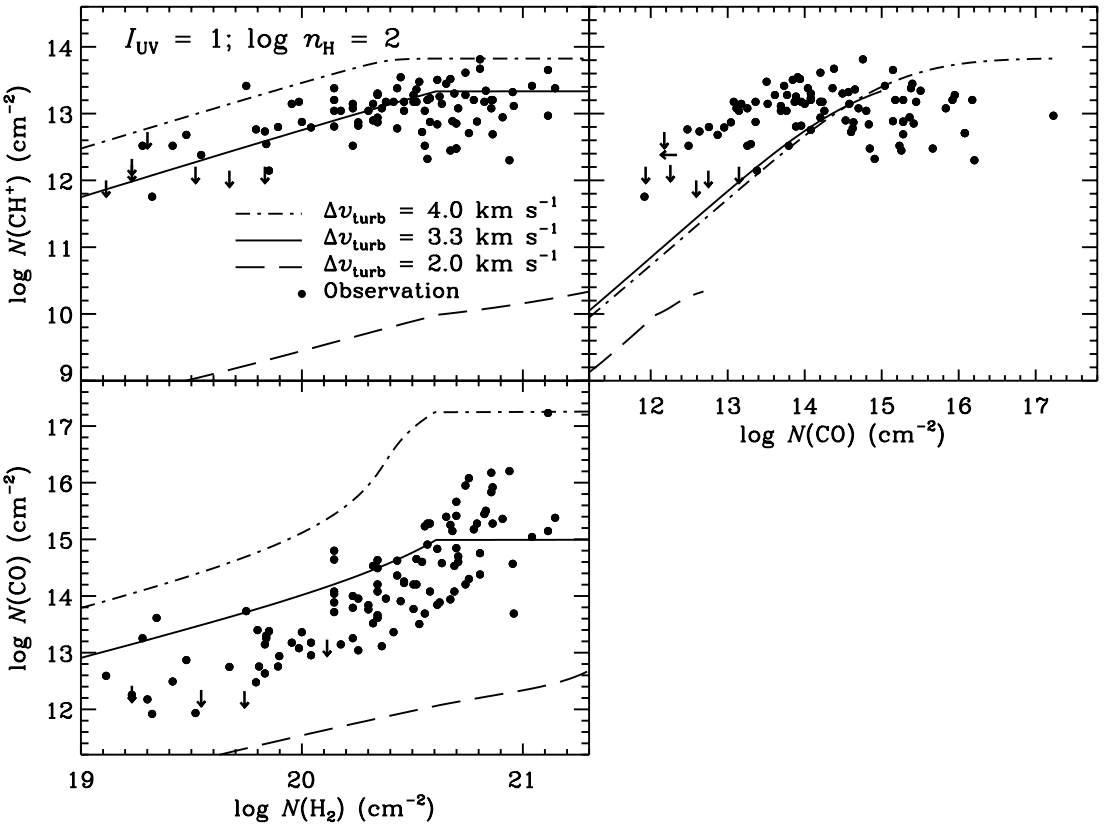

FIG. 23.—CH^+ vs. H_2, CH^+ vs. CO, and CO vs. H_2 as a function of Δv_{turb}, for $I_{UV} = 1$ and $n_H = 100$ cm^{-3}.

related to n_H/I_{UV}. As n_H/I_{UV} increases, the depth at which hydrogen becomes predominately molecular [$f(H_2) > 0.8$] decreases (see Fig. 15 of Le Petit et al. 2006), while an increased H_2 abundance increases the destruction rate of CH^+ through the formation of CH_2^+ and, eventually, CH (§ 6.3). This effect is greatest for $n_H/I_{UV} = 1000$ cm^{-3} (corresponding to log $n_H = 3$, $I_{UV} = 1$ in Fig. 21 or log $n_H = 2$, $I_{UV} = 0.1$ in Fig. 22) because $f(H_2)$ is then nearly 1, whereas for smaller n_H/I_{UV} values $f(H_2)$ never exceeds 0.8 (Le Petit et al. 2006). Our models predict (in Fig. 23) that $N(CH^+)$ increases as Δv_{turb} increases. This trend is easy to understand as a temperature effect. Increasing Δv_{turb} increases T_{eff}, which increases the rate of the reaction given by equation (1).

We find that reasonable assumptions of model parameters can explain the observed distribution in the $N(CH^+)$ versus $N(H_2)$ plot. If we limit ourselves to only the case where $I_{UV} = 1$ (Fig. 21), then over half of the data points lie in the region between the log $n_H = 1$ and 3 lines. About 75% of the rest of the data fall above the log $n_H = 1$ line, i.e., where $n_H < 10$ cm^{-3}. When the effects of turbulence (Fig. 23) are considered, then essentially all the observations are consistent with a suitable combination of n_H and Δv_{turb}.

6.4.2. CH^+ *versus* CO

A plot of log $N(CH^+)$ versus log N(CO) shows an important observational trend that can be understood through our calculations. Initially, $N(CH^+)$ increases with N(CO), as was found in Figure 10. Once N(CO) reaches 10^{14} cm^{-2}, $N(CH^+)$ no longer increases, but levels off at $N(CH^+) \sim 2 \times 10^{13}$ cm^{-2}. For even larger N(CO), $N(CH^+)$ appears to decrease. This trend can be understood as reflecting variations in n_H (or n_H/I_{UV}, if I_{UV} differs significantly from unity). As n_H increases, the amount of CH^+ decreases, while the amount of CO increases (see Fig. 21). Therefore, the observations are well characterized by variations in n_H, since for log N(CO) $\lesssim 14$, where CH^+ and CO are coupled through the $CH^+ + O$ reaction, $n_H = 10$–100 cm^{-3}, while regions of higher CO and lower CH^+ have $n_H > 100$ cm^{-3}. This conclusion does depend somewhat on Δv_{turb}, since for $\Delta v_{turb} = 2$ km s^{-1} the amount of $N(CH^+)$ per N(CO) falls off significantly. However, for regions with values of I_{UV} consistent with the average interstellar far-UV radiation field, the ratio of $N(CH^+)$/N(CO), combined with our models, is a good diagnostic of the density and hence the importance of nonequilibrium effects.

6.4.3. CO *versus* H_2

Our calculations for the variation in N(CO) versus $N(H_2)$ show several important results. Comparing the results of the equilibrium models of Le Petit et al. (2006) with the log $n_H = 2$, $I_{UV} = 1$ calculations, we find that including CH^+ chemistry can increase N(CO) by a factor of 50–100 at low column densities. Such a dramatic increase in CO cannot be attributed to a more rigorous treatment of the CO dissociation rate or geometry effects, both of which would enter at the factor of 2 level (Le Petit et al. 2006). Instead, this points to the chemistry of CH^+ as essential for understanding the abundance of CO in diffuse clouds, especially for $N(CO) < 10^{14}$–10^{15} cm^{-2}. Equilibrium models need high n_H values between 100 and 1000 cm^{-3} to match the observed N(CO) versus $N(H_2)$ (van Dishoeck & Black 1988; Sonnentrucker et al. 2007). Our calculations show that the value of n_H can be an order of magnitude lower. This supports the conclusion of Zsargó & Federman (2003) that nonequilibrium chemistry is important to the formation of CO in diffuse environments. For larger densities (or large n_H/I_{UV}), CH^+ chemistry is less important due to destruction of CH^+ through the formation of CH_2^+ (§ 6.3). For regions where $N(H_2)$ exceeds the cutoff for

nonequilibrium effects, modeled N(CO) values remain constant as a result of the decline in $T_{\rm eff}$ and thus in CO formation rates. However, observed N(CO) can readily reach values higher than 10^{15} cm^{-2} for higher $N(\rm H_2)$. This is because, for large $n_{\rm H}/I_{\rm UV}$, the CO photodissociation rate is less effective in destroying CO while the reaction $\rm C^+(OH,\ H)CO^+$ still forms CO efficiently. The effect of $T_{\rm eff}$ on N(CO) is easily seen in Figure 23, where increasing $\Delta v_{\rm turb}$ by a factor of 2 leads to N(CO) values higher by $\sim$4 dex. Overall, about 35% of the observations require densities ranging from 100 to 1000 cm^{-3}, with the rest requiring lower densities and hence the effect of nonequilibrium $\rm CH^+$ chemistry on CO production.

From Figure 21 we also see that modeled $n_{\rm H}$ values do increase both along and across the (variable) slope of the CO versus $\rm H_2$ distribution. This confirms the results in § 4.3, where these trends were derived qualitatively based on observed CN/$\rm CH^+$ ratios. The range of $n_{\rm H}$ between 10 and 1000 cm^{-3} from Cloudy is in good agreement with the analytic results from the CN chemistry in § 5. For sight lines without detected CN, analytic $\rm CH^+$ chemistry yielded very low values for $n_{\rm H}$, of which some 30% were between 3 and 30 cm^{-3} and thus in agreement with the lowest numerical values in Figure 21. It is evident from the Cloudy results that $\rm CH^+$ resides in regions of lower gas density, whereas higher values of $n_{\rm H}$ correlate well with increased N(CO). This is in excellent agreement with our pointing out in §§ 4 and 5 that higher density gas is associated with both CN and CO, as well as with our empirical finding that $n_{\rm H}$ is revealed by the observed ratio $N(\rm CN)/N(CH^+)$.

7. DISCUSSION

7.1. *The Ratio of* CO *to* $\rm H_2$

In this study we showed (Fig. 6) that the power-law relationship, $N(\rm CO) \propto [N(H_2)]^B$, is observed to behave differently in two density regimes that control the production route for CO. For sight lines below the break at $\log N(\rm H_2,\ CO) = (20.4,\ 14.1)$, the relationship has $B = 1.5 \pm 0.2$, while above the break for higher N, higher $n_{\rm H}$ sight lines, it becomes steeper with $B = 3.1 \pm 0.7$. The higher value for B is consistent with CO photochemical predictions (van Dishoeck & Black 1988) of the transition region between the diffuse and dark cloud regimes (Figs. 6*b* and 7), where UV shielding plays an important role ($\Theta \approx 0.1$) for $N(\rm CO) \approx 10^{15}$ and $N(\rm H_2) \approx 10^{21}$ cm^{-2}. Throughout the plot the vertical dispersion in $\log N$(CO) has a full width of ± 1.0, a range that is much larger than what is expected from observational uncertainties alone. This intrinsic dispersion is influenced by the value of $n_{\rm H}/I_{\rm UV}$, as can be seen in Figures 7, 21, and 22. For $I_{\rm UV}$ that is not far from 1, the width of the dispersion is reflecting the variability of $n_{\rm H}$, since we showed in § 4.3 (and Fig. 17) the changes in CN/$\rm CH^+$ both along and across the relationship of CO versus $\rm H_2$ (for a constant $I_{\rm UV} = 1$). A quantitative numerical confirmation from Cloudy was provided in Figure 21, where for $\log N(\rm H_2) \lesssim 20.5$ the dispersion in CO is seen to correspond to a range in $n_{\rm H}$ between 10 and 100 cm^{-3}.

The CO versus $\rm H_2$ relationship can be recast into

$$\frac{N(\rm CO)}{N(\rm H_2)} \propto [N(\rm H_2)]^{(B-1)},$$

which means that in the regime of diffuse clouds, the abundance of CO relative to $\rm H_2$ is *not* a constant factor but varies between dependence on the square root of $N(\rm H_2)$ ($B - 1 \approx 0.5$) for the lower values of N and dependence on the second power ($B - 1 \approx 2.1$) of $N(\rm H_2)$ for clouds with $\log N \geq 20.4$. This steeper dependence, however, gets shallower again once the transition into the dark cloud regime has occurred, just before CO uses up all the C atoms in the gas. In fact, for the assumed full conversion of C atoms into CO, the constant $\rm CO/H_2$ ratio means that the relative abundance of the two molecules is independent of $N(\rm H_2)$ for the highest N-values. Such global variations have a bearing on $X_{\rm CO}$ whenever measurements include diffuse and translucent sight lines, since low values of $\rm CO/H_2$ for low N-values directly translate into higher values for $X_{\rm CO}$. There is no doubt that this X-factor is dependent on physical conditions that affect the abundance of CO in diffuse molecular clouds. However, since our sample involves essentially local clouds, it is not relevant to the issue of variations in $X_{\rm CO}$ over Galactic scales, where metallicity can play a role (Strong et al. 2004).

Our range of $\log(\rm CO/H_2)$ ratios shows values between -7.58 and -4.68, with the single exception of HD 200775 having a value of -3.88. The latter value is 47% of the value obtained from a full conversion of all carbon atoms into CO molecules, $\log(2 \times \rm C/H) = -3.55$. As remarked earlier, full conversion is expected inside dark clouds, a regime associated with the PDR illuminated by HD 200775. Federman et al. (1980) presented $\log(\rm CO/H_2)$ values between -7.37 and -5.30, i.e., overall lower values that were the result of their sample of sight lines with lower N(CO). For the small samples toward Cep OB2 and Cep OB3 Pan et al. (2005) obtained values from -6.31 to -4.85 and from -6.42 to -5.95, respectively, with the former range clearly including higher N(CO) sight lines. Burgh et al. (2007) and Sonnentrucker et al. (2007) presented restricted samples that ranged from -7.00 to -4.74 and from -6.56 to -4.56, respectively. The results from the smaller samples show good agreement with ours, albeit their ranges are narrower, as expected.

7.2. *Connections to Molecular Clouds*

We showed the correspondence between significant molecular absorption and the presence of molecular clouds seen in emission for a number of directions in the past. Gredel et al. (1992) mapped the high-latitude cloud responsible for the absorption seen toward HD 210121, while Gredel et al. (1994) mapped the CO emission around HD 154368. Federman et al. (1994) indicated the sight lines probing molecular clouds associated with stars in Taurus, Ophiuchus, and Cep OB3, while Wannier et al. (1999) did the same for the dark cloud B5 and stars in Per OB2. Most recently, Pan et al. (2005) examined the correspondence between CO cloudlets seen in emission and stars in Cep OB2.

We can do the same for additional sight lines from the current survey. The most extensive sets of measurements probe molecular clouds in Chamaeleon (HD 93237, HD 94454, HD 96675, HD 99872, and HD 102065), the Southern Coalsack (HD 106943, HD 108002, HD 108639, HD 110434, HD 114886, HD 115071, and HD 115455), and Lupus (HD 137595, HD 140037, HD 144965, and HD 147683). From the emission maps compiled by Andersson et al. (2002) an interesting trend is discerned. Only directions with significant N(CO) values (greater than 10^{15} cm^{-2}) and CN ($\sim 10^{12}$ cm^{-2}, when available) lie within the CO contours. These are HD 96675, which probes the Cham I cloud, and HD 144965 and HD 147683, which pass through a cloud in Lupus. A particularly interesting sight line for future study is toward HD 147683, where N(CO) is about 10^{16} cm^{-2}. Unfortunately, no CN data exist at the present time.

With the aid of the SIMBAD site at the Centre de Données astronomiques de Strasbourg, we found other likely associations based on the similarity in $v_{\rm LSR}$. The direction toward HD 30122 appears to be probing the envelope of L1538 seen in CO emission (Ungerechts & Thaddeus 1987). The gas toward HD 36841

in the Ori OB1 association may be related to that seen in emission from the reflection nebula IC 423 (Maddalena et al. 1986) in the dark cloud L913 (Clemens & Barvainis 1988). For all other sight lines, no clear correspondence could be found.

7.3. *Further Chemical Considerations*

Having applied the analytical expressions to extract gas densities from chemical schemes involving CN and CH^+ to numerous sight lines, we now have a clearer understanding of their limitations. While higher densities are found for CN-rich directions, as also found from our more comprehensive models, the correspondence between density and points on plots of N(CO) versus $N(H_2)$, etc., is rather weak (Fig. 17). The relationships involving N(CN)/N(CH) are stronger (see Fig. 16*a* and the discussion in Pan et al. 2005). The best correspondence is seen when N(CO)/$N(H_2)$ is plotted against N(CN)/$N(CH^+)$ in Figure 16*b*. This arises because CN only probes denser diffuse gas (e.g., Cardelli et al. 1991; Pan et al. 2005), in which CH^+ is more likely to be destroyed by H_2.

The limitations involve a number of factors. For a given velocity component, the amount of CH^+-like CH (Lambert et al. 1990) is not easily obtained; the dispersion in the relationship between N(CH) and $N(CH^+)$ for directions without detectable amounts of CN is too large (Pan et al. 2005). Most sight lines, however, reveal absorption from all three molecules at a given velocity (e.g., Table 3). As for the CH^+ chemistry, the amount of material along a line of sight and the strength of the local interstellar radiation field are not well known, especially for stars greater than a kiloparsec away. More comprehensive models, combining the synthesis of CH^+ and CN, are needed for the next level of understanding. Our goal is to apply models based on Cloudy to this problem.

In this work we presented a series of Cloudy-based calculations of diffuse cloud conditions that simultaneously reproduce the observed H_2, CH^+, and CO abundances in these environments. Diffuse sight lines with $N(\mathrm{CO}) < 10^{14}$–10^{15} cm^{-2} are well characterized by regions with $n_{\mathrm{H}}/I_{\mathrm{UV}} < 100$ cm^{-3}, but only if the effects of CH^+ are taken into account. Without the effects of nonequilibrium CH^+ chemistry, equilibrium calculations predict too little CO per H_2. This result appears robust to uncertainties in the C/H abundance or the CO photodissociation rate. Furthermore, $N(CH^+)$ increases with increasing N(CO), until N(CO) reaches 10^{14}–10^{15} cm^{-2}. For $N(\mathrm{CO}) > 10^{15}$ cm^{-2}, $N(CH^+)$ appears to decrease for increasing N(CO). Our models show that this is likely a density effect, with N(CO) increasing, and $N(CH^+)$ decreasing, with increasing n_{H}. Last, the observed trend of $N(CH^+)$ flattening out at a few times 10^{13} cm^{-2} can be explained if the nonequilibrium chemistry acts only over a certain physical size, such as the Alfvén wave propagation formalism in Federman et al. (1996a). The observed scatter in $N(H_2)$ with $N(CH^+)$ is best explained through a combination of density effects and the importance of nonequilibrium processes, parameterized in this work by Δv_{turb}.

7.4. *The Synoptic View*

The sight lines from our study have properties comparable to those inferred from both (1) H I self-absorption (HISA) clouds with weak or no CO emission and (2) CO-poor H_2 gas revealed via γ-rays and far-infrared (FIR) emission. The former category has been investigated in recent 21 cm radio *absorption* surveys of the Galactic plane (Gibson et al. 2005), showing that cold atomic hydrogen gas is not necessarily associated with detections of CO emission. Since these clouds can be small (<0.6 pc) with $n \geq 100$ cm^{-3} and $T_{\mathrm{spin}} < 50$ K, the physical conditions in them are very similar to the clouds studied here, or in other words, they correspond to the intermediate category of diffuse molecular clouds (Snow & McCall 2006). One may, therefore, assume that despite CO nondetections via radio emission, CO is likely present in these clouds, albeit with low CO/H_2 values determined by small values of $n_{\mathrm{H}}/I_{\mathrm{UV}}$. Such clouds with low N(CO) should, in principle, be detected via UV absorption. For example, Klaassen et al. (2005) provide $N(\mathrm{CO}) < 6 \times 10^{15}$ cm^{-2} for a small HISA feature, an upper limit that excludes only the top 6% of our diffuse sight lines.

In fact, an analysis of a Galactic plane survey by Kavars et al. (2005) has determined that 60% of HISA features are associated with CO emission, with $n \sim$ few $\times$ 100 cm^{-3} and 6 K $< T_{\mathrm{spin}} <$ 41 K. Although Kavars et al. (2005) suggest that these are "missing link" clouds between the atomic and dense molecular varieties, we point out that this region in parameter space is occupied by diffuse molecular clouds. With $H/H_2 \leq 0.01$ and $CO/H_2 \leq 10^{-5}$ (Klaassen et al. 2005), these are probably clouds that include the types of carbon-bearing molecular photochemistries that were explored here. The inferred T_{spin} values are lower than the $T_{01}(H_2)$ kinetic temperatures along diffuse sight lines, resembling more $T_{02}(C_2)$ values that are associated with denser diffuse gas and the presence of ^{13}CO (Sheffer et al. 2007). It will be interesting to see if these colder clouds are related to sight lines with very low $^{12}CO/^{13}CO$ as observed by Liszt & Lucas (1998) using millimeter-wave *absorption* observations.

A second category of CO-poor H_2 gas has been revealed in FIR studies (Reach et al. 1994; Meyerdierks & Heithausen 1996; Douglas & Taylor 2007). The survey of Reach et al. (1994) found infrared excess emission from cirrus clouds attributed to cold H_2 gas and dust, whereas only half of the clouds showed detectable levels of CO emission. When detected, CO was found to be subthermally excited with inferred $n_{\mathrm{H}} \sim 200$ cm^{-3} and $^{12}CO/^{13}CO$ ratios between ~10 and >90, all indicating overlap with the parameter space of diffuse molecular clouds. CO-poor H_2 gas has been inferred also from Galactic surveys of γ-rays (Grenier et al. 2005), which trace the gas content in the ISM and show an "excess" of γ emission not associated with CO emission. Indeed, Grenier et al. (2005) indicate that the CO-less gas is found around dense molecular clouds (that are detected via CO emission) and along bridges between cloud cores and atomic gas, precisely the sites where one would find gas known as diffuse molecular clouds. As is the case with the HISA clouds, we believe that CO is still there, albeit at low levels of abundance relative to H_2 that are potentially observable via UV absorption but are not seen via current methods that detect CO in emission.

Federman & Willson (1982) showed that a connection exists between diffuse molecular gas and dark clouds, namely, that there is good agreement in CH abundance and radial velocity between radio emission for dark clouds and optical absorption along nearby sight lines, the latter probing the outer envelopes of dark clouds. This CH connection has been exploited by Magnani and colleagues (Magnani & Onello 1995; Magnani et al. 2003) in deriving CO/H_2 ratios for translucent sight lines, based on the tight correlation between CH and H_2 (Federman 1982; our § 3.3). Magnani et al. (2005) observed radio emission from CH along the Galactic plane, finding similarities to CO emission line profiles and inferring that the molecular gas has $n_{\mathrm{H}} < 1000$ cm^{-3}. The material resembles the denser gas in our sample of diffuse molecular clouds, consistent with the presence of CO emission (see § 7.2). This connection is also related to OH emission that has been detected from intermediate regions around denser molecular CO-emitting clouds (Wannier et al. 1993) and the lack

of a correlation between $N(^{13}CO)$ and $N(OH)$ in another sample of molecular clouds (Goldsmith & Li 2005).

8. CONCLUSIONS

Our study of diffuse molecular clouds employed a new and extensive sample of sight lines with UV observations of CO and H_2 to explore in detail the power-law relationship between the two species. The slope of $\log N(CO) \propto B \log N(H_2)$ was shown to require two components, one with $B = 1.5 \pm 0.2$ for $\log N(H_2) \leq 20.4$, and another with $B = 3.1 \pm 0.7$ for UV sight lines with higher $N(H_2)$. The break in slope arises from a change in CO production, with $CH^+ + O$ important at low $N(CO)$ and $C^+ + OH$ at $N(CO) > 10^{14}$ cm^{-2}. The ratio CO/H_2 has a dependence on $N(H_2)$ that results in an increase by $\sim$3.5 orders of magnitude over the range of $\log N(H_2) \approx 19.5$–22.0. Causes for variation in X_{CO} include (1) the n_H/I_{UV} ratio, which affects production and destruction, including self-shielding; and (2) the metallicity of gas.

Together with the CO and H_2, we also analyzed new data for the carbon-bearing diatomic molecules CH, CH^+, and CN (as well as C_2) that are accessible through ground-based spectroscopy. The linear relationship between $N(CH)$ and $N(H_2)$ was confirmed again, both directly using these two molecules and indirectly by showing that the CO versus CH relationship follows that for CO versus H_2. After determining fitted relationships of both CO and CH versus H_2, we were able to employ fit parameters in the prediction of $N_p(H_2)$ for three sight lines without H_2 data. Analyzing $N(CH^+)$ versus H_2 and CO resulted in two more confirmations of the power-law break displayed by CO versus either H_2 or CH, showing that this break separates the regime of low-density photochemistry from that involving high density. As for $N(CN)$, all our regression fits returned slopes with $B \leq 1.8$, somewhat shallower than earlier reports. Since essentially all CN detections are along high-density sight lines, the absence of a detected break in slope for the (smaller) CN sample is not surprising.

Many of the sight lines here are helping us to explore molecular environments that are associated with low n_H. As such, these lines of sight probe regions where nonequilibrium CH^+ chemistry is dominating the production of CO, as confirmed by modeling with Cloudy. For those sight lines with higher n_H it was possible to include (equilibrium) chemistry of CH, C_2, and CN to predict molecular abundances and gas density. Such predictions were found to have tighter correlations when $N(C_2)$ is part of the input into the chemical model. For the entire range of densities we showed that the empirical ratio $N(CN)/N(CH^+)$ is better suited than $N(CN)/N(CH)$ as an indicator of the average n_H along diffuse sight lines.

We also considered rotational (excitation) temperatures in our modeling of CO and H_2, showing that $T_{0J}(CO)$ does not vary for $J = 1$–3. On the other hand, $T_{0J}(H_2)$ increases with J, with indistinguishable slopes between $\log T_{0J}$ and $\log T_{01}$ for $J = 2$–4. Further analysis of the excitation of both molecules should help constrain the conditions in diffuse molecular clouds.

As related in § 7.4, it is our understanding that the regime of low-$N(CO)$, low-n_H diffuse molecular clouds is also sampled by a variety of non-UV observational methods, which nonetheless result in a significant number of CO nondetections. Thus, the true nature of diffuse molecular clouds is best revealed by synoptic knowledge extracted from studies spanning the electromagnetic spectrum from radio and FIR, through visible and UV, to γ-ray observations.

We thank NASA for grant NNG04GD31G and STScI for grant HST-AR-09921.01-A. Data files for this paper were accessed through the Multiwavelength Archive at STScI. Y. S. acknowledges the testing and use of Ismod.f by S. Federman, J. Zsargó, D. Knauth, T. Crenny, A. Ritchey, K. Walker, and R. Hupe and thanks the Department of Physics and Astronomy at the University of Toledo for having been granted the title of Research Assistant Professor. M. R. acknowledges support by the National Science Foundation under grant 0353899 for the Research Experience for Undergraduates in the Department of Physics and Astronomy at the University of Toledo. N. P. A. would like to acknowledge financial support through the National Science Foundation under grants 0094050 and 0607497 to the University of Cincinnati. We are grateful to the ESO staff, who made available one night in service mode after the technical problems with the dome wheels had been fixed. Last but not least, we thank an anonymous referee, whose thorough comments helped us to improve our analysis and its presentation.

APPENDIX

As described in § 2, our high-resolution optical data from McDonald Observatory included two atomic transitions belonging to Ca I and Ca II. These were fitted with `Ismod.f`, but we did not provide atomic results in the main body of the paper, which is dedicated exclusively to analysis of molecular results. Thus, for the sake of completeness, in Table 9 we give the fit results for total column densities for the two Ca species along 24 sight lines.

TABLE 9
NEW Ca I AND Ca II DETECTIONS FROM McDONALD DATA

	log N (cm^{-2})			log N (cm^{-2})			log N (cm^{-2})	
STAR	Ca I	Ca II	STAR	Ca I	Ca II	STAR	Ca I	Ca II
BD +48 3437	...	12.97	HD 23478	...	12.08	HD 63005	10.03	12.83
BD +53 2820	...	12.99	HD 24398	9.75	12.01	HD 157857	9.88	12.69
HD 12323	10.53	13.16	HD 30122	...	12.32	HD 190918	...	12.96
HD 13268	10.53	13.11	HD 36841	9.82	11.89	HD 192035	10.63	12.64
HD 13745	10.12	13.07	HD 37367	9.64	12.28	HD 198781	9.77	12.73
HD 14434	10.43	13.01	HD 43818	10.27	12.87	HD 210121	9.97	12.29
HD 15137	10.36	12.90	HD 43819	9.67	12.61	HD 210809	10.31	13.01
HD 23180	...	12.08	HD 58510	10.03	12.77	HD 220057	10.50	12.60

REFERENCES

Abel, N. P., Ferland, G. J., Shaw, G., & van Hoof, P. A. M. 2005, ApJS, 161, 65
Abgrall, H., Roueff, E., Launay, F., Roncin, J. Y., & Subtil, J. L. 1993a, A&AS, 101, 273
———. 1993b, A&AS, 101, 323
Aiello, S., Barsella, B., Chlewicki, G., Greenberg, J. M., Patriarchi, P., & Perinotto, M. 1988, A&AS, 73, 195
Akritas, M. G., & Bershady, M. A. 1996, ApJ, 470, 706
Andersson, B.-G., Wannier, P. G., & Crawford, I. A. 2002, MNRAS, 334, 327
Andre, M. K., et al. 2003, ApJ, 591, 1000
Bally, J., & Langer, W. D. 1982, ApJ, 255, 143
Barbaro, G., Mazzei, P., Morbidelli, L., Patriarchi, P., & Perinotto, M. 2001, A&A, 365, 157
Black, J. H., & van Dishoeck, E. F. 1988, ApJ, 331, 986
———. 1991, ApJ, 369, L9
Boger, G. I., & Sternberg, A. 2005, ApJ, 632, 302
Bohlin, R. C., Savage, B. D., & Drake, J. F. 1978, ApJ, 224, 132
Bowers, C. W. 1997, in *HST* Calibration Workshop, ed. S. Casertano et al. (Baltimore: STScI), 18
Burgh, E. B., France, K., & McCandliss, S. R. 2007, ApJ, 658, 446
Cardelli, J. A., & Clayton, G. C. 1991, AJ, 101, 1021
Cardelli, J. A., Federman, S. R., & Smith, V. V. 1991, ApJ, 381, L17
Cardelli, J. A., Meyer, D. M., Jura, M., & Savage, B. D. 1996, ApJ, 467, 334
Cardelli, J. A., Suntzeff, N. B., Edgar, R. J., & Savage, B. D. 1990, ApJ, 362, 551
Carnochan, D. J. 1986, MNRAS, 219, 903
Cartledge, S. I. B., Lauroesch, J. T., Meyer, D. M., & Sofia, U. J. 2004, ApJ, 613, 1037
Cazaux, S., & Tielens, A. G. G. M. 2002, ApJ, 575, L29
Chan, W. F., Cooper, G., & Brion, C. E. 1993, Chem. Phys., 170, 123
Clemens, D. P., & Barvainis, R. 1988, ApJS, 68, 257
Cowie, L. L., & Songaila, A. 1986, ARA&A, 24, 499
Crane, P., Lambert, D. L., & Sheffer, Y. 1995, ApJS, 99, 107
Crawford, I. A. 1995, MNRAS, 277, 458
Crawford, I. A., Barlow, M. J., Diego, F., & Spyromilio, J. 1994, MNRAS, 266, 903
Crenny, T., & Federman, S. R. 2004, ApJ, 605, 278
Dame, T. M., Hartmann, D., & Thaddeus, P. 2001, ApJ, 547, 792
Danks, A. C., Federman, S. R., & Lambert, D. L. 1984, A&A, 130, 62
Dickman, R. L., Snell, R. L., & Schloerb, F. P. 1986, ApJ, 309, 326
Diplas, A., & Savage, B. D. 1994, ApJS, 93, 211
Douglas, K. A., & Taylor, A. R. 2007, ApJ, 659, 426
Draine, B. T. 1978, ApJS, 36, 595
Draine, B. T., & Katz, N. 1986, ApJ, 310, 392
Dubernet, M. L., Gargaud, M., & McCarroll, R. 1992, A&A, 259, 373
Ducati, J. R., Ribiero, D., & Rembold, S. B. 2003, ApJ, 588, 344
Eidelsberg, M., Jolly, A., Lemaire, J. L., Tchang-Brillet, W.-Ül., Breton, J., & Rostas, F. 1999, A&A, 346, 705
Eidelsberg, M., Lemaire, J. L., Fillion, J. H., Rostas, F., Federman, S. R., & Sheffer, Y. 2004, A&A, 424, 355
Eidelsberg, M., Sheffer, Y., Federman, S. R., Lemaire, J. L., Fillion, J. H., Rostas, F., & Ruiz, J. 2006, ApJ, 647, 1543
Elitzur, M., & Watson, W. D. 1978, ApJ, 222, L141
Enard, D. 1982, Proc. SPIE, 331, 232
Federman, S. R. 1982, ApJ, 257, 125
Federman, S. R., Danks, A. C., & Lambert, D. L. 1984, ApJ, 287, 219
Federman, S. R., Fritts, M., Cheng, S., Menningen, K. M., Knauth, D. C., & Fulk, K. 2001, ApJS, 134, 133
Federman, S. R., Glassgold, A. E., Jenkins, E. B., & Shaya, E. J. 1980, ApJ, 242, 545
Federman, S. R., Huntress, W. T., Jr., & Prasad, S. S. 1990, ApJ, 354, 504
Federman, S. R., Knauth, D. C., Lambert, D. L., & Andersson, B.-G. 1997a, ApJ, 489, 758
Federman, S. R., & Lambert, D. L. 1988, ApJ, 328, 777
Federman, S. R., Lambert, D. L., Sheffer, Y., Cardelli, J. A., Andersson, B.-G., van Dishoeck, E. F., & Zsargó, J. 2003, ApJ, 591, 986
Federman, S. R., Rawlings, J. M. C., Taylor, S. D., & Williams, D. A. 1996a, MNRAS, 279, L41
Federman, S. R., Sheffer, Y., Lambert, D. L., & Smith, V. V. 2005, ApJ, 619, 884
Federman, S. R., Strom, C. J., Lambert, D. L., Cardelli, J. A., Smith, V. V., & Joseph, C. L. 1994, ApJ, 424, 772
Federman, S. R., Weber, J., & Lambert, D. L. 1996b, ApJ, 463, 181
Federman, S. R., Welty, D. E., & Cardelli, J. A. 1997b, ApJ, 481, 795
Federman, S. R., & Willson, R. F. 1982, ApJ, 260, 124
Ferland, G. J., Korista, K. T., Verner, D. A., Ferguson, J. W., Kingdon, J. B., & Verner, E. M. 1998, PASP, 110, 761
Fitzpatrick, E. L., & Massa, D. 1990, ApJS, 72, 163
———. 2005, AJ, 130, 1127
Flower, D. R., Pineau des Forets, G., & Hartquist, T. W. 1985, MNRAS, 216, 775
Frerking, M. A., Langer, W. D., & Wilson, R. W. 1982, ApJ, 262, 590
Garrod, R. T., Rawlings, J. M. C., & Williams, D. A. 2003, Ap&SS, 286, 487
Gibson, S. J., Taylor, A. R., Higgs, L. A., Brunt, C. M., & Dewdney, P. E. 2005, ApJ, 626, 195
Goldsmith, P. F., Heyer, M., Narayanan, G., Snell, R., Li, D., & Brunt, C. 2008, ApJ, 680, 428
Goldsmith, P. F., & Li, D. 2005, ApJ, 622, 938
Gredel, R. 1997, A&A, 320, 929
———. 1999, A&A, 351, 657
———. 2004, A&A, 425, 151
Gredel, R., Pineau des Forêts, G., & Federman, S. R. 2002, A&A, 389, 993
Gredel, R., van Dishoeck, E. F., & Black, J. H. 1993, A&A, 269, 477
———. 1994, A&A, 285, 300
Gredel, R., van Dishoeck. E. F., de Vries, C. P., & Black, J. H. 1992, A&A, 257, 245
Grenier, I. A, Casandjian, J.-M., & Terrier, R. 2005, Science, 307, 1292
Habing, H. J. 1968, Bull. Astron. Inst. Netherlands, 19, 421
Heiles, C., & Troland, T. H. 2005, ApJ, 624, 773
Hollenbach, D. J., Takahashi, T., & Tielens, A. G. G. M. 1991, ApJ, 377, 192
Isobe, T., Feigelson, E. D., & Nelson, P. I. 1986, ApJ, 306, 490
Jenkins, E. B., Jura, M., & Loewenstein, M. 1983, ApJ, 270, 88
Jensen, A. G., & Snow, T. P. 2007, ApJ, 669, 378
Kaczmarczyk, 2000, Acta Astron., 50, 151
Kaufman, M. J., Wolfire, M. G., Hollenbach, D. J., & Luhman, M. L. 1999, ApJ, 527, 795
Kavars, D. W., Dickey, J. M., McClure-Griffiths, N. M., Gaensler, B. M., & Green, A. J. 2005, ApJ, 626, 887
Klaassen, P. D., Plume, R., Gibson, S. J., Taylor, A. R., & Brunt, C. M. 2005, ApJ, 631, 1001
Knauth, D. C., Federman, S. R., Pan, K., Yan, M., & Lambert, D. L. 2001, ApJS, 135, 201
Krelowski, J., & Strobel, A. 1983, A&A, 127, 271
Lambert, D. L., & Danks, A. C. 1986, ApJ, 303, 401
Lambert, D. L., Sheffer, Y., & Crane, P. 1990, ApJ, 359, L19
Lambert, D. L., Sheffer, Y., & Federman, S. R. 1995, ApJ, 438, 740
Larson, R. B. 1981, MNRAS, 194, 809
Larson, K. A., & Whittet, D. C. B. 2005, ApJ, 623, 897
Larson, K. A., Whittet, D. C. B., & Hough, J. H. 1996, ApJ, 472, 755
Larson, K. A., Wolff, M. J., Roberge, W. G., Whittet, D. C. B., & He, L. 2000, ApJ, 532, 1021
Le Coupanec, P., Rouan, D., Moutou, C., & Léger, A. 1999, A&A, 347, 669
Le Petit, F., Nehmé, C., Le Bourlot, J., & Roueff, E. 2006, ApJS, 164, 506
Le Petit, F., Roueff, E., & Herbst, E. 2004, A&A, 417, 993
Lesaffre, P., Gerin, M., & Hennebelle, P. 2007, A&A, 469, 949
Le Teuff, Y. H., Millar, T. J., & Markwick, A. J. 2000, A&AS, 146, 157
Liszt, H. 2003, A&A, 398, 621
Liszt, H. S. 2007, A&A, 476, 291
Liszt, H. S., & Lucas, R. 1998, A&A, 339, 561
Maddalena, R. J., Morris, M., Moscowitz, J., & Thaddeus, P. 1986, ApJ, 303, 375
Magnani, L., Chastain, R. J., Kim, H. C., Hartmann, D., Truong, A. T., & Thaddeus, P. 2003, ApJ, 586, 1111
Magnani, L., Lugo, S., & Dame, T. 2005, AJ, 130, 2725
Magnani, L., & Onello, J. S. 1995, ApJ, 443, 169
Massa, D., Savage, B. D., & Fitzpatrick, E. L. 1983, ApJ, 266, 662
Mattila, K. 1986, A&A, 160, 157
McCall, B. J., et al. 2003, Nature, 422, 500
Meyer, D. M., Jura, M., & Cardelli, J. A. 1998, ApJ, 493, 222
Meyerdierks, H., & Heithausen, A. 1996, A&A, 313, 929
Morton, D. C., & Noreau, L. 1994, ApJS, 95, 301
Neckel, Th., & Klare, G. 1980, A&AS, 42, 251
Pan, K. 2002, Ph.D. thesis, Univ. Toledo
Pan, K., Federman, S. R., Cunha, K., Smith, V. V., & Welty, D. E. 2004, ApJS, 151, 313
Pan, K., Federman, S. R., Sheffer, Y., & Andersson, B.-G. 2005, ApJ, 633, 986
Pan, K., Federman, S. R., & Welty, D. E. 2001, ApJ, 558, L105
Papadopoulos, P. P., Thi, W.-F., & Viti, S. 2002, ApJ, 579, 270
Papaj, J., & Krelowski, J. 1992, Acta Astron., 42, 211
Papaj, J., Wegner, W., & Krelowski, J. 1991, MNRAS, 252, 403
Patriarchi, P., Morbidelli, L., & Perinotto, M. 2003, A&A, 410, 905
Patriarchi, P., Morbidelli, L., Perinotto, M., & Barbaro, G. 2001, A&A, 372, 644
Patriarchi, P., & Perinotto, M. 1999, Mem. Soc. Astron. Italiana, 70, 637

Perryman, M. A. C., et al. 1997, A&A, 323, L49
Polk, K. S., Knapp, G. R., Stark, A. A., & Wilson, R. W. 1988, ApJ, 332, 432
Rachford, B. L., et al. 2002, ApJ, 577, 221
Reach, W. T., Koo, B.-C., & Heiles, C. 1994, ApJ, 429, 672
Ritchey, A. M., Martinez, M., Pan, K., Federman, S. R., & Lambert, D. L. 2006, ApJ, 649, 788
Röllig, M., et al. 2007, A&A, 467, 187
Roth, K. C., & Meyer, D. M. 1995, ApJ, 441, 129
Roth, K. C., Meyer, D. M., & Hawkins, I. 1993, ApJ, 413, L67
Roueff, E., Felenbok, P., Black, J. H., & Gry, C. 2002, A&A, 384, 629
Savage, B. D., Bohlin, R. C., Drake, J. F., & Budich, W. 1977, ApJ, 216, 291
Savage, B. D., Massa, D., Meade, M., & Wesselius, P. R. 1985, ApJS, 59, 397
Savage, B. D., & Sembach, K. R. 1996, ARA&A, 34, 279
Seab, C. G., & Snow, T. P. 1984, ApJ, 277, 200
Shaw, G., Ferland, G. J., Abel, N. P., Stancil, P. C., & van Hoof, P. A. M. 2005, ApJ, 624, 794
Shaw, G., Ferland, G. J., Srianand, R., & Abel, N. P. 2006, ApJ, 639, 941
Sheffer, Y., Federman, S. R., & Andersson, B.-G. 2003, ApJ, 597, L29
Sheffer, Y., Rogers, M., Federman, S. R., Lambert, D. L., & Gredel, R. 2007, ApJ, 667, 1002
Shull, J. M., & Van Steenberg, M. E. 1985, ApJ, 294, 599
Snow, T. P., & McCall, B. J. 2006, ARA&A, 44, 367
Sofia, U. J., et al. 2005, ApJ, 625, 167
Sonnentrucker, P., Friedman, S. D., Welty, D. E., York, D. G., & Snow, T. P. 2002, ApJ, 576, 241
———. 2003, ApJ, 596, 350
Sonnentrucker, P., Welty, D. E., Thorburn, J. A., & York, D. G. 2007, ApJS, 168, 58
Strong, A. W., Moskalenko, I. V., Reimer, O., Digel, S., & Diehl, R. 2004, A&A, 422, L47
Thorburn, J. A., et al. 2003, ApJ, 584, 339
Tull, R. G., MacQueen, P. J., Sneden, C., & Lambert, D. L. 1995, PASP, 107, 251
Ungerechts, H., & Thaddeus, P. 1987, ApJS, 63, 645
Valencic, L. A., Clayton, G. C., & Gordon, K. D. 2004, ApJ, 616, 912
van Dishoeck, E. F., & Black, J. H. 1988, ApJ, 334, 771
———. 1989, ApJ, 340, 273
van Dishoeck, E. F., & de Zeeuw, T. 1984, MNRAS, 206, 383
van Hoof, P. A. M., Weingartner, J. C., Martin, P. G., Volk, K., & Ferland, G. J. 2004, MNRAS, 350, 1330
Wannier, P., Andersson, B.-G., Penprase, B. E., & Federman, S. R. 1999, ApJ, 510, 291
Wannier, P., Penprase, B. E., & Andersson, B.-G. 1997, ApJ, 487, L165
Wannier, P. G., Andersson, B.-G., Federman, S. R., Lewis, B. M., Viala, Y. P., & Shaya, E. 1993, ApJ, 407, 163
Warin, S., Benayoun, J. J., & Viala, Y. P. 1996, A&A, 308, 535
Wegner, W. 2003, Astron. Nachr., 324, 219
Welty, D. E., Federman, S. R., Gredel, R., Thorburn, J. A., & Lambert, D. L. 2006, ApJS, 165, 138
Welty, D. E., & Fowler, J. R. 1992, ApJ, 393, 193
Whittet, D. C. B., Gerakines, P. A., Hough, J. H., & Shenoy, S. S. 2001, ApJ, 547, 872
Williams, J. P., Bergin, E. A., Caselli, P., Myers, P. C., & Plume, R. 1998, ApJ, 503, 689
Witt, A. N., Bohlin, R. C., & Stecher, T. P. 1984, ApJ, 279, 698
Woodall, J., Agúndez, M., Markwick-Kemper, A. J., & Millar, T. J. 2007, A&A, 466, 1197
Young, J. S., & Scoville, N. 1982, ApJ, 258, 467
Young, J. S., & Scoville, N. Z. 1991, ARA&A, 29, 581
Zsargó, J., & Federman, S. R. 2003, ApJ, 589, 319